University of Bergen

Master Thesis

# Characterization of the coastal marine atmospheric boundary layer (MABL) for wind energy applications.

*Author:*
Konstantinos Christakos

*Supervisor:*
Joachim Reuder
*Co-supervisor:*
Birgitte R. Furevik

*A thesis submitted in fulfilment of the requirements*
*for the degree of Master of Science in Meteorology and Oceanography*

*Specialization: Meteorology*

Geophysical Institute
Faculty of Mathematics and Natural Sciences
University of Bergen


June 2013

*"It is the mark of an educated mind to be able to entertain a thought without accepting it. "*

Aristotle ($384BC - 322BC$), Greek philosopher.

**Abstract**

The main problem for the characterization of marine atmospheric boundary layer is the lack of available offshore measurements in relevant altitude range up to 200 m. Remote sensing meteorological instruments such as LIDARs or SODARS are applied in the field to provide the essential wind profile and turbulence data.

The master thesis presents an analysis of 4 years of lidar wind profile measurements at the small island of Storholmen off the Norwegian coast. This site is expected to represent offshore conditions for most of the time. A statistical analysis of different parameters which are related to wind power meteorology, i.e. horizontal and vertical wind speed, turbulence parameters (horizontal and vertical turbulence intensity, and turbulence kinetic energy) and wind shear, is presented. The results show a clear relation between horizontal turbulence intensity distribution and the wind speed. A high correlation between TKE and horizontal turbulence intensity is also observed for high wind speeds. Furthermore, for offshore conditions, the occurrence of high TKE increases.

Offshore wind profiles are investigated with respect to turbulence parameters, atmospheric stability and wind shear. The analysis shows a strong relation between turbulence parameters and average wind profiles and wind shear. The results indicate that these turbulence parameters can potential be used as a proxy of the classification of atmospheric stability for offshore conditions in cases of missing temperature profile data.

Finally, case studies of different mesoscale phenomena are investigated using a combination of SAR, lidar and met mast data. The results show that this potential combination of instruments can be applied for an improved knowledge of these phenomena and their potential effects on offshore applications.

# *Acknowledgements*

It is my great pleasure to thank all the people who contributed and helped me to accomplish this study.

First of all, I would like to express my deep gratitude to my supervisor Professor Joachim Reuder, for his support, patient guidance, encouragement and thoughtful comments. I would also like to express my great appreciation to my co-supervisor Birgitte R. Furevik from the Norwegian Meteorological Institute for her advices and useful critiques.

I am grateful to Dag T. Breistein and Andrea N. Eugster from Vestavind Offshore AS for sharing the wind data. I have to express my sincere thanks to Johnny A. Johannessen from Nansen Environmental and Remote Sensing Center for providing access to the SAR data. I also express my gratitude to NORCOWE and Statoil AS for receiving the Hywind scholarship to participate and present my study at the Deep Sea Offshore Wind *R&D* Conference in Trondheim on January $24-25$, 2013 and at NORCOWE WP meeting in Stavanger on May $21-22$, 2013.

I owe particular thanks to the PhD students Mostafa Bakhoday Paskyabi and Martin Flugge for many inspiring discussions. Thanks to my fellow students at UiB for giving me a wonderful study time in Bergen.

Finally, I would like to express thanks from the bottom of my heart to my family for their support and encouragement during my studies.

# Contents

# Abbreviations

| | |
|---|---|
| **agl** | above ground level |
| **asl** | above sea level |
| **ABL** | Atmospheric Boundary Layer |
| **PBL** | Planetary Boundary Layer |
| **ML** | Mixed Layer |
| **SL** | Surface Layer |
| **LIDAR** | Light Detection and Ranging |
| **SODAR** | Sonic Detection and Ranging |
| **HIRLAM** | High Resolution Local Area Modelling |
| **NORCOWE** | Norwegian Center for Offshore Wind Energy |
| **WRF** | Weather Research and Forecasting |
| **SAR** | Synthetic Aperture Radar |
| **TKE** | Turbulence Kinetic Energy |
| **MKE** | Mean Kinetic Energy |
| **CNR** | Carrier to Noise Ratio |
| **MTP** | Microwave Temperature Profiler |
| **CFD** | Computational Fluid Dynamics |

# Chapter 1

# Introduction

Wind is important variable that affects the human civilization. It has influenced the daily life, the history and inspired religions and mythologies. In ancient Greek mythology, Aeolus, the Keeper of the Winds, released the gentle West Wind, Zephyrus to help Odysseus to sail back home to Ithaca. In the 15th century, Christofer Columbus discovered America using the trade winds from the east (easterlies). For thousand years, the wind energy was used to sail boats, grid grain and pump water.

In recent years, wind turbines use the wind to produce electrical power as an alternative to fossil fuels, reducing CO2 emissions. Due to high wind energy potential over the ocean, offshore wind turbines have been developed the last years. The first offshore wind farm was inaugurated in 1991 off the Danish coast [1]. In 2009, Hywind the first full scale 2.3 megawatt floating wind turbine became operational in the North Sea off of Norway by Statoil AS.

For the development of offshore wind energy applications, the accurate characterization of the marine atmospheric boundary layer becomes crucial. In particular, the better knowledge of wind shear, turbulence, atmospheric stability and wind-wave interaction and their effect on offshore wind profiles and power output of wind turbines are necessary.

Wind shear over the rotor disk and turbulence intensity are important parameters for the design parameter and operation of wind turbines. Both high wind shear and high turbulence intensity have negative impacts on load control and rotor fatigue [2]. On the other hand, high wind shear is connected to higher power output compare to low wind shear [3]. The turbulence intensity also affects the power curves since for high wind speed, the power is higher for lower turbulence intensity [4]. Wind speed and turbulence intensity are closely related to atmospheric stability. Therefore it also effects the wind power generation of wind turbines. For instance, under stable conditions, the average power output at a given nacelle wind speed is greater compare to strongly convective conditions [5].

However, the main problem for the investigation of marine atmospheric boundary layer is the lack of available offshore measurements in relevant altitude range up to 200 m. For this reason, new instrumentation technologies as remote sensing instruments (i.e. LIDAR, SODAR) are used in the field, providing a rich source of wind profile data. LIDAR is now a widely accepted meteorological instrument in the wind energy industry.

The main benefit of a LIDAR system is that its capability to take simultaneous measurements of the 3 wind speed components (u,v,w) in several heights up to 200 m. On the other hand, it cannot provide temperature profile measurements. This information is essential for the estimation of the atmospheric stability using the traditional methods of the MoninObukhov length or the Richardson number.

An alternative method for the estimation of atmospheric stability without available temperature profile measurements was suggested by Wharton and Lundquist [6]. The method defines the thresholds of the turbulence parameters, i.e. horizontal turbulence intensity, vertical turbulence intensity, TKE and the wind shear for the classification the atmospheric stability into 5 main classes. The method should be appropriate for LIDAR or SODAR measurements where the temperature information is missing. The thresholds in the study of Wharton and Lundquist [6] were based on SODAR measurements onshore in Western North America. This study aims to investigate the applicability of the method to lidar measurements for offshore conditions. This was the main motivation for the investigation of offshore wind profiles with respect to turbulence parameters presented here.

This Master Thesis is a part of NORCOWE (Norwegian Center for Offshore Wind Energy). The goal of this study is to contribute to a better knowledge of the marine atmospheric boundary layer for offshore wind energy applications using mainly lidar wind profile data from the small island of Storholmen in the Havsul region. Storholmen is located close to Norwegian coastline, about 8 km northwest of island of Vigra. Due to small island's size and its distance off the coast, the lidar data can be assumed representative for offshore conditions. As a supplementary data to lidar measurements, the meteorological mast data from Ona and SAR data were used in this study.

The study is divided into six chapters. In particular, Chapter 2 gives the basic theoretical knowledge of boundary layer meteorology and wind energy. The description of instrumentation and the data overview is presented in Chapter 3. The results of the statistical analysis and evaluation of lidar data is presented in Chapter 4. The results of the investigation of offshore wind profiles based on turbulence and atmospheric stability is given in Chapter 5. Chapter 6 presents 3 case studies of different mesoscale phenomena using a combination of satellite, lidar and met mast measurements in the Havsul region. Finally, the summary of the results and the outlook is given in Chapter 7.

# Chapter 2

# The Atmospheric Boundary Layer under the Aspect of Wind Energy

## 2.1 Extracting Power from Wind

Power from wind has been used for thousands of years by sailing boats, windmills for grinding grain or pumping water. Nowadays, large onshore and offshore wind parks are connected to the power grids generating large amount of electric power.

### 2.1.1 Wind Energy

Wind energy (E) is a renewable energy resource and is defined as the kinetic energy of air parcels in motion:

$$E = \frac{1}{2}mU^2 = \frac{1}{2}At\varrho U^3 \tag{2.1}$$

where m is the mass of air passing rotor, A is the rotor swept area of the turbine, $\varrho$ is the density of air and U is the wind speed. The wind energy is converted into wind power using wind turbines (Fig. 2.1). The wind power is described by the following mathematical expression:

$$P = \frac{E}{t} = \frac{1}{2}A\varrho U^3 \tag{2.2}$$

FIGURE 2.1: Offshore wind turbine in the North Sea off the coast of Belgium. (Source: http://www.greendiary.com/hywind-world-s-first-floating-turbine-to-start-its-voyage.html)

Eq. 2.2 and 2.1 show that the wind power potential is proportional to the third power of U, i.e. for a doubling in wind speed, the wind power increases eightfold.

In reality every wind turbine has an individual efficiency factor to convert the wind energy into wind power, which the power coefficient ($C_p$). $C_p$ depends on turbine design and represents the rate of available wind power [7]. Considering the power coefficient, Eq. 2.2 becomes:

$$P = \frac{1}{2} A \varrho C_p U^3 \tag{2.3}$$

Based on Betz's law [8], the power coefficient of a wind turbine can not be greater than 16/27 or 59.3%. For this theoretical optimum, the wind speed behind the wind turbine has decreased to 1/3 of the incoming wind speed.

### 2.1.2 Power Curve

The power curve of a turbine describes the expected wind power output as function of wind speed. Fig. 2.2 shows a typical example. For very low wind speeds, it is insufficient for the turbine blades to start rotation. When the wind speed exceeds the cut-in speed, typically 3-4 m/s, the wind turbine will start rotation and wind power generation. For further increasing wind speed, the wind power production increases with the cube of the wind speed until it reaches its maximum at the rated output speed in the order of 12-14 m/s. Above this wind speed, the wind power production remains constant for increasing wind speed by actively controlling the pitch angle of the turbine blades. Due to a risk of damage for a further increase of wind speed which will rise the forces on the wind turbine, the systems shuts down by pitching the blades to minimal resistance to the flow.

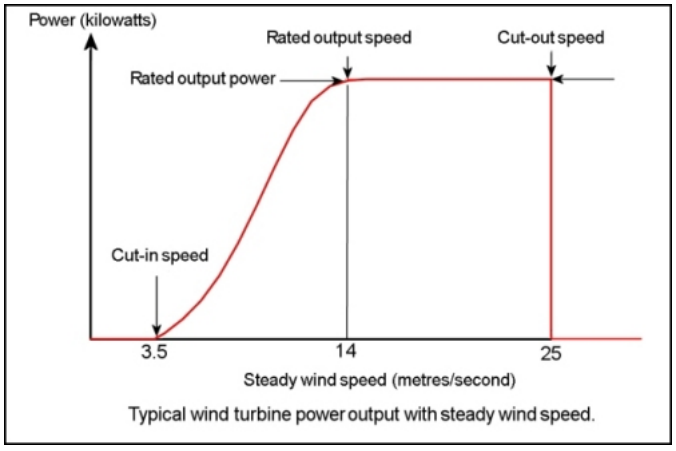


FIGURE 2.2: Typical wind power curve. Adapted from Wind Power Program. (*Source* : *http* : *//www.wind − power − program.com/turbine_characteristics.htm*)

### 2.1.3 Why offshore wind?

The wind potential is usually higher offshore than onshore. Over ocean the wind speeds are higher than over land since the friction is less. In turbulence conditions, offshore areas are more homogeneous compare to onshore locations which have large differences in topography (i.e. mountains, valleys). Fig. 2.4 shows the mean wind speed (m/s) at 10 m agl for the period 1976-95, based on the NCEP/NCAR reanalysis data set. It is clear that the wind speed is higher over ocean than over land. Especially in deep ocean waters the wind potential is much higher compared to coastal areas. Another study (Fig. 2.3) from NASA Jet Propulsion Laboratory shows a large spatial and seasonal variability in wind power potential over oceans. In northern hemisphere, during winter the wind energy is much higher than during northern summer since the frequency of low pressure systems is higher during winter period. In tropics, the wind power potential remains nearly constant during the year and lower compare to mid latitudes.

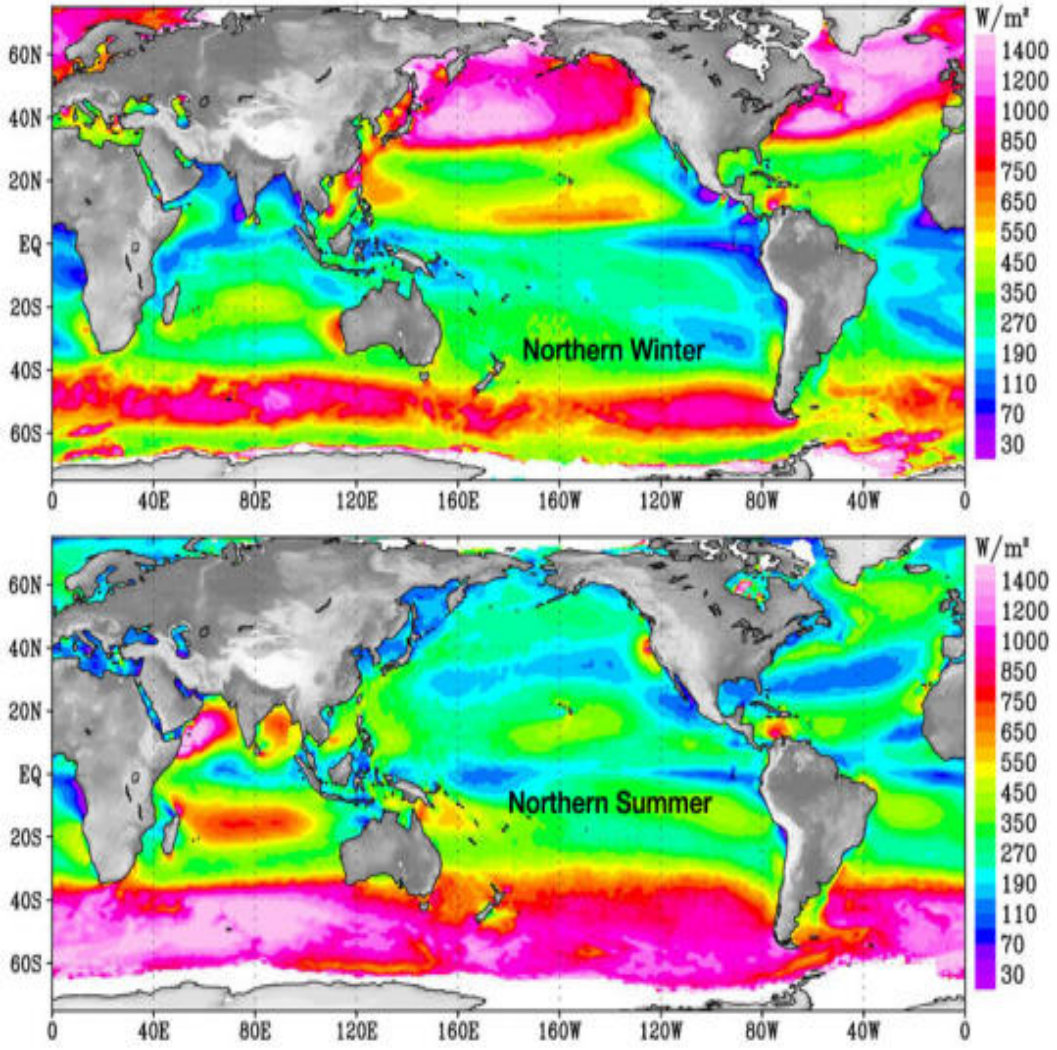


FIGURE 2.3: Map of offshore wind energy potential around the world including 10 years of satellite data. Adapted from NASA Jet Propulsion Laboratory. (*Source* : *http* : *//news.cnet.com/*$8301 - 11128_3 - 9987211 - 54.html$)

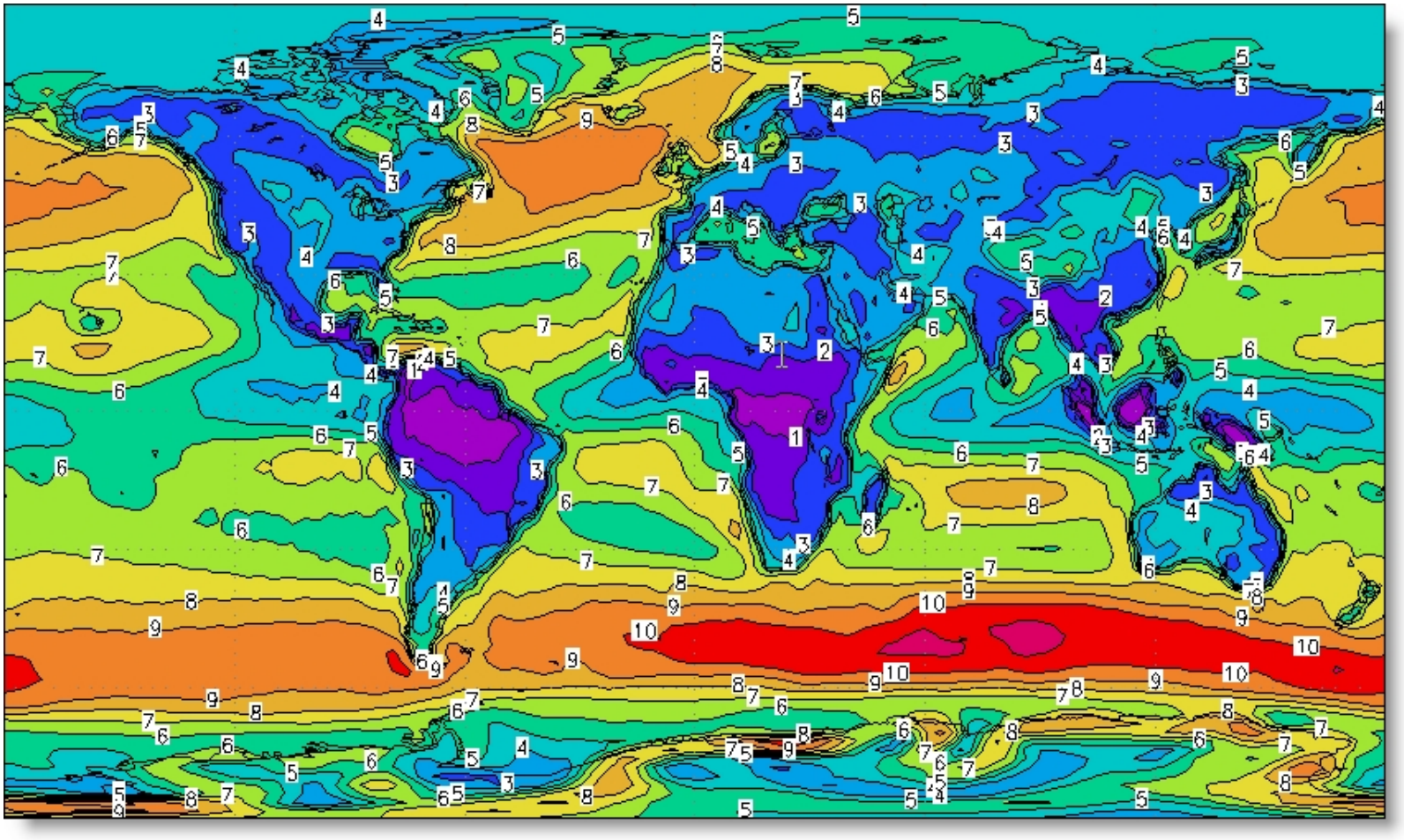

FIGURE 2.4: The mean wind speed (m/s) at 10 m agl for the period 1976-95, based on the NCEP/NCAR reanalysis data set. (*Source* : *http* : *//www.windatlas.dk/world/index.htm*)

## 2.2 Atmospheric Boundary Layer

### 2.2.1 Definition

The atmospheric boundary layer (ABL), also known as the planetary boundary layer (PBL), is defined as the lowest layer of the atmosphere and its behavior is directly influenced by the earth surface. The height of the ABL varies typically between 100 m and 3 km and depends on the surface properties, the time of the day, the seasons and the synoptic weather situations [9]. Above this layer, there is an upper layer which is referred to as Free Atmosphere (FA) [9]. In this layer the wind is approximately geostrophic while the effect of the earth's surface friction on the air motion is negligible. The atmospheric parameters in FA are strongly influenced by the synoptic scale processes and they are not sensitive to the surface properties.

The dynamics and structure of the ABL become critical important for the understanding of different physical processes such as the exchange of heat, water vapor, and momentum with the earth surface, the dispersion of pollutants and the absorption and emission of radiation at the surface and within the atmosphere.

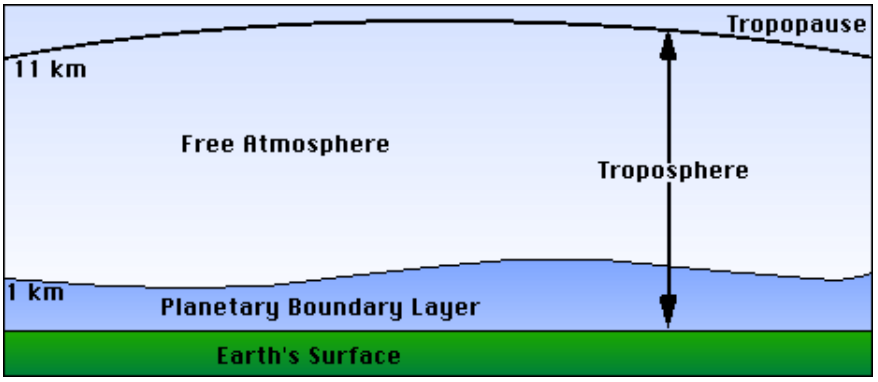


FIGURE 2.5: PBL and FA
(Source: http://san.hufs.ac.kr/ gwlee/session7/whatis.html)

### 2.2.2 Sublayers and Diurnal evolution of the ABL

The ABL can be divided into different sublayers during fair weather conditions over land i.e. the Mixed Layer (ML), the Residual Layer (RL), the Stable (noctural) Boundary Layer (SBL), the Entrainment zone (EZ) and Surface Layer (SL). The figure 2.6 shows the diurnal evolution of the ABL in high pressure regions with low cloud cover. After

sunrise, surface heating causes turbulent eddies to develop. In the ML, meteorological quantities i.e potential temperature and water vapor mixing ratio are quite uniform. At the sunset, the surface cools via radiation cooling and creates the SBL which is a shallow stable layer of air that is in direct contact with the ground. Above this layer there is a residual layer which is the left over part of the mixed layer. In addition there is the entrainment layer (zone) which is a stable layer above the mixed layer. Finally close to the earth surface there is the SL which is the lower part of ABL. In this layer, the turbulent fluxes are approximately constant with height [9].

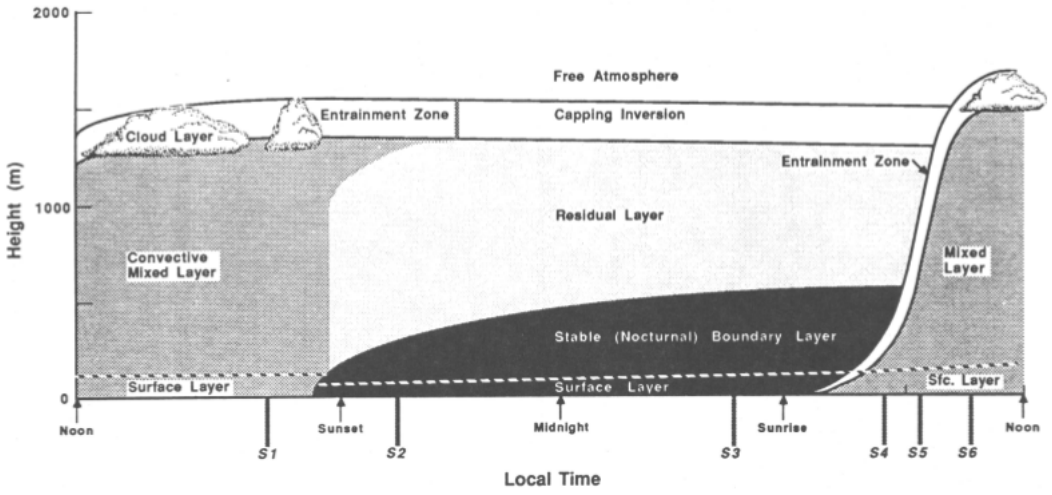


FIGURE 2.6: Diurnal evolution of the ABL over a land. Adapted from [9].

The figure 2.7 shows the typical daytime profiles of mean virtual potential temperature $\bar{\theta_v}$, wind speed $\bar{M}$, water vapor mixing ratio $\bar{r}$ and pollutant concentration $\bar{C}$. Turbulence in the mixed layer is driven by buoyancy and by strong wind shear. The virtual potential temperature is nearly constant with height (adiabatic) in the mixed layer (ML), and is decreasing with height in the surface layer. The ML is usually capped by an inversion which stops the turbulent eddies from rising further. The wind speed increases in the SL, remains constant in th ML, increases again in the EZ and finally becomes geostrophic in the FA. The water vapor mixing ratio and the pollutant concentration have the same vertical daytime profiles. They are nearly constant in the ML, decrease with height in the SL and in the EZ.

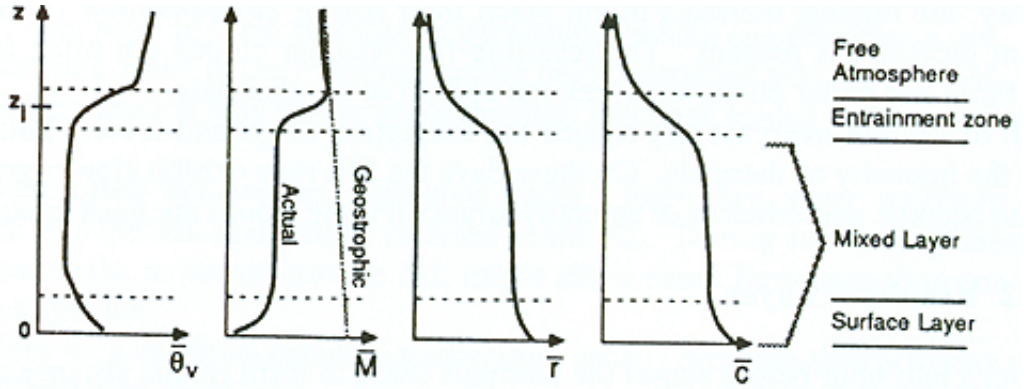


FIGURE 2.7: Vertical daytime profiles at mean virtual potential temperature $\bar{\theta_v}$, wind speed $\bar{M}$ , water vapor mixig ratio $\bar{r}$ and pollutant concentration $\bar{C}$. Adapted from [9].

## 2.3 Boundary Layer Turbulence

Turbulence parameters, such as the horizontal turbulence intensity, the vertical turbulence intensity and the TKE, and the wind shear are important in boundary layer meteorology and in wind energy. Theses parameters describe the turbulence in the wind field, are related to the atmospheric stability and they can effect the wind power generation (see section 2.6).

### 2.3.1 Horizontal Turbulence Intensity

The horizontal turbulence intensity ($I_U$, %) is a dimensionless parameter. It measures the fluctuations of turbulence in the wind field and is defined as the standard deviation of the horizontal wind speed $\sigma_U = \sqrt{\sigma_u^2 + \sigma_v^2}$ over the mean horizontal wind speed $U = \sqrt{u^2 + v^2}$, where u and v are the latitudinal and longitudinal velocity components.

$$I_U = \frac{\sigma_U}{U} \tag{2.4}$$

A variety of meteorological instruments can provide information about the $I_U$ such as cup anemometers, sonic anemometers, SODARs and LIDARs. These instruments can measure the instantaneous wind speed with typical temporal resolution of 1 s or higher. Those measurements are then used to calculate average values in wind power meteorology typically over 10 minutes, and the corresponding standard deviation.

### 2.3.2 Vertical Turbulence Intensity

The vertical turbulence intensity ($I_w$, %) is defined in analogy as the standard deviation of the vertical velocity $\sigma_w$ divided by the mean horizontal wind speed U.

$$I_w = \frac{\sigma_w}{U} \tag{2.5}$$

This parameter was e.g. used by Wharton and Lundquist (2012) [5] to avoid the observed overestimation of $\sigma_U$ by SODARs which would give too high turbulence intensities. Compared to $I_U$, $I_w$ can be measured only by sonic anemometers, SODARs and LIDARs as these instruments can also measure the vertical wind component.

### 2.3.3 Wind Shear Exponent

The wind shear or power law exponent ($\alpha$) is a dimensionless parameter which describes the wind shear. The $\alpha$ exponent is widely used in wind energy. It is calculated by the power law expression [10].

$$U(z) = U_r(\frac{z}{z_r})^\alpha \tag{2.6}$$

$U(z)$: is the wind speed at height, z.
$U_r$: is the wind speed at a reference level, $z_r$.

To calculate the wind shear exponent, the Eq. 2.6 can be rearranged in terms of $\alpha$:

$$\alpha = \frac{\ln(U(z)/U_r)}{\ln(z/z_r)} \tag{2.7}$$

The $\alpha$ is an empirically derived exponent which depends on atmospheric stability [11], [12] and other physical properties, i.e. surface roughness. For neutral conditions, $\alpha$ is approximately 1/7. Hsu et al. (1994) [13] suggested $\alpha = 0.11$ as a good approximation for offshore conditions. Table 2.1 shows the wind shear exponent $\alpha$ for different terrains and roughness lengths. It shows that the wind shear exponent increases, for increasing roughness length.

### 2.3.4 Roughness length

Roughness length $z_0$ is a parameter which related to the characteristics of terrain elements. Under neutral conditions, it is the height at which the wind speed becomes zero in the logarithmic wind profile.

The logarithmic wind profile is described by:

$$u(z) = \frac{u_*}{\kappa}[\ln(\frac{z}{z_0})] \tag{2.8}$$

$u(z)$: is the mean wind speed (m/s) at height z above the ground,
$u_*$: is the friction velocity,
$\kappa$: is the von karman constant (approximately 0.41),
$z_0$: is the surface roughness in meters,

Charnock [14] proposed the following equation to describe $z_0$ over the ocean's surface :

$$z_0 = \alpha_0 \frac{u_*^2}{g} \tag{2.9}$$

$\alpha_0$: is an empirical constant that ranges between 0.01 and 0.035.
g: is the gravitational acceleration.

Assuming that the wind blows steadily and long enough to reach an equilibrium between the wind and wave field, the ocean's surface is aerodynamically rough.

Table 2.1 shows the roughness length as a function of terrain together with the resulting wind shear exponent. It shows that the roughness length increases while the height of the terrain elements increase. Fig. 2.8 shows the effect of $z_0$ on the wind profiles. For a geostrophic balanced wind of 9 m/s on top of the BL, 50 m wind speeds vary between 5 m/s for $z_0 = 0.5m$ and 7 m/s for a smooth water surface.

| **Terrain** | $z_0$ **(m)** | $\alpha$ |
|---|---|---|
| Ice | 0.00001 | 0.07 |
| Snow on flat ground | 0.0001 | 0.09 |
| Calm sea | 0.0001 | 0.09 |
| Coast with onshore wind | 0.001 | 0.11 |
| Snow-covered crop stubble | 0.002 | 0.12 |
| Cut grass | 0.007 | 0.14 |
| Crops, tall grass prairie | 0.05 | 0.19 |
| Hedges | 0.085 | 0.21 |
| Scattered trees and hedges | 0.15 | 0.24 |
| Trees, hedges, a few bulidings | 0.3 | 0.29 |
| Suburds | 0.4 | 0.31 |
| Woodlands | 1 | 0.43 |

TABLE 2.1: Roughness length $z_0$ and wind shear exponent $\alpha$ in different terrains. Adapted from [15].

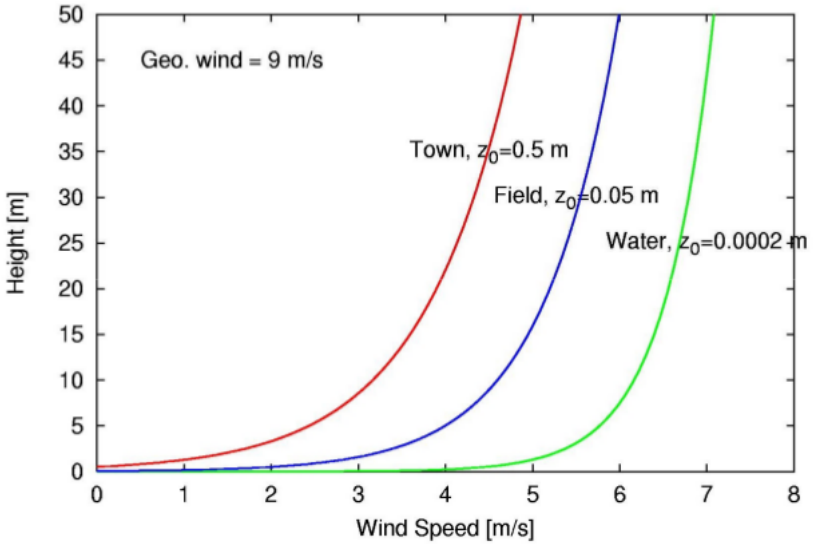


FIGURE 2.8: Wind profiles for different values of $z_0$. (Source: Soren E. Larsen DTU, Riso )

### 2.3.5 Turbulence Kinetic Energy (TKE)

The turbulence kinetic energy (TKE, $m^2/s^2$) is one of the most important parameter in describing the ABL. It is defined as the mean kinetic energy per unit mass and is a direct measure of the three dimensional turbulence. Mathematically, it is described as the sum of variances of the 3 velocity components divided by 2:

$$\frac{TKE}{m} = \frac{1}{2}(\overline{u'^2} + \overline{v'^2} + \overline{w'^2}) \tag{2.10}$$

or

$$\frac{TKE}{m} = \frac{1}{2}(\sigma_u^2 + \sigma_v^2 + \sigma_w^2) \tag{2.11}$$

Combining the Eq. 2.4 and 2.5 with Eq. 2.11, the TKE can be expressed as a function of $I_U$,$I_w$ and U:

$$\frac{TKE}{m} = \frac{U^2}{2}(I_U^2 + I_w^2) \tag{2.12}$$

Fig. 2.9 shows the diurnal cycle of TKE which is measured at 300 m agl in Tennessee in August 1978. The TKE increases from sunrise until afternoon. At 14.00 local time, TKE achieves the maximum value which indicates that the turbulence (i.e. due to heat fluxes) is dominant at the surface layer. From 14.00 until sunset the TKE decreases due to suppression of turbulence.

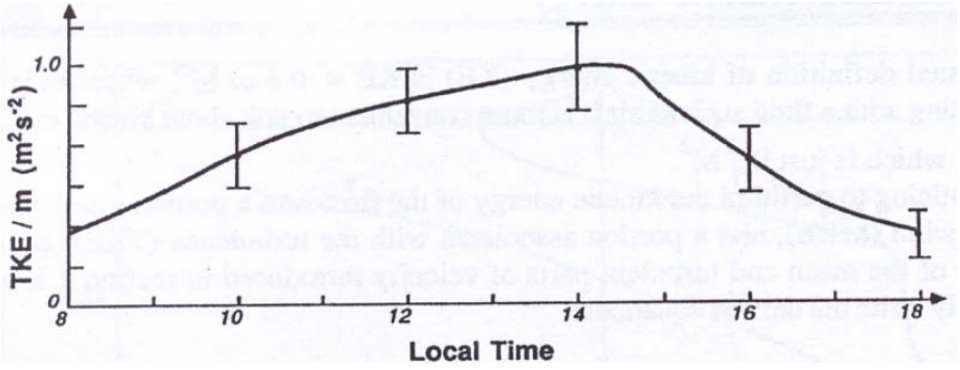


FIGURE 2.9: Diurnal cycle of TKE at 300 m agl in Tennessee, August 1978. Adapted from [16].

Assuming no subsidence, horizontal homogeneity and a coordinate system aligned with the mean wind, the budget of TKE can be described by the following equation:

$$\underbrace{\frac{\partial \bar{e}}{\partial \bar{t}}}_{\text{I}} = \underbrace{\frac{g}{\bar{\theta}_\nu}(\overline{w'\theta'_\nu})}_{\text{II}} \underbrace{-\overline{u'w'}\frac{\partial \bar{U}}{\partial z}}_{\text{III}} \underbrace{-\bar{U}\frac{\partial \bar{e}}{\partial x}}_{\text{IV}} \underbrace{-\frac{\overline{w'e}}{\partial z}}_{\text{V}} \underbrace{-\frac{1}{\bar{\varrho}}\frac{\partial \overline{w'p'}}{\partial z}}_{\text{VI}} \underbrace{-\epsilon}_{\text{VII}} \tag{2.13}$$

where

I: the tendency of TKE ,

II: buoyancy production or consumption term,

III: mechanical (shear) production or consumption term,

IV: advection of TKE by mean flow,

V: transport of TKE by eddies,

VI: pressure correlation term,

VII: viscous dissipation term,

Fig. 2.10 presents the distribution of the terms of the TKE budget equation in a daytime convective BL versus the normalized height $z/z_i$. It shows that the dissipation term is always negative (sink of TKE), the shear generation and buoyancy term are positive (sources of TKE) close to the ground and slightly negative for higher heights.

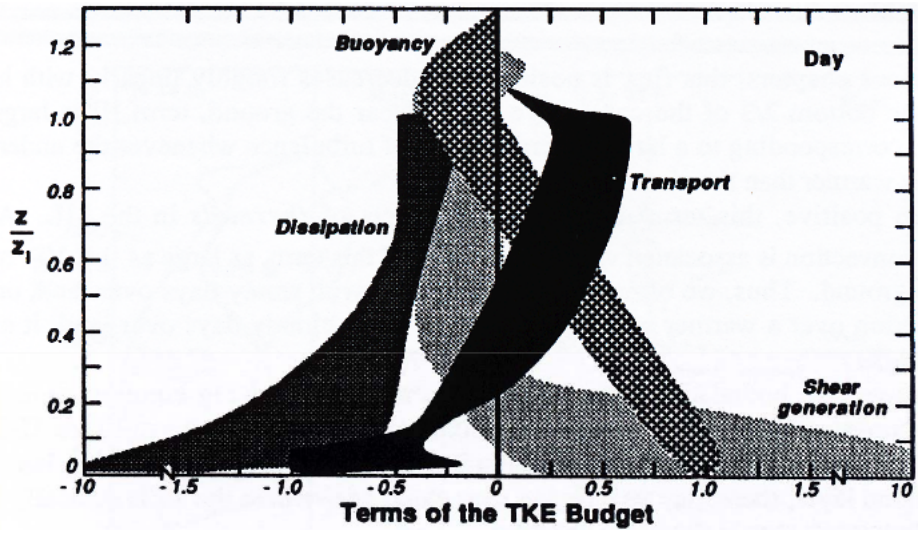


FIGURE 2.10: Effect of roughness length on wind profiles in neutral conditions. Adapted from [9].

### 2.3.6 3D Turbulence Intensity

The 3D turbulence intensity ($I_{3D}$, %) is a dimensionless parameter which describes the relation between the TKE and the mean kinetic energy (MKE) of the flow. It is defined as the square root of the sum of the velocities variances in three directions $\sigma_{3D} = \sqrt{\sigma_u^2 + \sigma_v^2 + \sigma_w^2}$ is divided by the three dimensional wind speed $U_{3D} = \sqrt{u^2 + v^2 + w^2}$.

$$I_{3D} = \frac{\sigma_{3D}}{U_{3D}} = \frac{\sqrt{\sigma_u^2 + \sigma_v^2 + \sigma_w^2}}{\sqrt{u^2 + v^2 + w^2}} \tag{2.14}$$

By the definition of MKE:

$$MKE = \frac{1}{2}(u^2 + v^2 + w^2) \tag{2.15}$$

After some basic calculations and combining the equations 2.11 and 2.15, the 3D turbulence intensity can be written as the square root of TKE divided by MKE:

$$I_{3D} = \sqrt{\frac{TKE}{MKE}} \tag{2.16}$$

## 2.4 Atmospheric Stability

### 2.4.1 Parcel Theory

Atmospheric stability is defined as the resistance of the atmosphere to vertical motion. Based on the parcel theory, there are three basic classes of atmospheric stability:

-**Stable atmosphere**: When an air parcel has displaced upward and it has lower temperature (is denser) than the surrounding environment, the lifted parcel will start to oscillate around its initial position.
-**Unstable atmosphere**: When an air parcel has displaced upward and it has a higher temperature (is less dense) than the surrounding environment, the lifted parcel will start to increase the displacement from its initial position.
-**Neutral atmosphere**: When an air parcel has the same temperature as the surrounding environment, the lifted parcel will remain at the new position.

### 2.4.2 Static Stability

The static stability is based on the vertical density difference of an air parcel. An air column is statically unstable if warm (less dense) air underlies cold (denser) air and statically stable for the opposite situation.

Static stability can be expressed by the Brunt Vaisala frequency or buoyancy frequency (N):

$$N = \sqrt{\frac{g}{\theta}\frac{d\theta}{dz}} \tag{2.17}$$

where $\theta$ is the potential temperature, z is geometric height and g the local acceleration of gravity or

$$N = \sqrt{-\frac{g}{\varrho}\frac{d\varrho}{dz}} \tag{2.18}$$

where $\varrho$ is the density of the air mass.

Another parameter that is connected to surface layer stability is the stability parameter:

$$\zeta = \frac{z}{L} \tag{2.19}$$

where L is the Monin-Obhukov length which has an important role in the Monin-Obhukov Similarity Theory (MOST). It is a measure for the stability by combining the surface fluxes of momentum via $u_*$ and heat.

$$L = \frac{-\overline{\theta_\nu} u_*^3}{kg(\overline{w'\theta_\nu})_s} \tag{2.20}$$

where $\overline{w'\theta_\nu}_s$: surface heat flux,
$u_*^2 = \sqrt{\overline{u'w'}_s^2 + \overline{v'w'}_s^2}$ is the friction velocity,
$\overline{u'w'}_s$: vertical momentum flux of u,
$\overline{v'w'}_s$: vertical momentum flux of v.

L can be interpreted as the height above the surface where the buoyancy production term of TKE dominates for the first time over the mechanical (shear) production term of TKE. The sign of L determines the stability:
-**positive** L indicates a stable surface layer.
-**negative** L indicates a unstable surface layer.

### 2.4.3 Dynamic Stability

In dynamic stability the mechanical (shear) forces become important in contrast to static stability. Kelvin-Helmholtz instability is a phenomenon which is related to dynamic instability. It can occur when a strong wind shear induces instability and overturning in a statically stable stratified atmosphere (Fig. 2.11).

FIGURE 2.11: The Kelvin-Helmholtz instability is visible by clouds. Source: Brooks Martner, NOAA/ETL

The dynamic stability can be described by the Richardson number. The Richardson number is a dimensionless parameter which is named by the British meteorologist, Lewis Fry Richardson. The Richardson number also combines stratification and wind shear:

$$Ri = \frac{N^2}{(\frac{du}{dz})^2} \tag{2.21}$$

In meteorology, the Bulk Richardson number is often used as it is based only on the temperature and wind measurements at two different heights:

$$Ri_B = \frac{g\Delta\overline{\theta_\nu}\Delta z}{\overline{\theta_\nu}(\Delta\overline{U})^2} \tag{2.22}$$

where $\theta_\nu$: is average virtual potential temperature,

$\Delta z$: is the difference of height between two measurements,

$\Delta\overline{\theta_\nu}$: is the measured difference of average virtual potential temperature,

$\Delta\overline{U}$: is the measured difference of average horizontal wind speed.

### 2.4.4 Atmospheric Stability, Turbulence Parameters and Wind Shear.

As presented before a realistic description of stability requires wind and temperature profiles. In particular, remote sensing instruments (i.e. SODAs and LIDARS) cannot provide temperature measurements.

Wharton and Lundquist (2012) [6] presented an alternative method to estimate the atmospheric stability. They expressed the atmospheric stability into five different classes:
- strongly stable,
- stable,
- near-neutral,
- convective,
- strongly convective.

The separation of the stability classes in this work is based on the comparison between a traditional description of atmospheric stability, the Monin-Obukhov length L (Eq. 2.20) and turbulence parameters that can be extracted directly from remote sensed data i.e. horizontal turbulence intensity $I_U$ , vertical turbulence intensity $I_w$ , TKE and the wind shear exponent $\alpha$ at different heights. A description of the boundary layer properties and the corresponding thresholds for each stability class are listed in Table 2.3. The advantage of this method is that the atmospheric stability can be estimated without temperature measurements. In addition, this method is suitable for LIDAR and SODAR measurements where the information of turbulence parameters and wind shear is available. This classification was based on onshore measurements (in Western North America) using SODAR. For offshore applications, this could be a disadvantage of the method since the thresholds have potentially to be adapted to offshore conditions. In our study, we used this method to estimate the atmospheric stability for the offshore area of Havsul using LIDAR data from Storholmen. The results show a high overestimation of strongly stable conditions for the different turbulence parameters. The less overestimated results were obtained using the horizontal turbulence intensity where the strongly stable conditions represents ca. 40% to 70% (see Poster A.1 in Appendix A) during the period 2008-2012.

### 2.4.5 Atmospheric Stability and Standard Deviation of Horizontal Wind Direction ($\sigma$)

Another method to determine the atmospheric stability without using the temperature information is the method of the standard deviation of the horizontal wind direction, $\sigma$. This method is based on the fluctuations on wind direction. The table 2.2 presents the Pasquill stability classes based on $\sigma$.

| **Pasquill Stability Class** | **$\sigma$, degrees** |
|---|---|
| A, very unstable | $\sigma > 22.5$ |
| B, unstable | $17.5 < \sigma \leq 22.5$ |
| C, slightly unstable | $12.5 < \sigma \leq 17.5$ |
| D, neutral | $7.5 < \sigma \leq 12.5$ |
| E, slightly stable | $3.75 < \sigma \leq 7.5$ |
| F, stable | $2.0 < \sigma \leq 3.75$ |
| G, very stable | $\sigma \leq 2.0$ |

TABLE 2.2: Pasquill stability class correlated with standard deviations of horizontal wind direction. Adapted from [17].

For stable conditions the wind direction has a small perturbation which leads to low $\sigma$. For unstable conditions, the perturbation of wind direction becomes greater leading to high $\sigma$.

**Table 1.** Thresholds for wind shear and turbulence during the five major stability classes, as well as associated boundary layer properties.

| Stability class | Boundary layer properties | Hub-height wind speed | Wind shear | Turbulence |
|---|---|---|---|---|
| Strongly stable | Highest shear in swept-area, nocturnal LLJ may be present, little turbulence except just below the LLJ | Strong, especially at night | Highest: $\alpha > 0.3$ | Lowest: $I_U < 8\%$; $I_w < 4\%$; TKE $< 0.4\ \mathrm{m^2\ s^{-2}}$ |
| Stable | High wind shear in swept-area, low amount of turbulence unless a nocturnal LLJ is present | Strong, especially at night | High: $0.2 < \alpha < 0.3$ | Low: $8\% < I_U < 10\%$; $4\% < I_w < 6\%$; $0.4 <$ TKE $< 0.7\ \mathrm{m^2\ s^{-2}}$ |
| Near-neutral | Logarithmic wind profile | Generally strongest | Moderate: $0.1 < \alpha < 0.2$ | Moderate: $10\% < I_U < 13\%$; $6\% < I_w < 9\%$ $0.7 <$ TKE $< 1.0\ \mathrm{m^2\ s^{-2}}$ |
| Convective | Lower wind speeds, low shear in swept-area, high amount of turbulence | Low | Low: $0.0 < \alpha < 0.1$ | High: $13\% < I_U < 20\%$; $9\% < I_w < 17\%$ $1.0 <$ TKE $< 1.4\ \mathrm{m^2\ s^{-2}}$. |
| Strongly convective | Lowest wind speeds, very little wind shear in swept-area, highly turbulent | Lowest | Lowest: $\alpha < 0.0$ | Highest: $I_U > 20\%$; $I_w > 17\%$; TKE $> 1.4\ \mathrm{m^2\ s^{-2}}$. |

TABLE 2.3: Atmospheric stability classes as defined by turbulence parameters and wind shear. Adapted from [5].

### 2.4.6 Modified logarithmic wind profile

The logarithmic wind profile is a relationship which is used to describe the vertical gradient of horizontal wind speed within the atmospheric planetary boundary layer [9]. The mathematical expression of the logarithmic wind profile, taking into account the atmospheric stability, is:

$$u(z) = \frac{u_*}{\kappa}[\ln(\frac{z-d}{z_0}) - \psi(z, L)] \tag{2.23}$$

$u(z)$: is the mean wind speed (m/s) at height z above the ground,

$u_*$: is the friction velocity,

$\kappa$: is the von karman constant (approximately 0.41),

$d$: is the zero displacement or displacement distance,

$z_0$: is the surface roughness in meters,

$\Psi$: is a stability function,

$L$: is the Monin-Obukhov length,

Under neutral conditions, the stability function $\Psi$ becomes equal to zero.

Fig. 2.12 illustrates the dependency of wind profile on atmospheric stability. The wind speed plotted versus the logarithm of the measurement height. For neutral conditions the wind profile is a straight line. On the other hand, for stable and unstable conditions the wind profile is represented by a concave and a convex curve, respectively.

However, Gryning et al. (2007) [18] found that this scheme is only applicable in the lowest part of the PBL (ca. 100 meters) and it is often not valid for stable conditions.

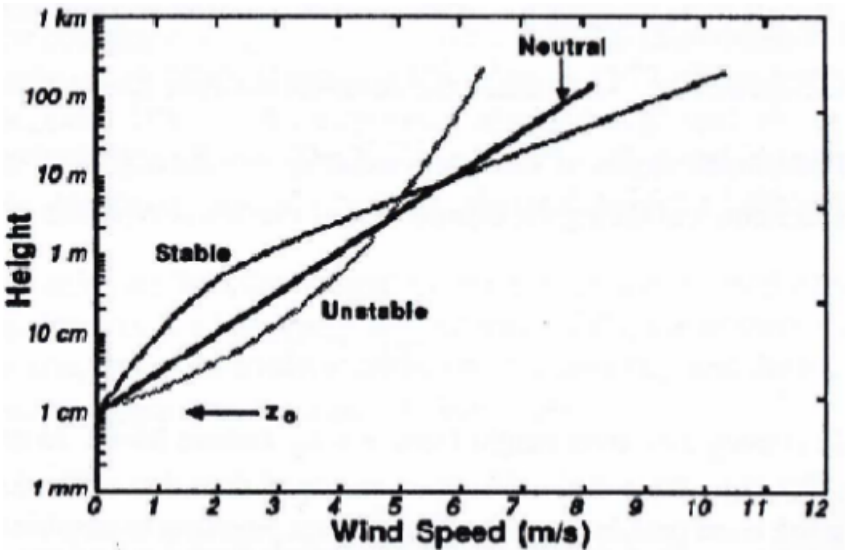


FIGURE 2.12: The effect of atmospheric stability on wind profiles. Adapted from [9].

## 2.5 Marine Atmospheric Boundary Layer (MABL)

The Marine Atmospheric Boundary Layer (MABL), also known as the Marine Boundary Layer (MBL), is defined as that part of the troposphere directly influenced by the presence of the ocean's surface. The MABL plays a important role in controlling the heat, moisture fluxes and the transfer of energy and moisture from ocean's surface to the free atmosphere [19].

In contrast to ABL over land, the diurnal course is absence in MABL, due to high heat capacity of water. In addition, the volume of the distribution of radiation energy is much larger for oceans [20]. In the MABL, the latent heat fluxes are higher in relation to sensible heat due to evaporation over the sea surface.

Furthermore, the MABL is not stationary due to ocean waves that interact with the wind field. Sullivan et al, (2008) [21] investigated the impact of moving and stationary waves on the PBL using Large eddy simulation (LES). Fig. 2.13 and 2.14 illustrate the flow response to different type of waves with a constant geostrophic wind speed of 5 m/s, a wave amplitude of 1.6 m, the phase speed of the waves C of 12.5 m/s. In Fig. 2.13 contours of horizontal wind speed (U) are illustrated for stationary waves (bottom), for C opposite to U (middle), and for C parallel to U (top). In the case of wind vector following waves (top), there is a clear coupling between the horizontal winds and surface waves. The same result is presented in contours of the vertical wind speed in Fig. 2.14

where there is a coupling between the w and surface waves when U and C are parallel [21].

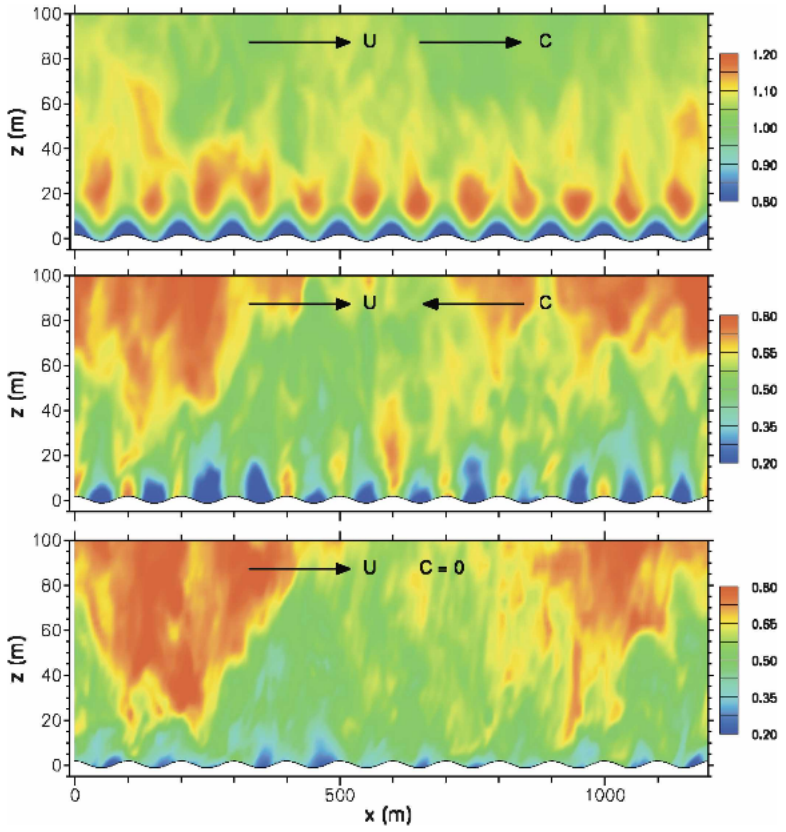


FIGURE 2.13: LES model simulation. Contours of the horizontal wind speed (u) for moving and stationary surface waves. (Bottom) Stationary waves (phase velocity (C) is zero), (Middle) wind vector opposing surface waves, (Top) wind vector following surface waves. Adapted from [21].

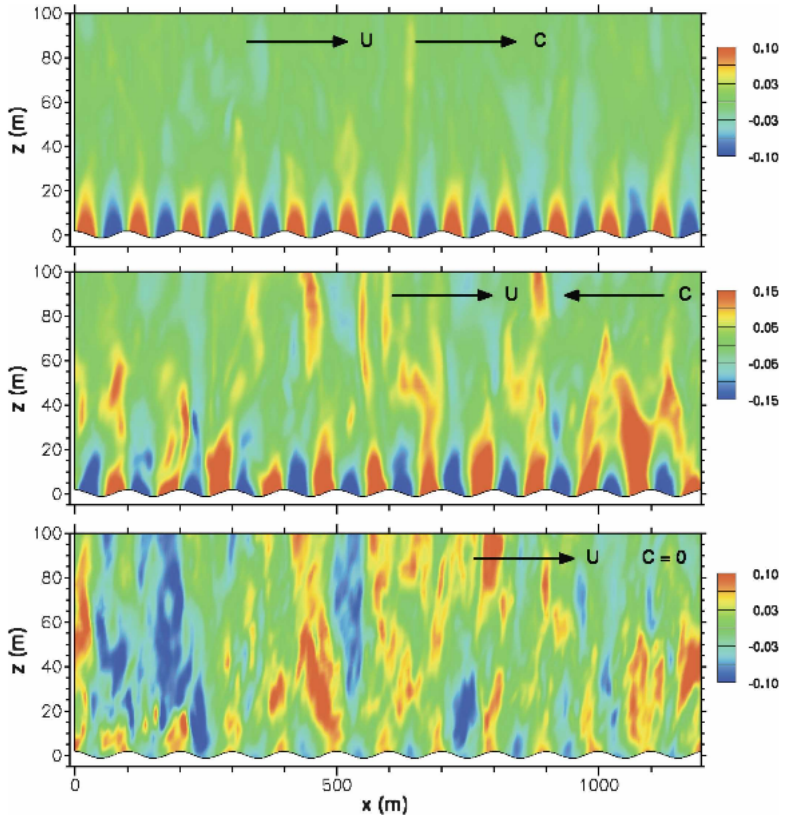


FIGURE 2.14: LES model simulation. Contours of the vertical wind speed (w) for moving and stationary surface waves. (Bottom) Stationary waves (phase velocity (C) is zero), (Middle) wind vector opposing surface waves, (Top) wind vector following surface waves. Adapted from [21].

## 2.6 Power Curves and Atmospheric Parameters

The last section of this chapter will present some studies which have focused on the influence of different atmospheric parameters such as turbulence intensity, TKE and wind shear on the power curves of wind turbines.

### 2.6.1 Power Curve and Horizontal Turbulence Intensity

Kaiser et al. (2003) [4] found that wind power curves are influenced by horizontal turbulence intensity (Fig. 2.15). For low wind speeds, the wind power is higher for high turbulence intensity (16%) compare to turbulence intensities less than 12%. On the other hand, for high wind speed, the wind power is higher for low turbulence intensity (8%) compare to turbulence intensities greater than 12%. Tindal et al. (2008) [22] suggested that for extreme values of turbulence intensity (18%) the wind power decreases at strong wind speed compare to turbulence intensity at 15% (Fig. 2.16)

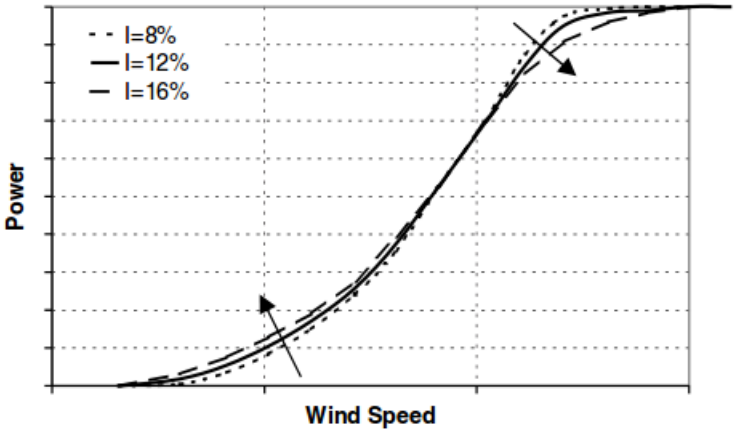


FIGURE 2.15: Power curves as a function of turbulence intensity. Adapted from [4].

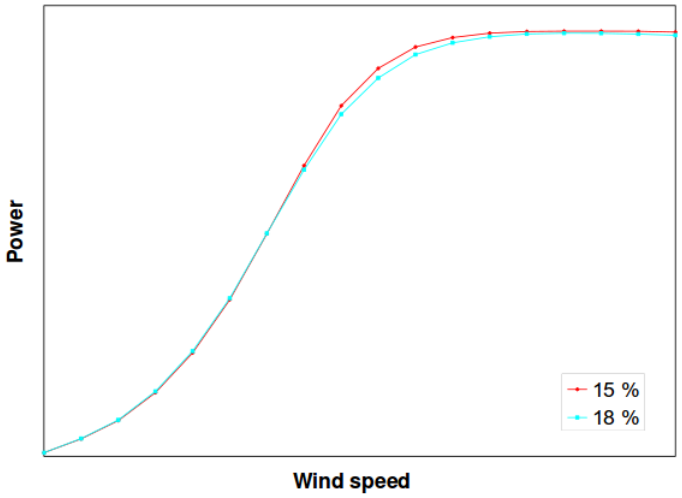


FIGURE 2.16: Power curves for extreme values of turbulence intensity. Adapted from [22].

### 2.6.2 Power Curve and Vertical Turbulence Intensity

Wharton and Lundquist (2012) [5] investigated the effect of vertical turbulence intensity ($I_w$) on wind power generation. They classified the wind power data into stable/strongly stable ($I_w < 6\%$), convective ($9\% < I_w < 17\%$) and strongly convective ($I_w > 17\%$) conditions (Fig. 2.17). The results show that during strongly convective conditions the wind power generation was lower than the expected power for wind between 10.5 m/s and 11 m/s. On the other hand, during stable or strongly stable conditions the power generation is 3% higher than the expected power for wind speeds between 5 and 8 m/s.

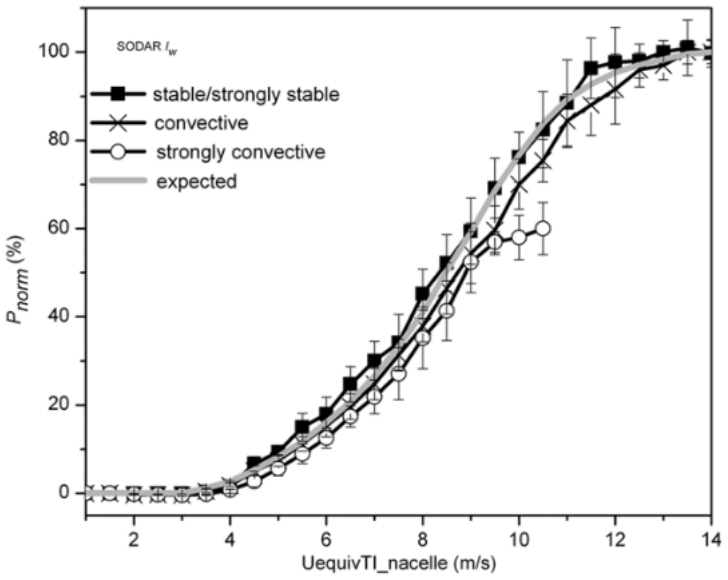


FIGURE 2.17: Power curves for different stability classes based on $I_w$. Adapted from [5].

### 2.6.3 Power Curve and TKE

Wharton and Lundquist (2012) [5] also studied the effect of turbulence kinetic energy ($TKE$) on wind power generation. The wind power data were classified into stable/strongly stable ($TKE < 0.7m^2/s^2$), convective ($1.0m^2/s^2 < TKE < 1.4m^2/s^2$) and strongly convective ($TKE > 1.4m^2/s^2$) conditions. Fig. 2.18 shows that the power generation is higher than the expected power during stable and strongly stable conditions. They found that during strongly convective conditions the average power was ca. 44% in comparison with the expected power of 60%.

### 2.6.4 Power Curve and Wind Shear

Rareshide et al. (2009) [3] suggested that high wind shear is related to higher wind power generation compare to low wind shear (Fig. 2.19). Fig. 2.20 illustrates the power curves for different classes of wind shear. For wind shear greater than 0.2, the wind power is higher (especially for strong winds) compare to cases with wind shear lower than 0.2. Wharton and Lundquist (2012) [5] also observed that wind shear exponent, greater than 0.2, has a positive impact on power performance for wind speeds between 5 m/s and 10 m/s. For wind speeds less than 5 m/s, they found that wind shear has a little effect on power generation. On the other hand, according to Wagner et al. (2009)

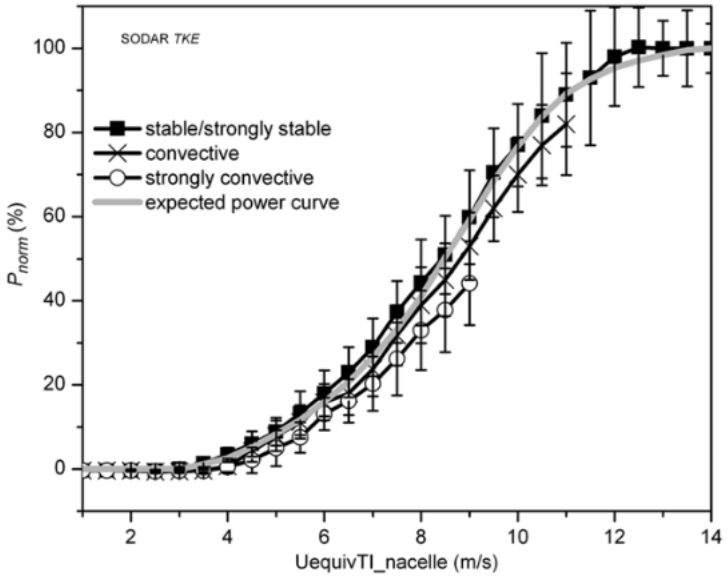


FIGURE 2.18: Power curves for different stability classes based on $TKE$. Adapted from [5].

[23], extreme wind shear decreased wind power by 26% in comparison with no wind shear conditions. This analysis was based on turbines on flat terrain in Denmark. Fig. 2.21(a) shows two power curves (for constant and variable wind speed of the air flow) during no wind shear conditions. For wind speed greater than 8 m/s, the wind power is between 1250 kW to 1850 kW. Fig. 2.21(b) presents the power curves during extreme wind shear conditions. For wind speed greater than 8 m/s, the wind power is between 1000 kW to 1300 kW which is much lower compare to no wind shear conditions.

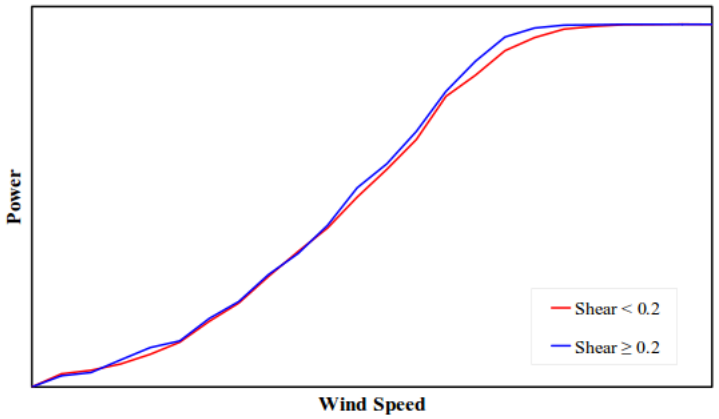


FIGURE 2.19: Power curves for different class of wind shear. Adapted from [3].

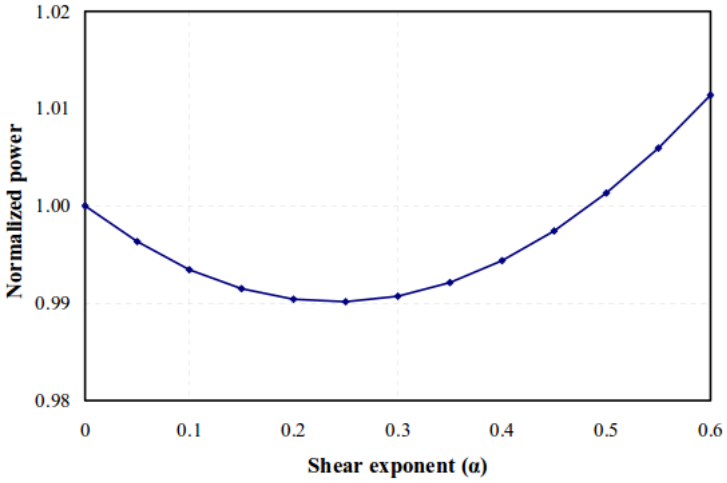


FIGURE 2.20: Normalized power as a function of wind shear exponent ($\alpha$). Adapted from [23].

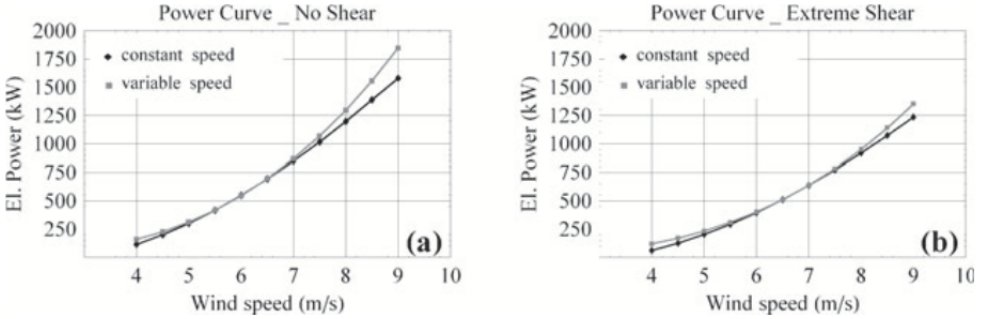


FIGURE 2.21: (a) Power curves during no wind shear conditions, (b) Power curves during extreme wind shear conditions. Adapted from [23].

# Chapter 3

# Instrumentation and Data Overview

The following section describes the measurement platforms and instruments providing the data evaluated in the Master thesis. These are in particular the wind measurements from a 60 m meteorological mast, a LIDAR wind profiler and sea surface winds from satellite data.

## 3.1 LIDAR Wind Profiler

### 3.1.1 What is a LIDAR wind profiler?

A LIDAR (Light Detection And Ranging) wind profiler is an active remote sensing instrument which uses the physical principle of the Doppler shift of a backscattered laser pulse to measure the movement of the air in the line of sight of the instrument. There are different types of LIDAR commercially available which are used for wind energy applications, i.e. ZephIR LIDAR (Fig. 3.1), Galion LIDAR(Fig. 3.2), Windcube LIDAR (Fig. 3.3). In the present study the Windcube lidar v.1 was used to measure the wind profiles.

FIGURE 3.1: ZephIR300, Source: www.zephirlidar.com

FIGURE 3.2: Galion, Source: www.sgurrenergy.com

FIGURE 3.3: WINDCUBE, Source: Vestavind Offshore AS

### 3.1.2 The WINDCUBE LIDAR's principle

The Windcube lidar is a pulsed lidar. Its principle relies on the the measurement of Doppler shift of signal backscattered by atmospheric particles i.e aerosols, sea salt, dust, which are transported by the wind. The Doppler shift describes a change in frequency and wavelength of a signal emitted or reflected by a moving particle. A laser pulse is sent into the atmosphere with a wavelength of 1.54 $\mu$m. Due to the Doppler shift, the

backscattered signal has different frequency than the emitted signal $f_e$. The change in frequency is knows as Doppler frequency $f_d$:

$$f_d = \frac{2f_e}{c} u_r \tag{3.1}$$

where $u_r$ is the radial wind speed i.e. the direction along the laser beam and $c$ is the speed of light [23].

Fig. 3.4 shows schematically the function of Windcube lidar. Measurements in one direction can only provide the line of sight velocity component. To determine the 3D wind speed several measurements have to be combined, assuming horizontal homogeneity of the wind field. The measurement pattern for this is sketched in Fig. 3.5. The lidar send out pulses in a cone angle of 30° and into four different directions, separated by 90° i.e 0°, 90°,180° and 270°, during a period of 1 second for each direction [24]. After the instantaneous 4 seconds the lidar calculates the instantaneous 3D wind vector that is then updated every second based on the last 4 sample measurements.

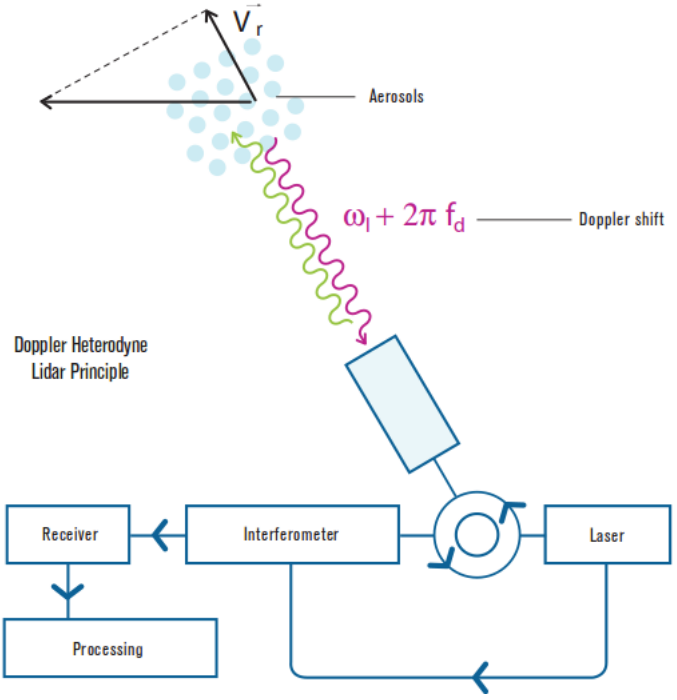


FIGURE 3.4: Measurement process of Windcube lidar. Adapted from [24].

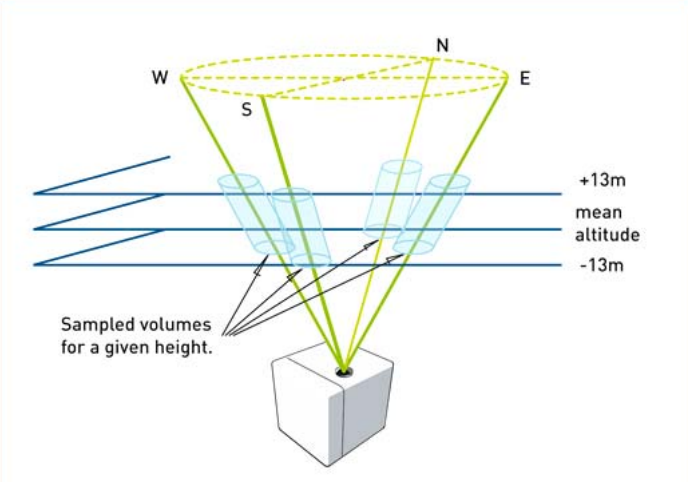


FIGURE 3.5: Sampled volumes and lidar pulses in 4 directions separated by 90°. Adapted from [24].

### 3.1.3 Range gating

The range gating defines the spatial resolution for the wind measurements. The lidar measures the backscatter signal from the aerosols in a defined volume around a specific height (Fig. 3.5). Because the pulse propagates at the speed of light, the sampling distance, z, can be calculated by the following equation:

$$z = \frac{ct}{2} \tag{3.2}$$

where c is the speed of light and t is the time that the signal needs to reach the target and to come back to the sensor [23]. It has to be kept in mind that the lidar measurements always represent a volume average due to the emitted pulse length and the time resolution of the receiver. Fig. 3.6 shows that the backscattered signal is not received from the distance z but from a range which is a function of pulse duration, $T_{pulse}$.

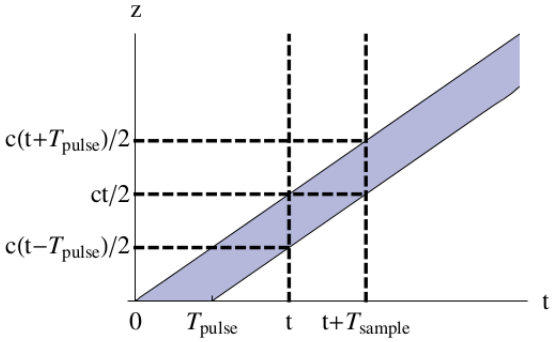


FIGURE 3.6: The length of the range defined by time. Adapted from [23].

### 3.1.4 Three-dimensional (3D) velocity vector

To estimate 3D velocity vector the Windcube lidar rotates the laser beam by 90° to measure four different radial speeds i.e $V_{r0}, V_{r90}, V_{r180}, V_{r270}$ as shown in Fig. 3.7. The following equation (adapted from [23]) calculates the components of the wind velocity (u,v,w):

$$u = \frac{u_{180} - u_0}{2sin(\phi)} \tag{3.3}$$

$$v = \frac{u_{270} - u_{90}}{2sin(\phi)} \tag{3.4}$$

$$w = \frac{u_0 + u_{90} + u_{180} + u_{270}}{4sin(\phi)} \tag{3.5}$$

where $\phi$ is the cone angle.

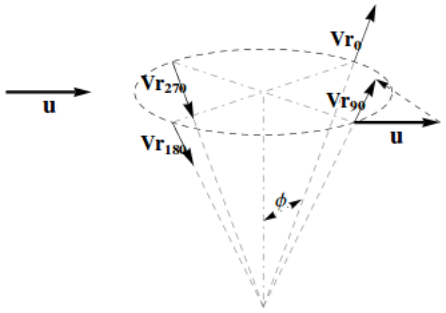


FIGURE 3.7: Cone scan of Lidar. Adapted from [23].

For homogeneous areas, the conical angle is usually selected as 30° while for complex conditions a value of 15° is suggested (Fig. 3.8).

### 3.1.5 Carrier-to-noise ratio (CNR)

The carrier to noise ratio (CNR) is defined as the ratio between the received carrier signal strength relative to the strength of the received noise. The CNR ratio is often specified in decibels (dB) by the following equation:

$$CNR_{dB} = 10log_{10}\frac{C}{N} \tag{3.6}$$

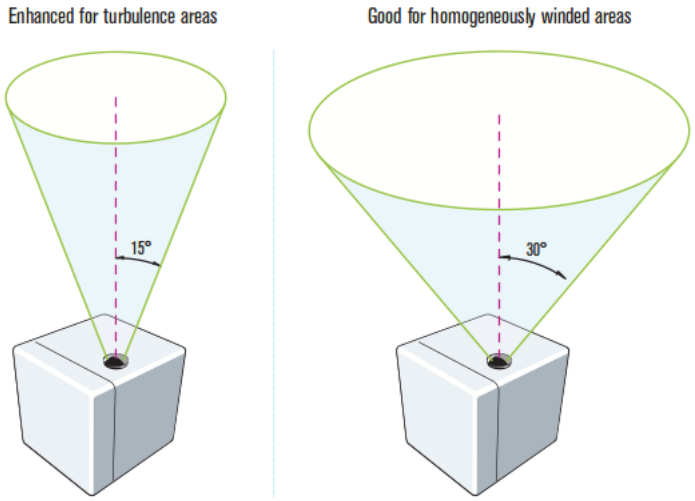


FIGURE 3.8: Lidar conical angle $\phi$. Adapted from [25].

where C is the received modulated carrier signal power and N is the total received noise power.

Fijii and Fukuchi(2005)[26] derived the CNR equation for a coherent lidar:

$$CNR = \eta \frac{T^2 E_x c \beta A_r}{2hvBR^2} \tag{3.7}$$

$h$: Planck's constant,

$\eta$ : overall efficiency factor,

T: atmospheric's extinction,

$v$: the transmitted laser beam frequency,

$c$: speed of light, $\beta$ is the backscatter coefficient by the lidar,

$B$: receiver noise-equivalent bandwidth,

R: target range

$A_r$: aperture area,

$E_x$: laser pulse energy.

A CNR threshold can be defined to select the wind measurements of appropriate quality. In the configuration for Storholmen, Windcube lidar only provides wind data for CNR above $-22dB$.

The data availability is a dimensionless parameter (%) which is defined as [23] :

$$availability = \frac{N_a}{N_{total}} \tag{3.8}$$

$N_a$: the number of wind speeds that actually measured,

$N_{total}$: the total number of wind speeds that theoretically could have been measured

### 3.1.6 Advantages

The main problem for the characterization of the MABL is the lack of observational data in the relevant altitude range. For wind energy applications, remote sensing instruments such as LIDARs offer some advantages over more traditional methods (meteorological masts). Lidars are mobile systems and more flexible with respect to positioning and handling due to their compact size. For remote sites (i.e islands, mountains) without power supply, Lidars can have an autonomous power system. In addition the cost of installation and maintenance is lower compare to high meteorological mast (i.e 150 m and higher). This remote sensing technique has progressed significantly during the last years and is on its way of being widely accepted as essential part of wind resource analysis and related scientific investigations of the MABL.

### 3.1.7 Limitations

#### 3.1.7.1 Aerosol Consentration

The aerosol concentration is stongly related to data availability. The LIDAR uses the aerosol's motion to estimate the wind speed and wind direction. The low aerosol concentration in the air results in a weak backscattered signal which leads to a low carrier to noise ratio (CNR) and consequently wind data of poor and questionable quality. Especially for high heights (i.e. above 200 m height), the aerosol concentration is too low to give good quality of wind measurements. Fig. 3.9 presents the average over the days of August 2010 diurnal variation of CNR at 40 m above the ground level in Boulder, Colorado.

Aitken et. al (2012) [28] describes that the CNR and therefore the availability depends on the atmospheric conditions i.e. the aerosol backscatter. Fig. 3.10 shows a scatter plot of

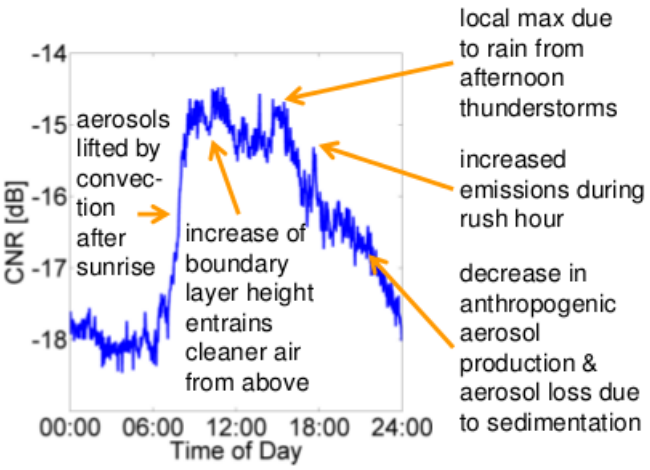


FIGURE 3.9: Average CNR diurnal cycle at 40 m above ground level for the month of August 2010 in Boulder,Colorado. Adapted from [27].

CNR and aerosol backscatter ($\beta$) at 80 m agl in Boulder, Colorado. The high correlation coefficient (0.7) indicates that there is a strong dependency of aerosol backscatter on CNR [28].

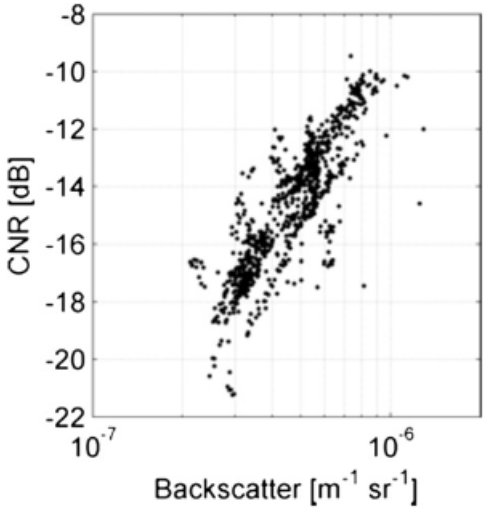


FIGURE 3.10: CNR as a function of aerosol backscatter at 100 m agl, August 2010 in Boulder, Colorado. Adapted from [28].

.

#### 3.1.7.2 Horizontal homogeneity

The Windcube lidar measures the radial speeds at 4 different positions into separated by 90°. The distance of two opposing measurement parts is given by:

$$D = 2tan(\phi)h \tag{3.9}$$

where h is the measurement height and $\phi$ is lidar conical angle. For $\phi$ equals 30° the distance is :

$$D \simeq 1.15h \tag{3.10}$$

When the lidar measures the wind speed at $h = 150m$, the distance between the two parts is $D = 173m$. To retrieve the 3D wind vector, the assumption of horizontal homogeneity at the relevant height (i.e 150 m) must be made. When the wind speed does not vary horizontally i.e over flat terrain, the assumption is correct, and the data are usually of good quality [23]. In complex terrain or very turbulence atmospheric condition, the assumption will often be violated and lead to substantial error in the wind determination (Fig. 3.11) [23],[29].

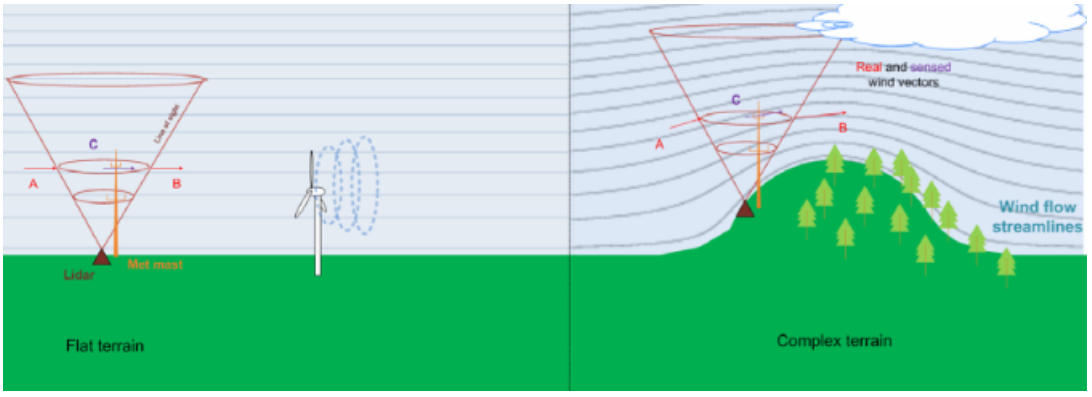


FIGURE 3.11: Lidar measurements in flat and complex terrain. Adapted from [29].

### 3.1.7.3 Precipitation

Precipitation is also a limiting factor for lidar measurements. Especially the vertical wind speed (w) can be affected due to the fall speed of rain drops. On the other hand the horizontal wind speed retrieval is not as strongly affected by precipitation [23],[30],[28]. Fig. 3.12 illustrates w measured by a Windcube lidar together with the rainfall in mm during a field experiment in Iowa, United States [28]. The vertical wind speed has a range of 1-5 m/s (positive values are toward the ground) which is the same order as the terminal velocity of a rain drop [31] and cannot represent the real wind speed [28].

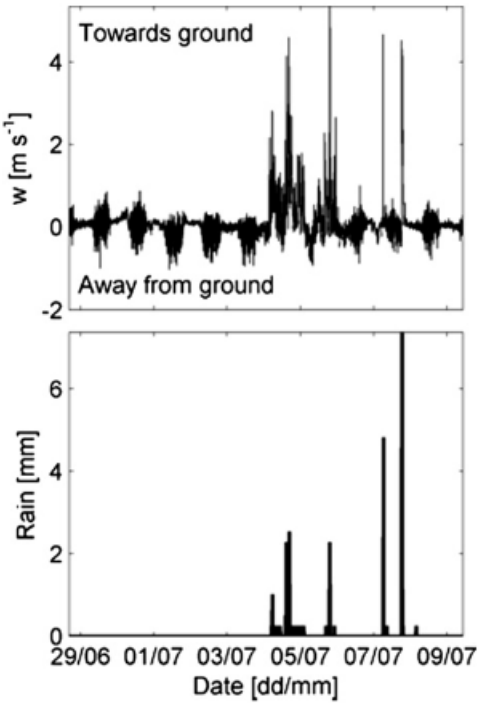


FIGURE 3.12: (Top) Vertical wind speed measured by Windcube lidar at 40 agl and (bottom) precipitation (rain) in Iowa, Unites States. Adapted from [28].

#### 3.1.7.4 Humidity

The CNR of the laser signal depends also on the relative humidity (RH) as aerosol particles increase distinctly in size by swelling at high values of RH. Wulfmeyer et al. (2000) [32] found that aerosol backscattering is constant for low to moderate values of humidity and grows rapidly for RH greater than 0.8. More recently, Aitken et al. (2012) [28] found that the humidity affects CNR only near saturation, since for RH lower than 0.8 there is no correlation between RH and CNR but for $RH > 0.8$ CNR increases (Fig. 3.13) following the non linear regression line (bold black):

$$CNR = a(1 - RH)^b \tag{3.11}$$

where a, b are constants.

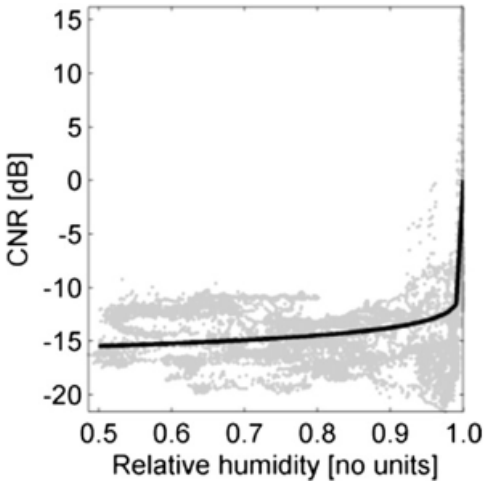


FIGURE 3.13: CNR as a function of RH at 28 June - 9 July 2010, including periods without precipitation in Iowa, United States. The black line indicates the non linear regression line $CNR = -16.3(1 - RH)^{0.0734}$. Adapted from [28].

## 3.2 Basics of SAR data

Radar measurements by synthetic aperture radar (SAR) have widely been used for the estimation of wind from space. SAR is an active microwave instrument for creating images of the earth's surface. It transmits a pulse of microwave radiation (C-Band) and measures the fraction that comes back. The backscattered signal is used for the estimation of the radar cross section $\sigma$ which is a measure of the sea surface roughness. Due to high correlation between $\sigma$ of sea surface and wind speed, it is applied to estimate the wind speed over sea using the C-Band model function (CMOD algorithm) [33]:

$$\sigma^o(U, \phi) = A(\theta)U^{\gamma(\theta)}[1 + B(U, \theta)cos\phi + C(U, \theta)sin\phi] \tag{3.12}$$

where $\phi$: Angle between wind direction and radar look direction,

$U$: surface wind speed,

$\gamma$: wind exponent,

$\theta$: angle of incidence,

$A, B, C$: empirical coefficients.

This satellite data can aid atmospheric scientists to understand better the atmospheric phenomena. Due to its high resolution (10-100 m), it has many applications in meteorology since it can detect a wide range of atmospheric phenomena as hurricanes, polar

lows, gap flows, barrier jets, vortex, internal waves, lee waves and atmospheric fronts. In addition, it is used for offshore wind energy applications while it has advantages for high resolution wind field mapping because it is independent of cloud cover and sunlight. For instance, Johannessen and Korsbakken [34] analyzed SAR measurements to generate high resolution wind energy maps in coastal regions.

One main disadvantage of SAR is that it cannot directly determine the wind direction. The wind direction must be taken from another source such as a numerical model (i.e. HIRLAM), a scatterometer which is collocated in the same time and space, or empirically from the wind structure (i.e. lee waves) in the SAR image [35]. Furthermore, SAR can measure only the wind speed at sea surface. For the accurate estimation of the wind speed at higher levels (i.e. above 10 m) the information on atmospheric stability is necessary.

## 3.3 Data Overview

### 3.3.1 Storholmen Data

Wind profile data were collected by Vestavind Offshore AS from January 2008 to January 2012 at the small island of Storholmen in the Havsul area (Fig 3.14), located about 8 km northwest of the island of Vigra on the West coast of Norway. The measurements were taken with a lidar wind profiler, WindCube v.1 by Leosphere (Fig. 3.3), deployed at 20 m above sea level (asl). Wind speed and wind direction was measured at eight height levels between 60 m and 200 m asl. The basic sampling rate of the instrument was set to 1 Hz, providing independent wind profiles every 4 seconds. However, only the 10 minute average wind profiles and wind speed variances over the period 2008-2012 were available from Vestavind Offshore AS. The data were filtered by Vestavind Offshore AS and measumerements with low CNR were regarding as invalid (NaN). Especially for the higher levels (from 180 to 200 m asl) the data availability was reduced due to the processes discussed in the section of limitations of lidar instrument. For the lidar in Storholmen, the data availability decreases with the height since the average data availability is 76.82% at 60 m asl, 75.87% at 100 m asl and 42.54% at 200 m asl.

The following table 3.1 gives an overview of the performances and specifications of Windcube lidar.

| **Performances** | |
|---|---|
| Range | 40 to 200m |
| Accumulation Time | 0.5 s |
| Data output frequency | 1 Hz |
| Probed length | 20m |
| Scanning cone angle | ~30° |
| Speed Accuracy | 0.2m/s |
| Speed range | Up to 60m/s |
| Direction Accuracy | 2° |
| Data Availability | > 95% up to 150 m* |
| Laser | |
| Wavelength | 1,54 µm |
| Pulse energy | 10 µJ |
| Eye safety | IEC 60825-1 |
| Environmental | |
| Temperature Range | -10 to +40°C with Temperature Con trol Unit* |
| Operating humidity | IP65 |
| Rain protection | Wiper (with water pump), rain detector |
| Compacity | Portable (2persons) |
| Dimensions | |
| Weight | 55 Kg |
| Dimensions | 900X550X550mm with Temperature Control Unit |
| Power Supply Specifications | |
| Electric Power Supply | 24 DC |
| Power consumption | 120 W / 300 W with Temperature Control Unit |
| Data | |
| Format | ASCII/Binary |
| Transfer | GPRS/Ethernet |

* for indication

TABLE 3.1: WINDCUBE Performances and Specifications. Adapted from [24].

### 3.3.2 Ona Data

Measurements from a 60 m meteorological mast (met mast) at Ona (Fig. 3.15) were collected by Vestavind Offshore AS from November 2008 to January 2012. As it shown in Fig. 3.14, Ona island is located to ca. 30km northeast of the Storholmen island, in Sandoy Municipality in More og Romsdal county in Norway. The met mast is deployed 2-3 m asl and it measured the wind speed, wind direction and the corresponding standard deviations in 40 m, 50 m and 60 m agl with cup anemometers and the temperature at 3 m agl. For this study, the Ona measurements were used as an additional information for the wind lidar data from Storholmen island.

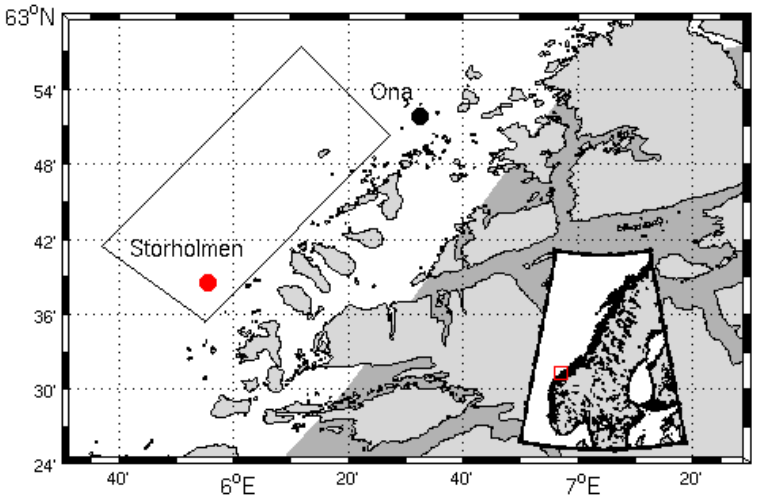


FIGURE 3.14: Location of Storholmen and Ona island in the Havsul region. The box indicates approximate outline of the wind farm concession area.

FIGURE 3.15: Meteorological Mast at Ona island (Source: Vestavind Offshore AS).

### 3.3.3 SAR, met-mast and lidar data

SAR image data were provided by Johnny A. Johannessen via Satellite Radar Data (http://sat.nersc.no) of Nansen Environmental and Remote Sensing Center in Bergen, Norway. The data set contain a worldwide archive of selected Envisat ASAR (Advanced Synthetic Aperture Radar) data and derived information including ocean surface winds, surface roughness and ocean currents information. More specific, the provided data include Envistat ASAR images with information about the $\sigma^o$ parameter in dB which is proportional to surface roughness and their analysis for the calculation of surface wind speed based on CMOD algorithm and wind direction by HIRLAM model.

For this study, selected SAR data from the Havsul area were used with a combination of lidar measumerements in Storholmen and met mast data from Ona. The benefit of lidar and the meteorological mast to measure the wind speed and direction in different height levels were used to provide the information of wind profiles, wind shear and turbulence intensity, lacking from SAR data. This combination of measurement techniques helped us to analyze and investigate complex atmospheric phenomena which took place in Havsul region.

# Chapter 4

# Statistical Analysis of Lidar Data

In the presented analysis, the statistical tools of distributions, probability density, cumulative density, wind roses, and basic statistical values, i.e. mean, median, minimum, maximum and standard deviations, are used to describe and characterize and the mean wind field and turbulence in the area of Storholmen.

## 4.1 Horizontal Wind Speed

The horizontal wind speed is a fundamental parameter as it has an important role in planning onshore/offshore wind farms and in estimating different engineering parameters i.e. power generation, turbine design parameters, extreme, fatigue loads.

Table 4.1 presents different statistical values such as mean, median, minimum (min), maximum (max), standard deviation (std) of horizontal wind speed in 8 different heights for the period 2008-2012 of the wind lidar data in Storholmen. It shows a general increase of mean, median and standard deviation of the wind speed with height. The result indicates that the wind speed increases with height due to the reduction of frictional effects. The mean wind speed takes the lowest values (8.23 m/s and ) at the 60 m asl and achieves the highest value (10.29 m/s) at 200 m asl. For 80 m asl the median takes the lowest value (7.52 m/s) and the highest (9.62 m/s) at 200 m asl. The standard deviation follows the increase of the mean wind speed with height and varies between 5.09 m/s at 60 m asl and 5.94 m/s at 200 m asl. The maximum wind speed (gust) during the 4 year period, 42.51 m/s, was observed at 200 m asl.

| **Height (asl)** | **Mean [m/s]** | **Median [m/s]** | **Max [m/s]** | **Std [m/s]** |
|---|---|---|---|---|
| 60 m | 8.23 | 7.60 | 36.80 | 5.09 |
| 80 m | 8.30 | 7.52 | 38.76 | 5.21 |
| 100 m | 8.95 | 8.27 | 39.90 | 5.38 |
| 115 m | 9.16 | 8.43 | 39.30 | 5.47 |
| 130 m | 9.25 | 8.53 | 40.09 | 5.55 |
| 150 m | 9.53 | 8.79 | 40.85 | 5.70 |
| 175 m | 9.77 | 9.05 | 41.63 | 5.80 |
| 200 m | 10.29 | 9.62 | 42.51 | 5.94 |

TABLE 4.1: Statistics of horizontal wind speed for the period 2008-2012

The monthly variation of horizontal wind speed for different heights is shown in Fig. 4.1. It is clear that the monthly mean wind speeds increase with height. The curve of 200 m asl gets always the highest values of horizontal wind speed during the year in contrast

with the curve of 60 m asl presenting the lowest values. May, June and August are the months with the weakest winds. On the other hand January, October and November are the months with the highest wind speeds since during winter and autumn more frequently low pressure systems and cold fronts travel across the Norwegian coast and bring strong winds in the area.

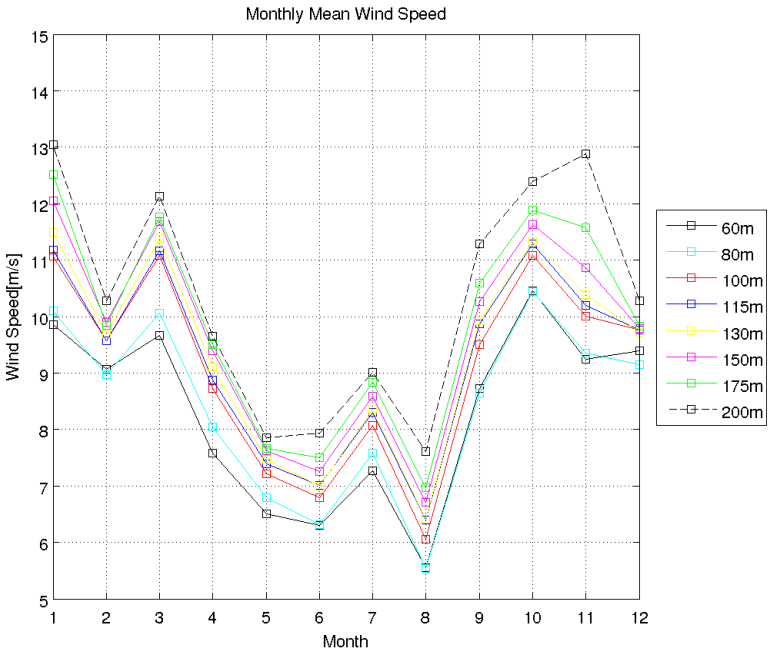


FIGURE 4.1: Monthly variation of mean horizontal wind speed for different heights asl.

### 4.1.1 Wind Direction

For the analysis of wind direction in Storholmen, the graphic tool of wind rose was plotted. This plot is used to describe the distribution of wind direction and wind speed at a particular location.

As illustrated in Fig. 4.2, the prevailing wind blows from the southwest due to a combination of the high frequency of low pressure systems and the effect of Norwegian mountains on the wind flow. For a better understanding of seasonal variation of wind direction, the average wind roses for autumn, winter, spring and summer for the period 2008-2012 are plotted in Fig. 4.3. During autumn (top-left) and winter (top-right) the main wind direction is southwest with a high percentage of strong wind speeds between 10 m/s and 20 m/s. The main wind direction remains southwest in spring but a secondary wind peak direction from northeast occurs with lower wind speeds in the range of 5-15 m/s.

In contrast, the main wind direction during summer is northeast, with a high percentage of wind speed between 5 m/s and 15 m/s. In summer the temperature of the land is higher than the sea, during day. This temperature difference is develops a wind which transfers cooler air from the sea to the land known as sea breeze. According to Gronas and Sandvik (1996) [36] during summer months, see breeze with long duration (due to great length of the summer days) combined with terrain driven circulations occurs frequently along the Norwegian coast having the main wind direction along the coastline, with ocean to the right (northeast). During winter, autumn and spring months, the southwest wind direction dominates mainly due to the synoptic situations.

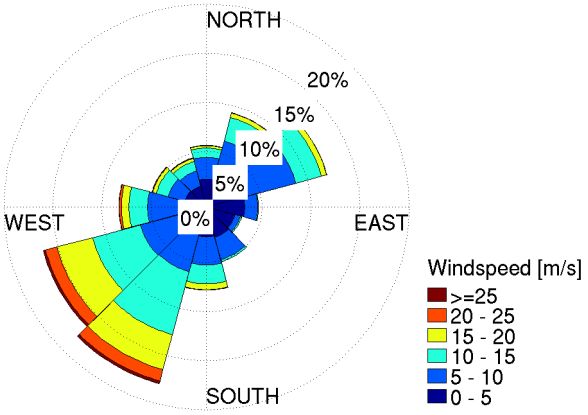


FIGURE 4.2: Overall average wind rose at 100 m asl at Storholmen over the 4 year period 2008-2012.

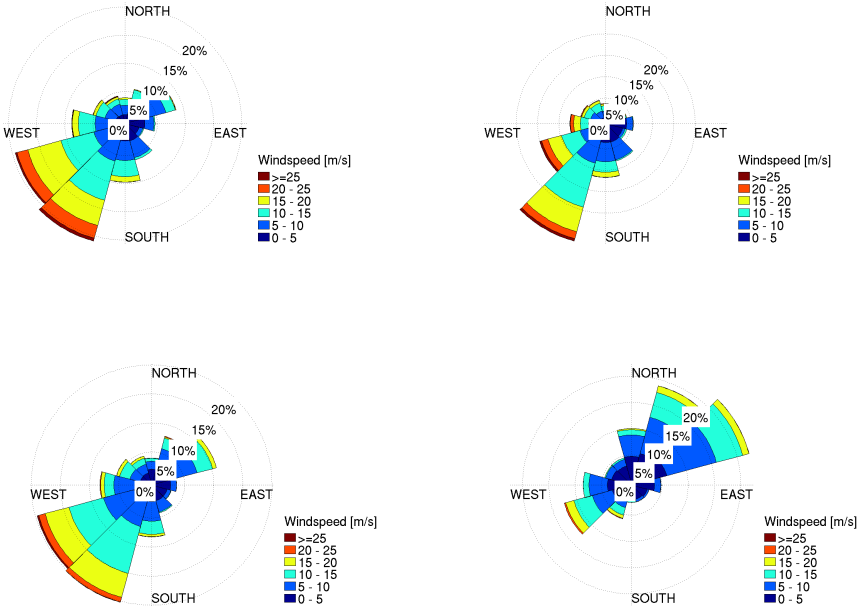


FIGURE 4.3: Average seasonal wind roses for the period 2008-2012. Top-left Autumn (September, October, November), top-right Winter (December, January, February), bottom-left Spring (March, April, May), bottom-right Summer (June, July, August).

### 4.1.2 Wind Distributions

The probability distribution of wind speed is an essential statistical parameter in wind power meteorology. It plays a critical role for the estimation of wind energy production since the average wind power of a wind turbine $\overline{P}$ can be calculated using the probability density function of horizontal wind speed f(U) by the following equation :

$$\overline{P} = \int_0^\infty P(U) f(U) dU \tag{4.1}$$

where P(U) is the turbine power output at a wind speed U [7].

Due to lack of sufficient wind data for the estimation of design parameters, the probability distribution of wind speed can also be used as the substitute for wind data. In the field of the wind power, the Weibull distribution is typically used to statistically describe and approximate wind observations [37].

In addition to the Weibull distribution, a number of other distributions has been tested in this analysis of the horizontal wind speed at Storholmen. This list contains the

following distributions: Continuous, Beta, Birnbaum-Saunders, Exponential, Extreme value, Gamma, Generalized extreme value, Generalized Pareto, Inverse Gaussian, Logistic, Log-logistic, Lognormal, Nakagami, Normal, Rayleigh, Rician, t location-scale and Weibull. The method of maximum likelihood estimates (MLEs) was applied using MATLAB programming language to calculate the parameters for each distribution and find the best.

Table 4.2 presents the resulting best distributions for the horizontal wind speed for each measurement level. The Weibull and the Nakagami distributions perform clearly best for offshore wind conditions. The Nakagami distribution has many applications in technical and life sciences (i.e. medicine, biology) and it is related to Gamma distribution [38]. The Weibull distribution is broadly used for wind energy applications. Most of the heights i.e 80 m, 115 m, 130 m, 150 m and 175 m asl, the Weibull distribution represents better the wind speed distribution. On the other hand only for 60 m, 100 m and 200 m asl, the Nakagami gives better results than the Weibull.

| **Height (asl)** | **Best Distribution** |
|---|---|
| 60 m | Nakagami |
| 80 m | Weibull |
| 100 m | Nakagami |
| 115 m | Weibull |
| 130 m | Weibull |
| 150 m | Weibull |
| 175 m | Weibull |
| 200 m | Nakagami |

TABLE 4.2: The best distribution of horizontal wind speed for different height, period 2008-2012.

Fig. 4.4 shows the histogram of horizontal wind speed and the best 4 fitting distributions (Nakagami, Weibull, Gamma and Rayleigh) at 100 m asl for the period 2008-2012. It is clear that the Nakagami and Weibull distributions can fit better on the histogram of horizontal wind speed.

The cumulative distribution of wind speed is shown in the Fig. 4.5(top). The empirical curve is plotted with the best four distributions, Nakagami, Weibull, Gamma and Rayleigh. The error of each distribution to approach the empirical is given in Fig. 4.5(bottom). The Rayleigh distribution has the highest error for wind speeds at 5 m/s

and the gamma distribution close to 8-7 m/s. The error of Weibull and Nakagami distributions is quite small (0.02) for wind speed below 15 m/s and it is close to zero for wind speeds greater than 15 m/s.

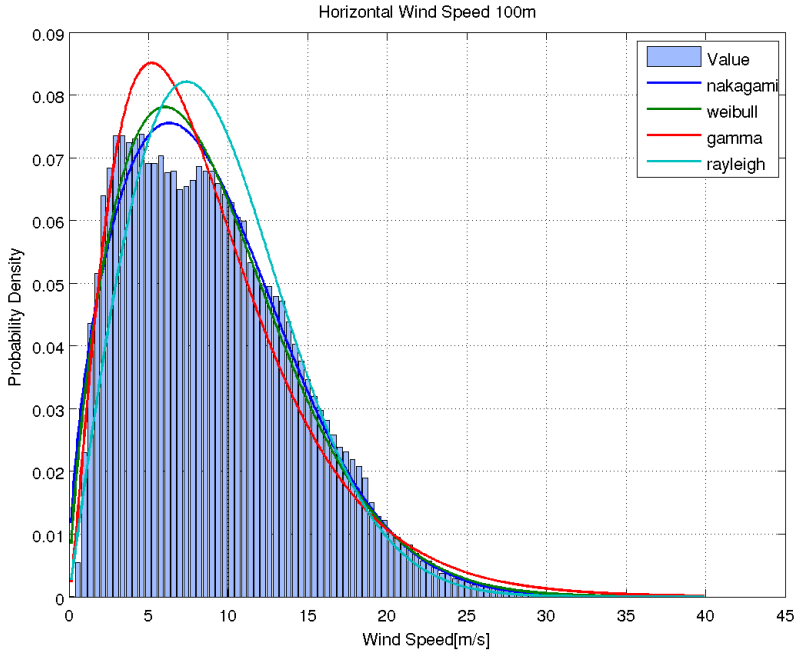


FIGURE 4.4: Histogram of horizontal wind speed and the best four fitted distributions.

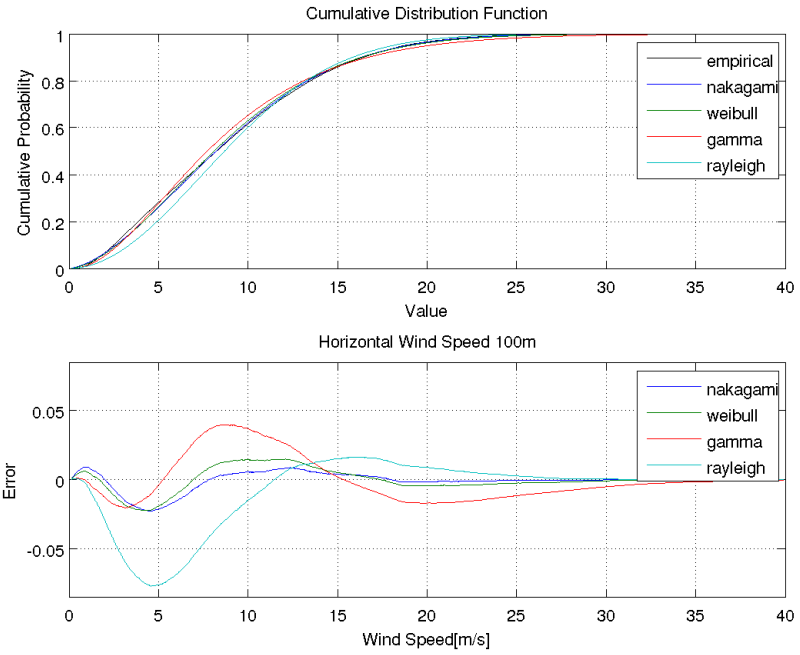


FIGURE 4.5: (Top) Cumulative distributions of the horizontal wind speed, (bottom) fitting error of each distribution.

### 4.1.3 Weibull distribution

The Weibull (2-parameter) distribution is the most widely used distribution for the analysis of 10 min average wind speeds [7], [37]. This continuous probability distribution is a generalized form of the Rayleigh distribution. The Weibull probability density function (pdf) f and the cumulative density function (cdf) F are:

$$f(U,c,k) = \left(\frac{k}{c}\right)\left(\frac{U}{c}\right)^{(k-1)} e^{[(-\frac{U}{c})^k]} \tag{4.2}$$

$$F(U,c,k) = 1 - e^{[-(\frac{v}{c})^k]} \tag{4.3}$$

where U is the horizontal wind speed, k is the Weibull shape parameter and c is the Weibull scale parameter (m/s).

The monthly Weibull probability density function calculated from the wind speeds at 100 m asl are shown in Fig. 4.6. During the summer months, the distribution is narrower (low variety of wind speeds) and has its peak at low wind speeds at around 5 m/s. For autumn and winter the distribution is much wider which represents high variety of wind speeds. The peak of the distributions is shifted towards to higher wind speeds around 10 m/s.

The monthly Weibull cumulative density function from the wind speeds calculated at 100 m asl is illustrated in Fig. 4.7. The results indicate e.g. only 10 % of the wind speeds are higher than 10 m/s during August, while this value increases to 60 % during March and October.

The calculation of scale (c) and the shape (k) parameters of Weibull distributions is critical important for estimation the Weibull distribution of wind speed. These two parameters control the Weibull distribution with different way. The scale parameter is proportional to median of wind speed. The shape parameter plays the role of stretching or shrinking the distribution.

The monthly variation of Weibull scale parameter for 8 different heights is given in Fig. 4.8. The Weibull scale parameter c is proportional to mean horizontal wind speed as it is shown in Fig. 4.1). August, June and May have the lowest values both for c and

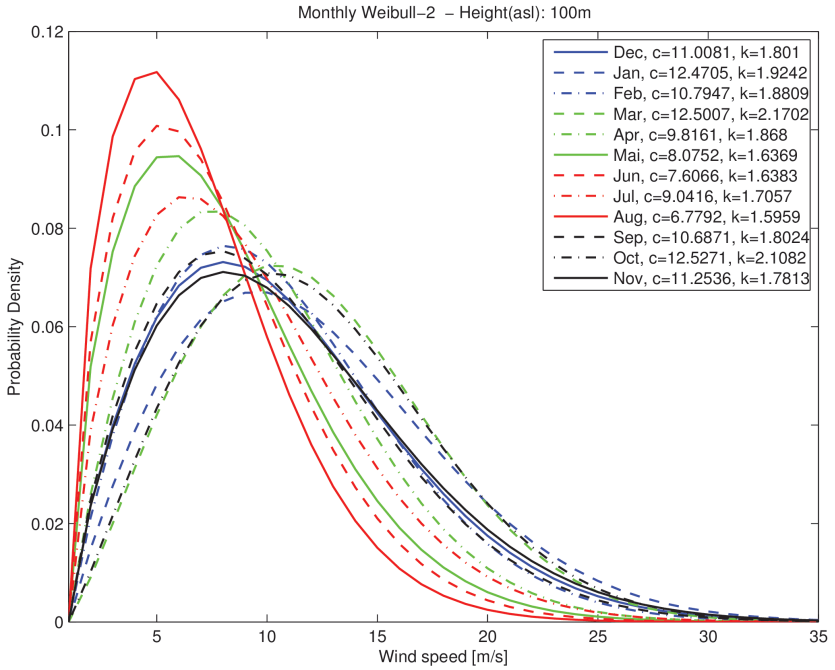


FIGURE 4.6: Monthly Weibull (2 parameters) probability density function for the wind speed at 100 m asl.

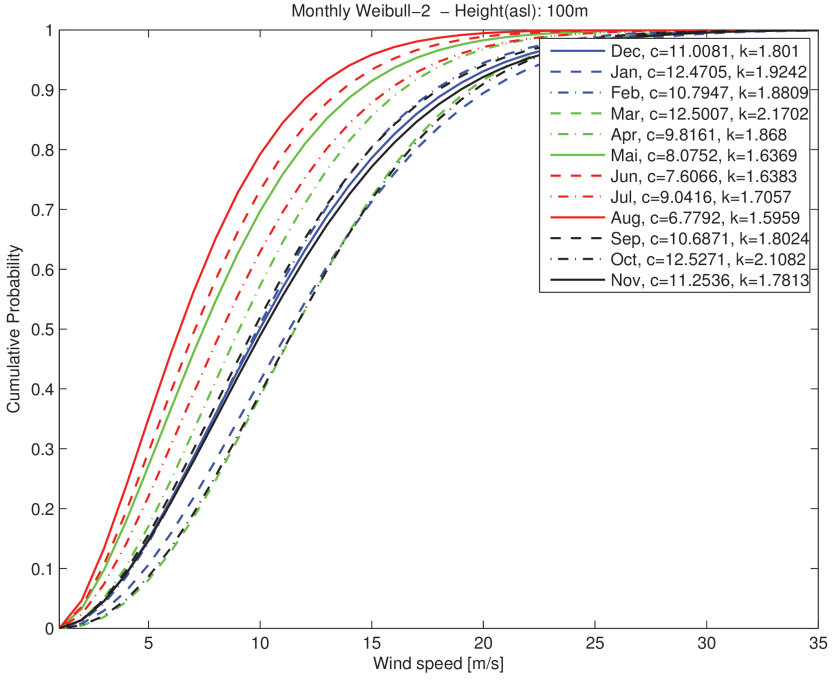


FIGURE 4.7: Monthly Weibull (2 parameters) cumulative probability function for wind speeds at 100 m asl.

mean wind speed in all heights. On the other hand, January, May and October have the highest values of c and the strongest mean wind speeds. The monthly variation of Weibull shape parameter for 8 different heights is illustrated in Fig. 4.9. The range of

shape parameter is between 1.4 and 2.3. It achieves the highest value in November at 200 m asl and the lowest value in August at 60 m asl.

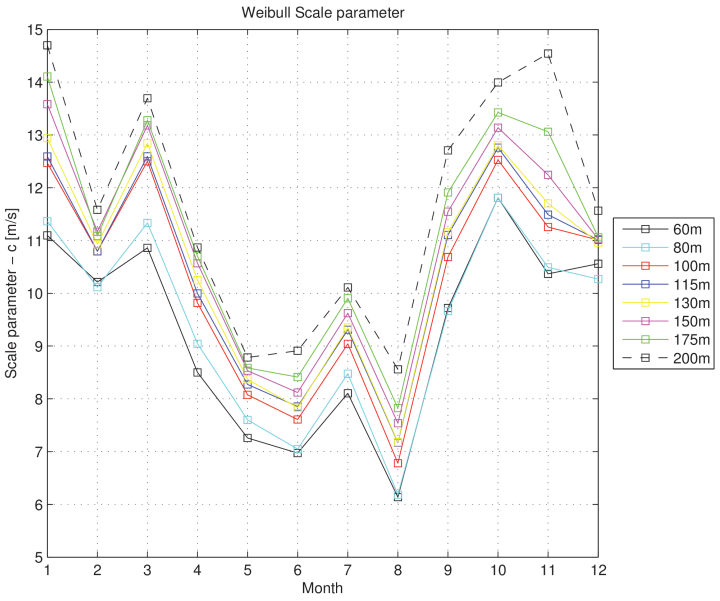


FIGURE 4.8: Monthly variation of Weibull scale parameter.

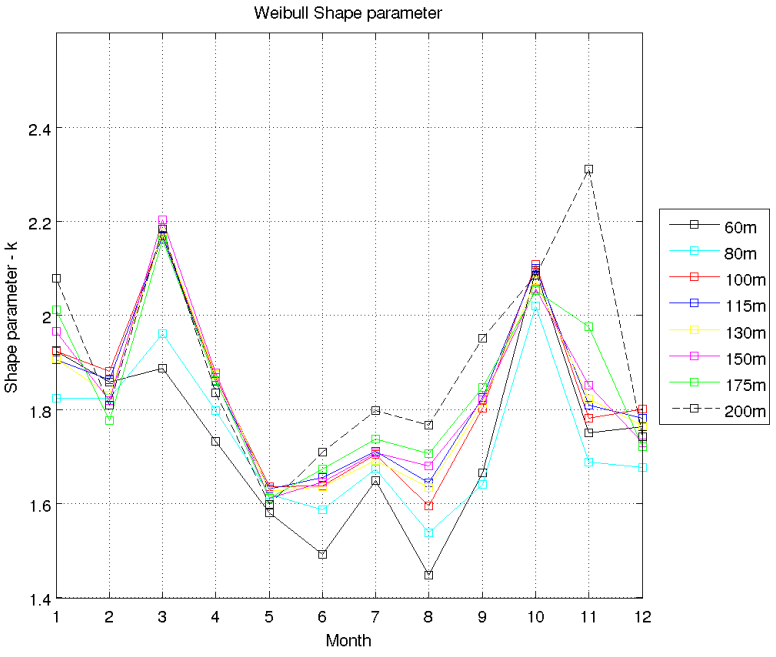


FIGURE 4.9: Monthly variation of Weibull shape parameter.

## 4.2 Vertical Wind Speed

In contrast to cup anemometer, lidar is able to measure the vertical component (w) of wind speed. The w is a fundamental parameter in atmospheric sciences as it is directly related to the vertical transport of heat, moisture and momentum fluxes.

Table 4.3 presents the main statistics for w at the 8 heights of lidar measurements at Storholmen for the period 2008-2012. There is a general increase of of mean and median of w with height which follows the increase of mean and median of horizontal wind speed with height as presented in Table 4.1. The mean and median of w take the lowest value (0.01 m/s and -0.12 m/s, respectively) at the lowest level 60 m asl and the highest values (0.09 m/s and 0.04 m/s, respectively) at 200 m asl. The standard deviation of w is rather uniform around 0.35 m/s, except for the lowest level of 60 m when it reaches 0.61 m/s.

| **Height (asl)** | **Mean [m/s]** | **Median [m/s]** | **Min [m/s]** | **Max [m/s]** | **Std [m/s]** |
|---|---|---|---|---|---|
| 60 m | 0.01 | -0.12 | -1.63 | 5.19 | 0.61 |
| 80 m | 0.02 | -0.05 | -1.55 | 3.85 | 0.37 |
| 100 m | 0.05 | -0.02 | -1.39 | 3.83 | 0.36 |
| 115 m | 0.08 | 0.01 | -1.34 | 3.65 | 0.35 |
| 130 m | 0.08 | 0.02 | -1.45 | 3.70 | 0.35 |
| 150 m | 0.08 | 0.03 | -1.60 | 3.03 | 0.33 |
| 175 m | 0.08 | 0.03 | -1.80 | 3.02 | 0.34 |
| 200 m | 0.09 | 0.04 | -2.01 | 2.81 | 0.34 |

TABLE 4.3: Statistics of vertical wind speed for the period 2008-2012

Following the method that was described in section 4.1.2, the list of different distributions fitted to the vertical wind speed data to find the 4 best distributions for the description of w. The best fitted distributions for w data for the 8 heights is the t location-scale.

The probability density function of t location-scale is described by:

$$f(w,v,\mu) = \frac{\Gamma\left(\frac{v+1}{2}\right)}{\sigma\sqrt{v\pi}\Gamma\left(\frac{v}{2}\right)}\left[\frac{v+\left(\frac{x-\mu}{\sigma}\right)^2}{v}\right]^{-\left(\frac{v+1}{2}\right)} \tag{4.4}$$

where w: vertical wind speed,

$\mu$: location parameter,

$\sigma$: scale parameter,

$v$: shape parameter,

$\Gamma$: Gamma function.

The t location-scale is used to model data distribution with outliers (heavy tails). For $v \to \infty$, it approaches the normal distribution and for $v \to 0$ it gives heavier tails.

The histogram of w at 100 m asl is shown together with the 4 best fitted distributions (t location-scale, generalized extreme value, logistic and normal) in Fig. 4.10. The histogram of w at 100 m asl is a not symmetric distributed since it has the peak value for slightly negative w (the median is -0.02 m/s) and an enhanced positive tail which explains the positive mean at 0.05 m/s. The corresponding cumulative distributions and the errors of each distributions are plotted in Fig. 4.11. It shows that t location-scale distribution has the lowest error for all values of w compared to normal, logistic and generalized extreme value distributions which have much higher error in fitting the w distribution. They clearly underestimate the values close to 0 and overestimate in particular the region between 0.3 and 0.7 m/s.

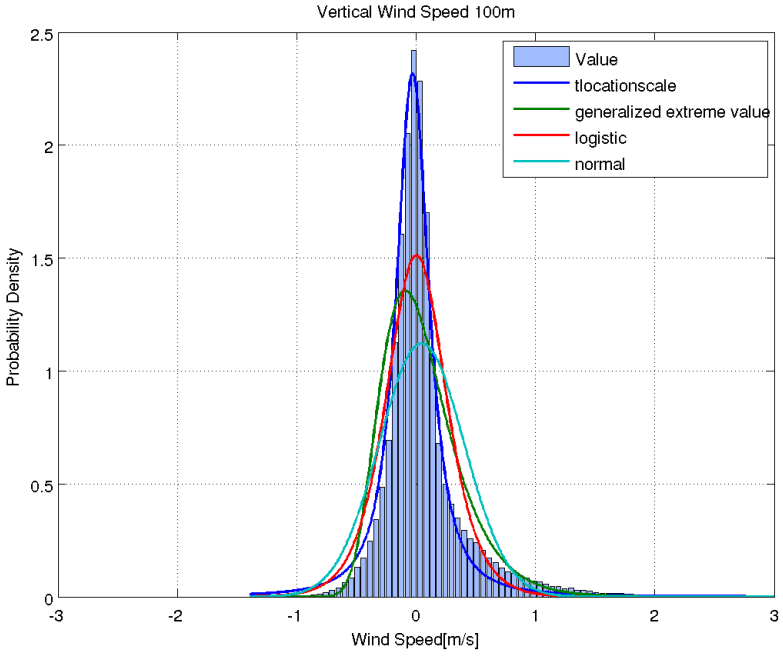


FIGURE 4.10: Histogram of vertical wind speed and the best four fitting distributions.

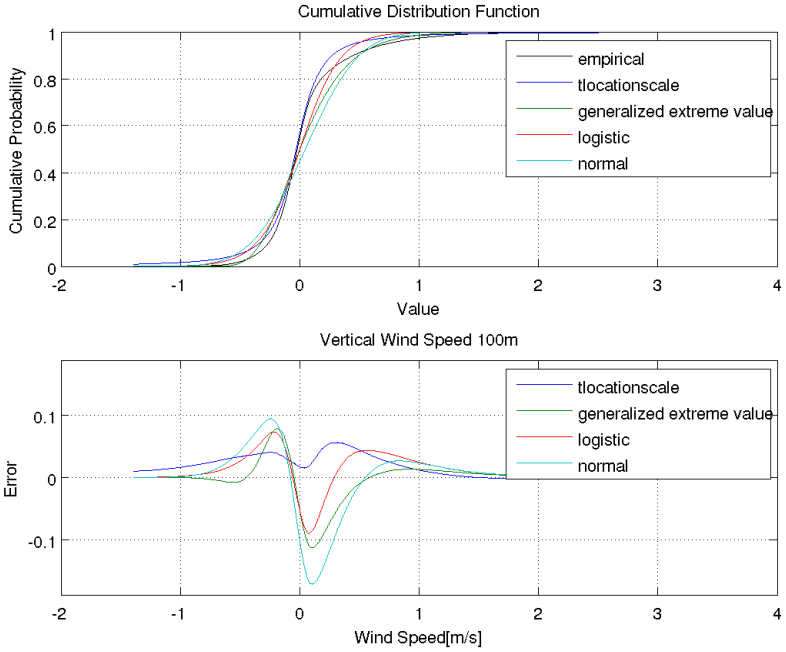


FIGURE 4.11: (Top) Cumulative distributions of the vertical wind speed, (bottom) fitting error of each distribution

## 4.3 Horizontal Turbulence Intensity

The horizontal turbulence intensity ($I_U$) is an important parameter in wind energy as is described in section 4.3.

The log-normal distribution is widely used to describe the turbulence intensity distribution in offshore areas [39]. In probability theory and statistics, a log-normal distribution is defined as a continuous probability distribution in which the logarithm of a random variable is normally distributed.

The probability density function of log-normal distribution is described by:

$$f(x, \sigma, \mu) = \frac{1}{x\sigma\sqrt{2\pi}} e^{-\frac{(lnx-\mu)^2}{2\sigma^2}} \tag{4.5}$$

where x is a positive variable,

$\mu$: log scale parameter,

$\sigma$: shape parameter.

Fig. 4.12 shows the log-normal distribution of turbulence intensity for different classes of wind speed at 100m asl. The parameters of the distribution were calculated again using the maximum likelihood estimates (MLEs). The results show a clear dependency of the turbulence intensity distribution on the wind speed. For increasing wind speed the center of distribution moves to lower turbulence intensities and the probability density increases. For wind speeds lower than 10 m/s, there is a decrease of turbulence intensity for an increase in wind speed. On the other hand, for wind speed greater than 10 m/s, for increasing the wind speed the turbulence intensity remains approximately constant.

Fig. 4.13 presents the monthly variation of $I_U$ and horizontal wind speed U at 100 m asl. The result indicates an anti-proportional relation between $I_U$ and U i.e. the maximum value of $I_U$ corresponds to minimum value of U during August. However, only the highest peaks of U during January, March and October do not correspond to the lowest values of $I_U$ which means that the perturbation of wind field is enough high during these months.

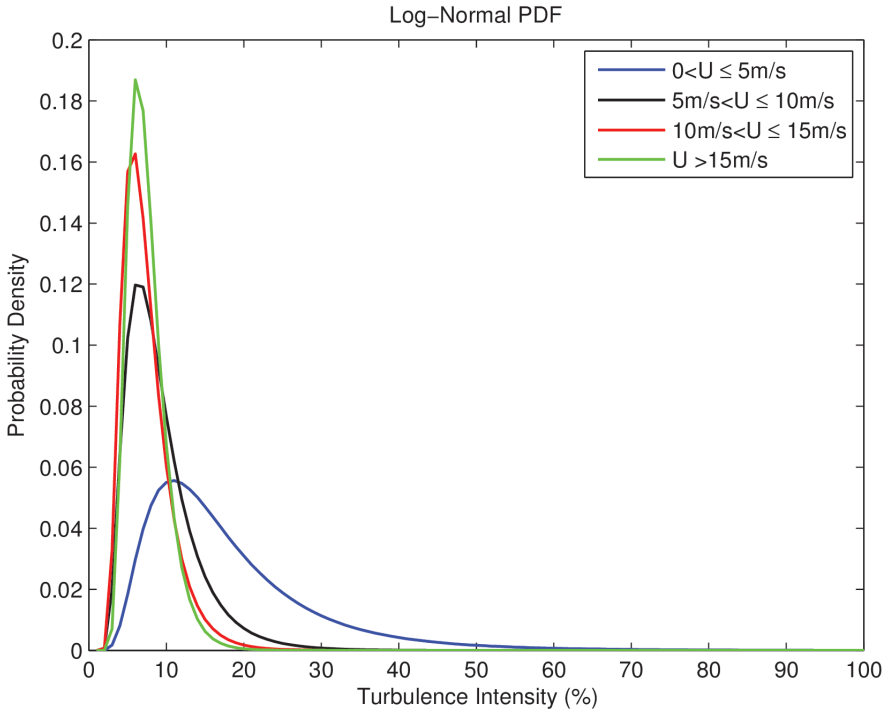


FIGURE 4.12: Log-normal distribution of the horizontal turbulence intensity $I_U$ for different classes of wind speed at 100 m asl.

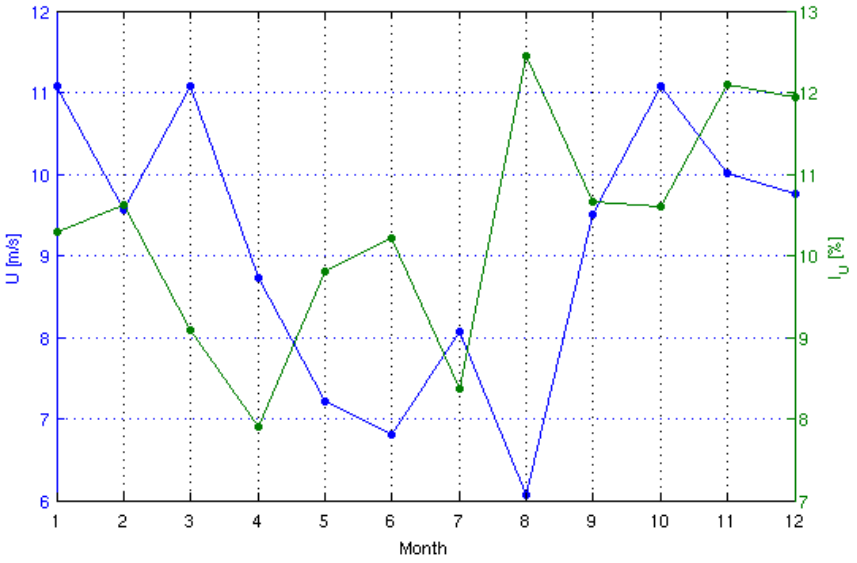


FIGURE 4.13: Monthly average values of $I_U$ and horizontal wind speed U at 100 m asl over the 4 years period (2008-2012).

## 4.4 TKE

As it is described in Chapter 2, TKE is an important parameter in boundary layer meteorology. In this analysis, the TKE was calculated based on the measured variances of the 3 components of wind speed using the Eq. 2.11.

For the investigation of TKE in the Havsul area, the observations are separated into two different direction ranges. Fig. 4.14 shows the location of Storholmen island and the line directed from 25° to 205° parallel to the coast.

Wind directions clockwise between 205° and 25° degrees are expected to represent undisturbed offshore conditions while the rest can be more or less influenced by the nearby land.

### 4.4.1 Offshore and Onshore TKE

In this section, the differences between offshore and onshore TKE have been investigated. For onshore conditions, a high frequency of low TKE and significant low frequency of high TKE are observed in Fig. 4.15. For offshore conditions, the frequency of low TKE decreases, and the frequency of high TKE increases in Fig. 4.16. This indicates that offshore winds are related to higher TKE compare to onshore winds.

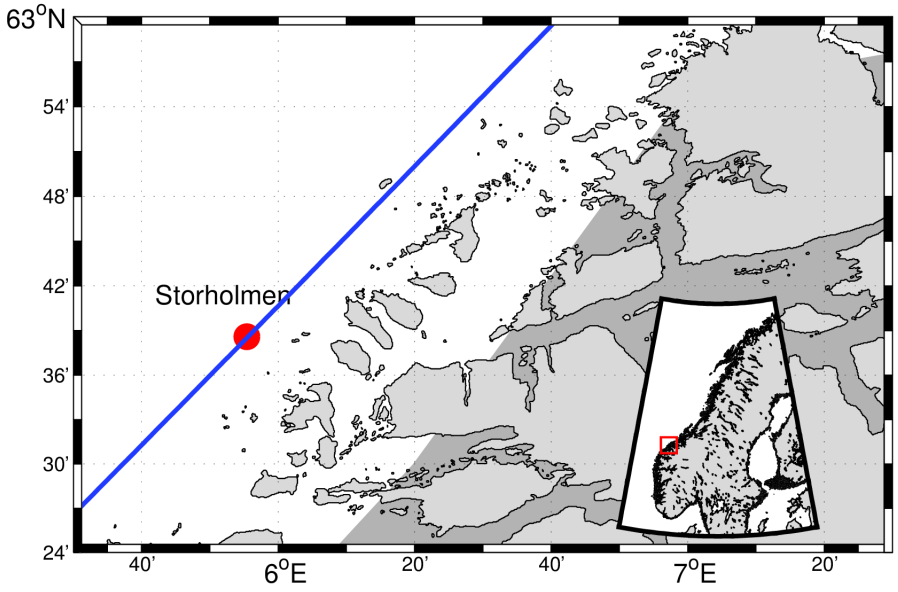


FIGURE 4.14: Map of Storholmen island and the parallel line (25° to 205°) to the coast.

### 4.4.2 Change of TKE with height

For the analysis of TKE with height, the offshore and onshore TKE classes are plotted for 8 different heights (1: 60 m, 2: 80 m , 3: 100 m , 4: 115 m, 5: 130 m, 6: 150 m, 7: 180 m, 8: 200 m asl).

Fig. 4.15 shows the occurrence of the different TKE classes for the different height levels. It illustrates that TKE lower than 0.6 $m^2/s^2$ dominates over all heights and represents ca. 90 % of cases. The occurrence of low TKE values increases with height. For instance, for $TKE < 0.2m^2/s^2$, the probability of occurrence raises from 50 % at 60 m to 70 % at 200 m.

The low values of TKE increases with height. The high TKE occurrence slightly decreases with height as e.g. the 7 % of TKE which is exceeding 0.8 $m^2/s^2$ at 60 m asl reduces to 4 % at 200 m asl.

Fig. 4.16 presents the variation of different onshore TKE classes with height. It shows that $TKE < 0.6m^2/s^2$ is the most frequent class of TKE over all heights since it

represents ca. 80-85 % of TKE. The low TKE increases with height while the 35 % of TKE which is lower than $0.2m^2/s^2$ at 60m asl increases at 40 % at 200 m asl. This increase of low TKE occurrence with height is much smaller compare to onshore wind. On the other hand, the high TKE decreases with height since the 20 % of TKE which is greater than 0.8 $m^2/s^2$ at 60 m asl reaches the 17 % at 200 m asl. Both for onshore and offshore wind speeds, the magnitude of decrease of high values of TKE with height is approximately the same (3%).

The results of separation of offshore and onshore TKE with height show that the flow coming from ocean is more turbulent (higher TKE) compare to the flow coming from land since offshore winds are stronger with high wind shear which can generate high TKE. In addition for onshore winds, for increasing the height the values of TKE becomes lower which indicates that the frictional effects play an important role in TKE. For offshore winds, for increasing the height , the classes of TKE remain nearly constant which shows that the waves do not effect significantly the TKE with height.

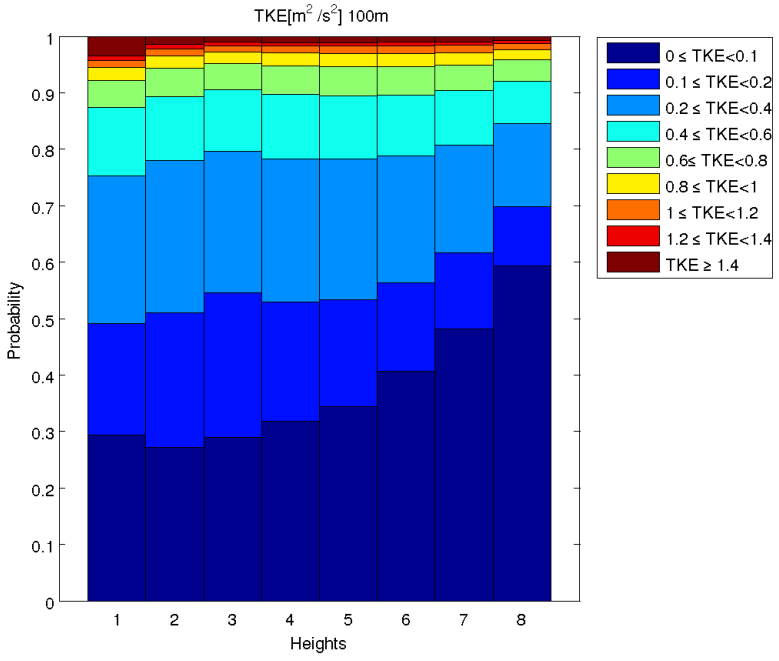


FIGURE 4.15: The change of different onshore TKE classes with height over the 4 years period (2008-2012).

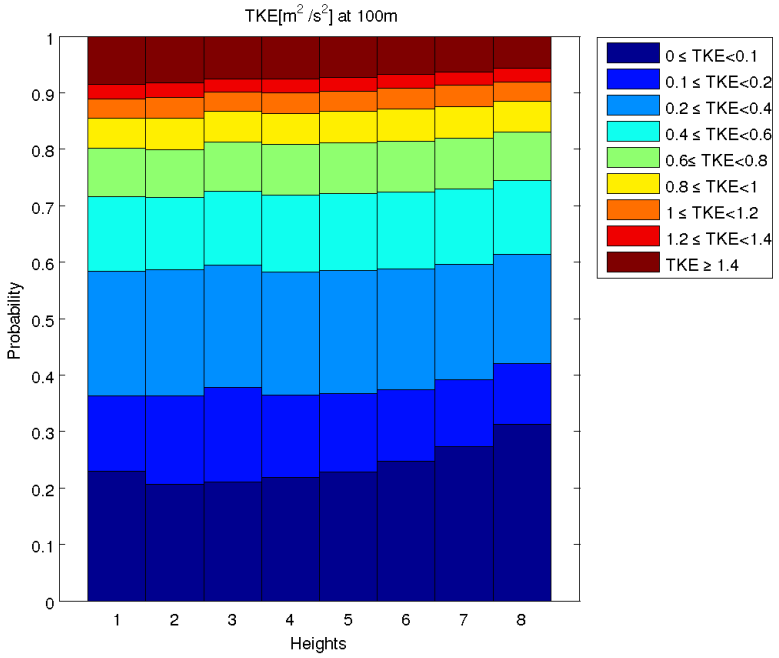


FIGURE 4.16: The change of different offshore TKE classes with height over the 4 years period (2008-2012).

### 4.4.3 Seasonal Variation of TKE

For the investigation of seasonal variation of TKE, the offshore and onshore TKE classes are plotted for the different months for the 4 year period 2008-2012.

Fig. 4.17 illustrates the monthly variation of different TKE classes at 100 m asl for onshore wind speeds. From April to August, low values of TKE, less than 0.4 $m^2/s^2$, represent approximately the 90% of TKE. During winter and autumn, values of TKE between $0.2m^2/s^2$ and $0.6m^2/s^2$ occur with 80-90% frequency.

Fig. 4.18 presents the monthly variation of offshore TKE. During winter, autumn and early spring (March), 50-70 % of TKE is lower than 0.6 $m^2/s^2$ and only 15-25 % is higher than 1 $m^2/s^2$ During the spring months, April, May and summer, 90 % of TKE is lower than 0.6 $m^2/s^2$ and a small percentage of TKE (ca. 2-4 %) represents values greater than 1 $m^2/s^2$.

Comparing the figures 4.17 and 4.18, there is a significant increase of high values of TKE (greater than $1m^2/s^2$) during the winter, autumn and march from spring for offshore winds. This result indicates that offshore winds can generates higher values of TKE than onshore winds, again due to the average higher wind speeds.

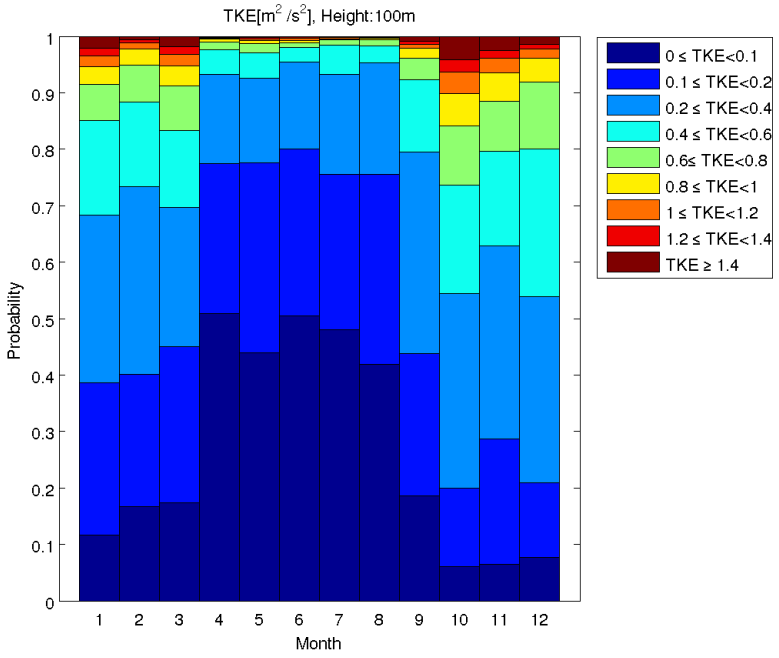


FIGURE 4.17: Onshore monthly stacked bars for different classes of TKE at 100 m asl over the 4 years period (2008-2012).

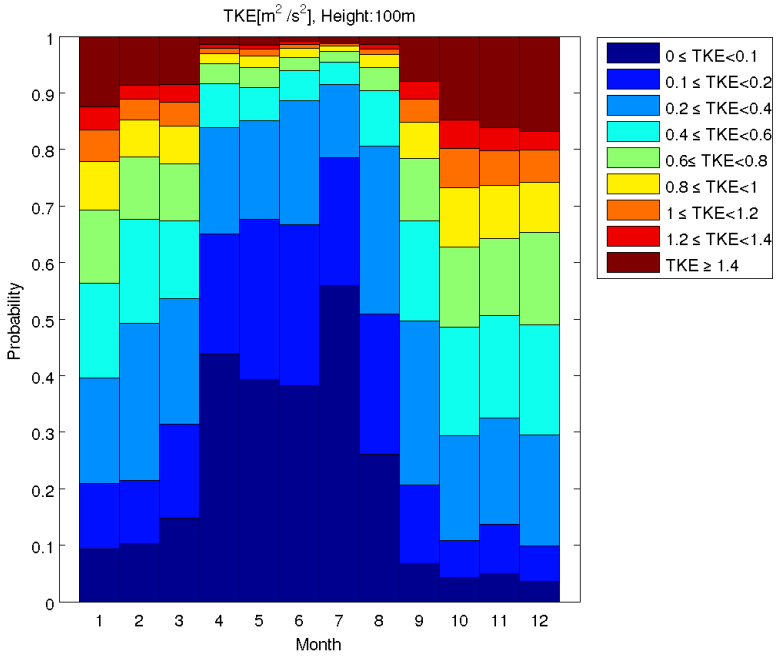


FIGURE 4.18: Offshore monthly stacked bars for different classes of TKE at 100 m asl over the 4 years period (2008-2012).

### 4.4.4 TKE and Turbulence Intensity

TKE is a parameter which is strongly connected to turbulence intensity. From Chapter 2, TKE is a function of $I_U$ and $I_w$ :

$$TKE = \frac{U^2}{2} {I_U}^2 + \frac{U^2}{2} {I_w}^2 \tag{4.6}$$

Eq. 4.6 shows that the turbulence parameters of TKE, $I_U$ and $I_w$ are correlated with a quadratic relationship.

Fig. 4.19 shows the relation between TKE and $I_U$ for different classes of wind speed. For wind speeds lower than 5 m/s, the TKE and $I_U$ are largely uncorrelated. For wind speeds above 5 m/s the correlation increases and the relation between TKE and $I_U$ becomes clearly quadratic.

The corresponding relation between TKE and $I_w$ for different thresholds of wind speeds is given in Fig. 4.20. The result indicates that the relation between TKE and $I_w$ is not pronounced since these parameters have lower correlation for all the wind speeds classes.

### 4.4.5 TKE and Wind Shear

In this section, the wind power exponent $\alpha$ is used to describe the wind shear and its relation to TKE. The dependency between TKE and $\alpha$ for different wind speeds is shown in Fig. 4.21. The $\alpha$ exponent is calculated between 60 m and 150 m asl. For low wind speeds (less than 5 m/s), $\alpha$ varies between -2 and 2 and the most of TKE values are low close to 0. Increasing the wind speed, $\alpha$ decreases and TKE gets higher values. Finally, for strong wind speed, greater than 15 m/s, the $\alpha$ values are grouped between 0 and 0.5 and TKE achieves the highest values. The results show a clear relation between TKE, $\alpha$ and wind speed since TKE increases for increasing wind speed and decreasing the range of the $\alpha$ exponent. In addition for the highest wind speeds, $\alpha$ tends to approach the neutral condition threshold of 1/7 or 0.143.

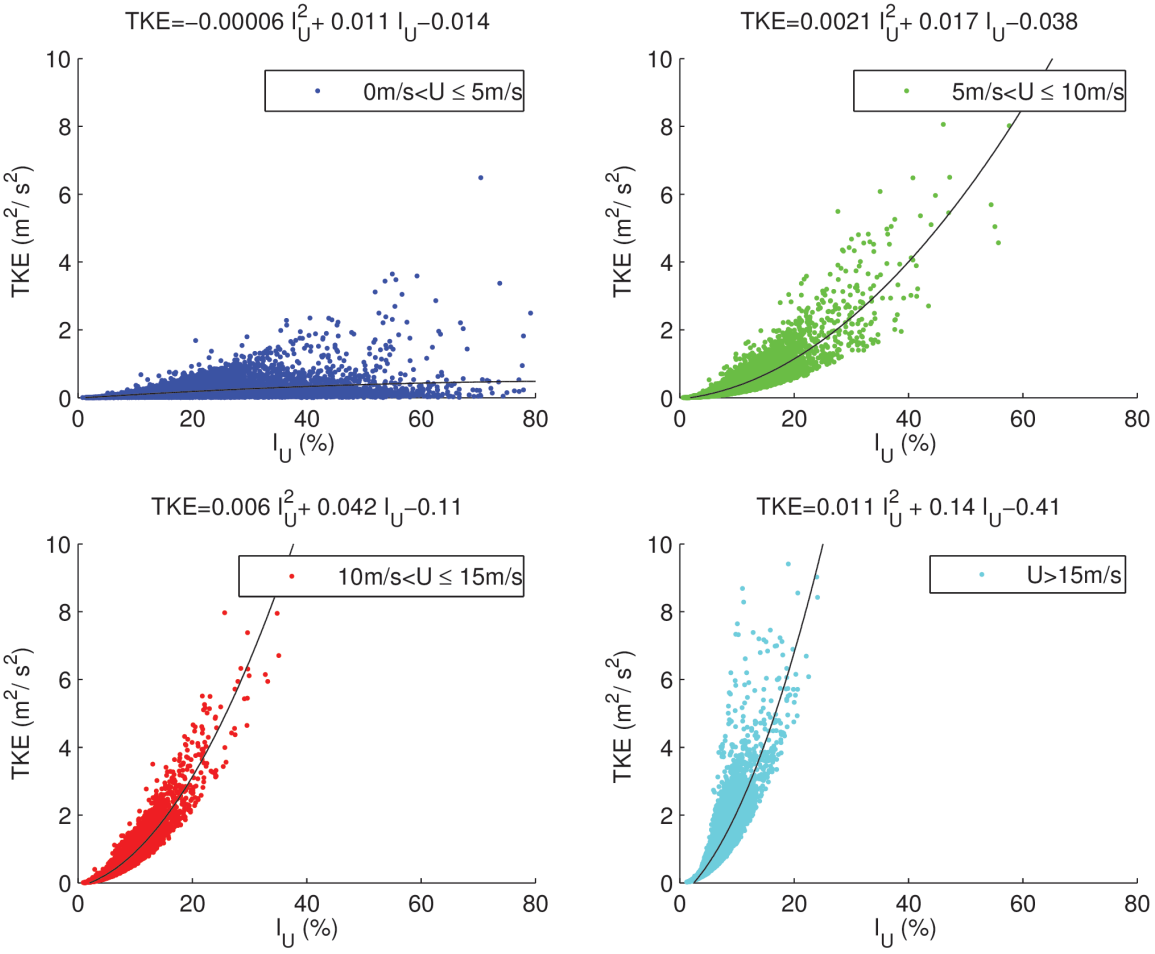


FIGURE 4.19: TKE as a function of $I_U$ for a different wind speeds.

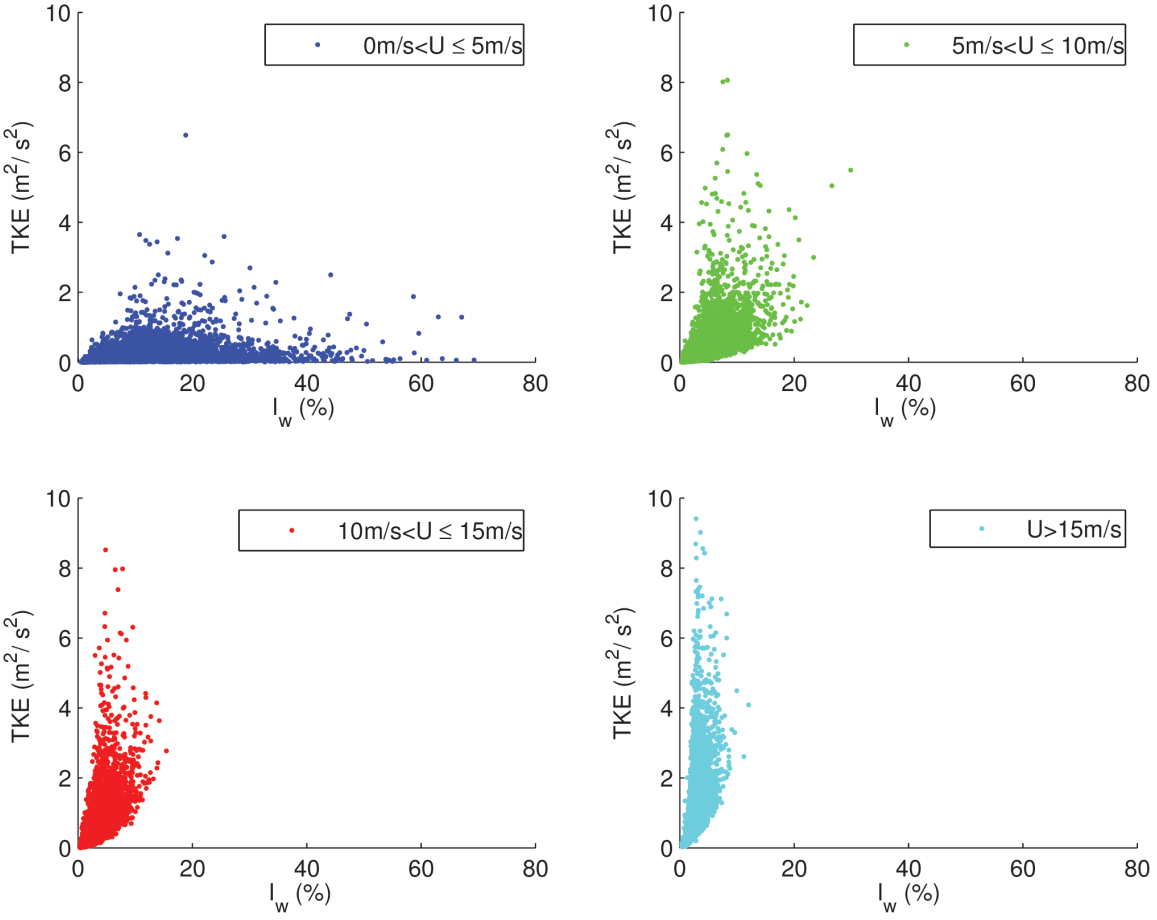


FIGURE 4.20: TKE as a function of $I_w$ for a different wind speeds.

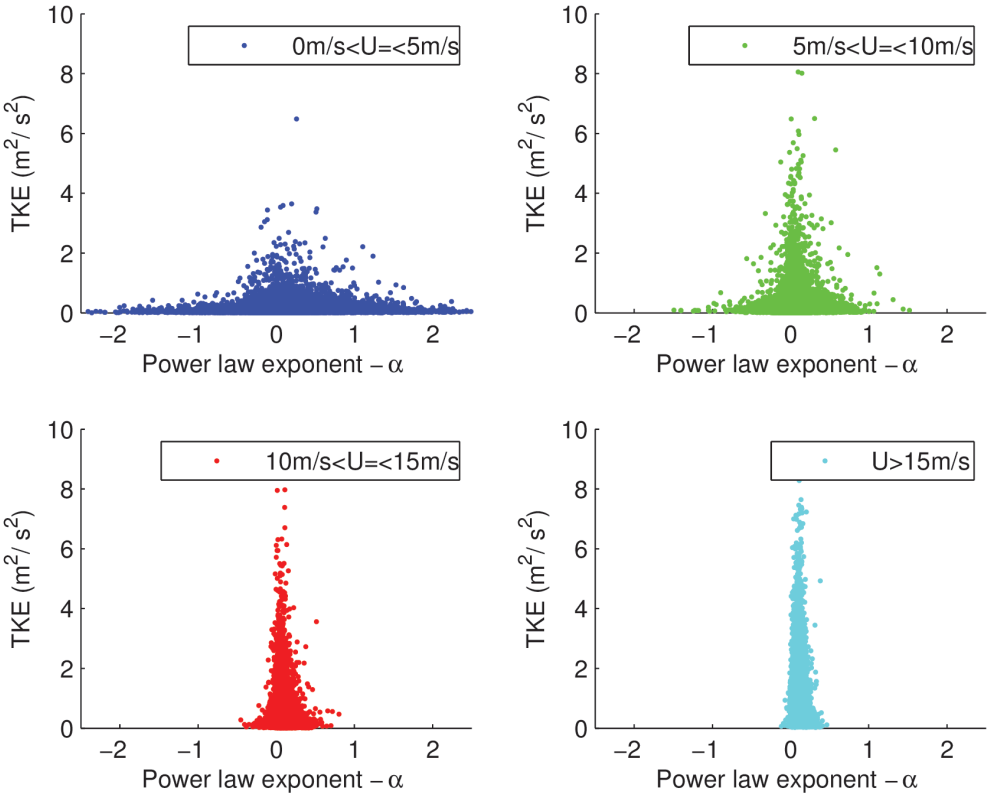


FIGURE 4.21: TKE as a function of wind power exponent $\alpha$ for a different wind speeds. The $\alpha$ is calculated between 60 m and 150 m asl.

# Chapter 5

# Offshore Wind Profiles

## 5.1 Offshore Wind Profiles and Turbulence Parameters

In this section, the relation between the offshore wind profiles and the turbulence parameters is investigated. For this analysis, the 10 minutes average wind profiles from the lidar are classified into different classes of $I_U$, $I_w$, $I_{3D}$ and TKE. The motivation was the classification of atmospheric stability based on turbulence parameters by Wharton and Lundquist in section 2.4.4. While these parameters are strongly connected to atmospheric stability, they will also effect wind profiles and in particular wind shear. For the investigation between wind shear and turbulence parameters, the average wind profiles are normalized to 1 at 100 m asl which is the typical level for the nacelle heights of state of art wind turbines.

Due to the processes discussed in the section 3.1.7, the data availability of the lidar decreases with the height. For the following analysis only data of complete offshore wind profiles between 60 m and 150 m asl have been used, leaving a total number of 75249 profiles for the presented investigation.

Results of this section have been the main source for the scientific publication "Experimental characterization of the marine atmospheric boundary layer in the Havsul area, Norway" by Christakos, K., J. Reuder, and B. Furevik, submitted to Energy Procedia, Elsevier (see Appendix B).

### 5.1.1 Horizontal Turbulence Intensity

As described in section 4.3, the probability density function of horizontal turbulence intensity shows a distinct dependency on wind speed since there is a general decrease of turbulence intensity for increasing wind speed (Fig. 4.12).

The average wind profiles are classified into different $I_U$ classes in Fig. 5.1. There is a clear dependency between $I_U$ and the averaged profiles. For $I_U$ higher than 6% (68% of the data - 51396 wind profiles), an increase of horizontal wind speed is connected to a decrease of $I_U$. For $I_U$ lower than 9% (62% of the data - 46663 wind profiles) the wind profiles are grouped between 10 m/s and 12 m/s.

For a better understanding of the dependency between wind shear and $I_U$, the wind profiles have been normalized to 1 at 100 m asl in Fig. 5.2. The results also show a clear

dependency of wind shear on $I_U$. For decreasing $I_U$, the wind shear increases. However, for $I_U$ greater than 20% (8.77% of the data - 6603 profiles), which represents mainly low wind speeds (2-3 m/s), the normalized profile shows an extreme wind shear at the highest levels (i.e. 130-150 m asl).

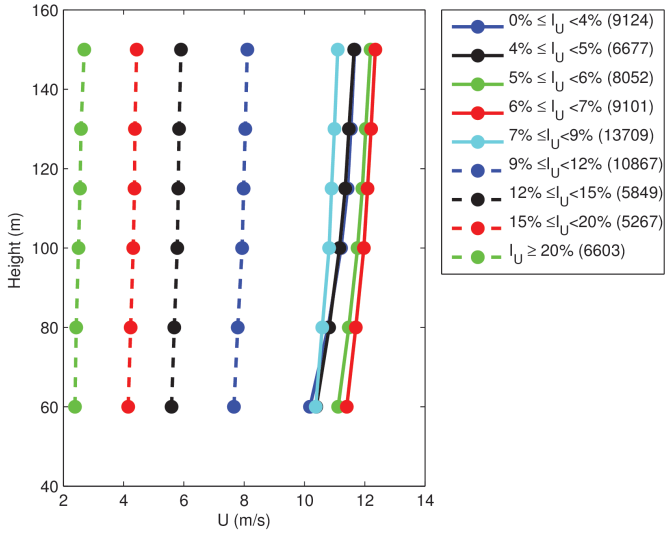


FIGURE 5.1: Average wind profiles for different classes of $I_U$ at 100 m asl.The number of profiles for each class is given in parentheses.

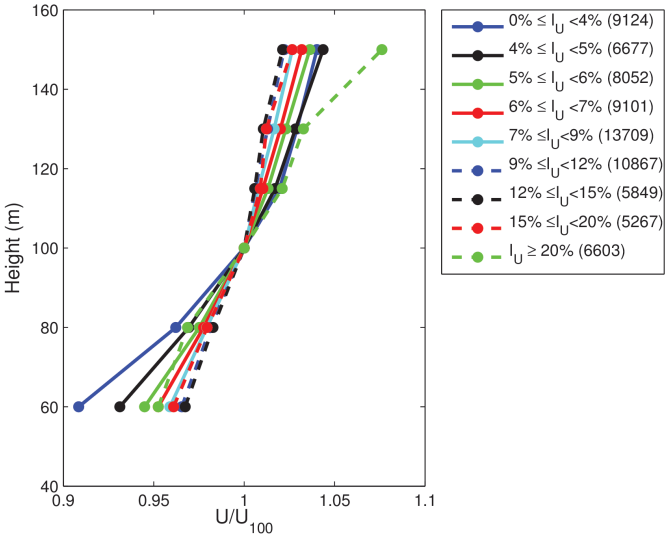


FIGURE 5.2: Normalized wind profiles for different classes of $I_U$ at 100 m asl. The number of profiles for each class is given in parentheses.

### 5.1.2 Vertical Turbulence Intensity

Wharton and Lundquist (2012) [5] suggested that also the vertical turbulence intensity ($I_w$) can be used for the classification of atmospheric stability. Fig. 5.3 presents the average profiles for different classes of $I_w$ at 100 m asl. For $I_w$ higher than 4% (41.63% - 31333 wind profiles), an increase of $I_w$ is related to a decrease of the average wind speed. For $I_w$ lower than 4% (58% of the data - 43916 profiles), the profiles are closely grouped again (as the case of $I_U$) between 10 m/s and 12 m/s.

Fig. 5.4 illustrates the corresponding normalized profiles at 100 m asl. For lower levels (i.e. below 100 m asl), $I_w$ increases with decreasing the wind shear. For higher levels (i.e. above 100 m asl) the dependency between $I_w$ and wind shear is distinctly weaker.

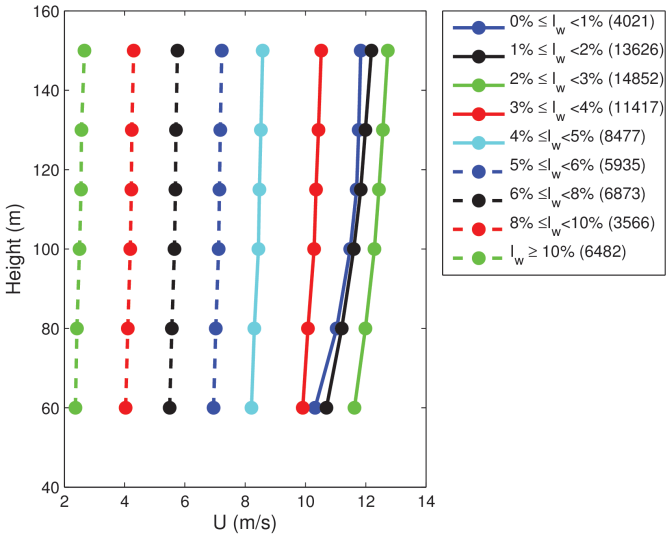


FIGURE 5.3: Average wind profiles for different classes of $I_w$ at 100 m asl. The number of profiles for each class is given in parentheses.

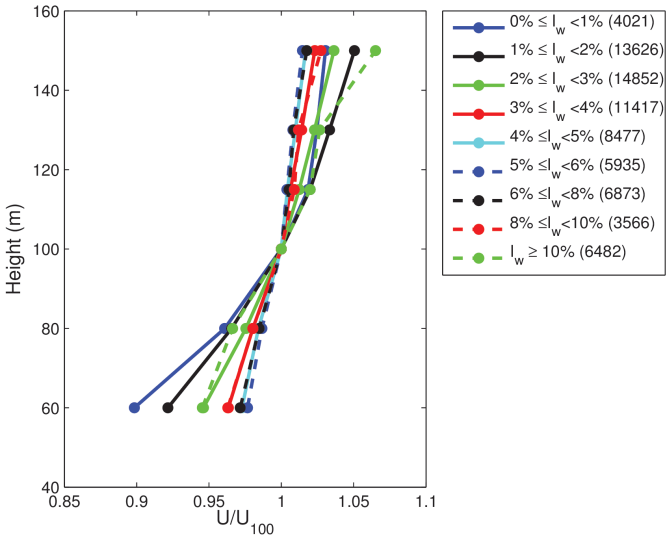


FIGURE 5.4: Normalized wind profiles for different classes of $I_w$ at 100 m asl. The number of profiles for each class is given in parentheses.

### 5.1.3 Turbulence Kinetic Energy

TKE is an important parameter in boundary layer meteorology since is associated with the energy of 3 dimensional eddies in turbulent flow. As described in section 2.3.5, buoyancy and wind shear are the main sources of TKE. Fig. 5.5 shows average profiles of wind speed for different classes of TKE at 100 m asl. The figure shows a clear dependency between TKE and the average wind profiles. The lower the wind speed, the lower the TKE. For values of TKE greater than $1.4m^2/s^2$ (4.7% - 3577 profiles), the average wind speed is above 16 m/s. For TKE values below $0.1m^2/s^2$ (28.25% - 21263 profiles), the average wind speed is with 4-7 m/s distinctly lower. This result indicates that wind shear is the main TKE production term in the MABL.

For a closer investigation of the relationship between TKE and wind shear, the profiles were normalized to 1 at 100 m asl in Fig. 5.6. For lower levels, below 100 m asl, there is a decrease of wind shear for increasing TKE. For higher levels, above 100 m asl, the normalized wind shear is nearly independent from TKE.

Fig. 5.7 shows the monthly average values of TKE and horizontal wind speed U at 100 m asl over the 4 years period (2008-2012). The results show that U and TKE are highly correlated. This result indicates again that the TKE in the lowest part of the MABL is mainly generated mechanically by wind shear.

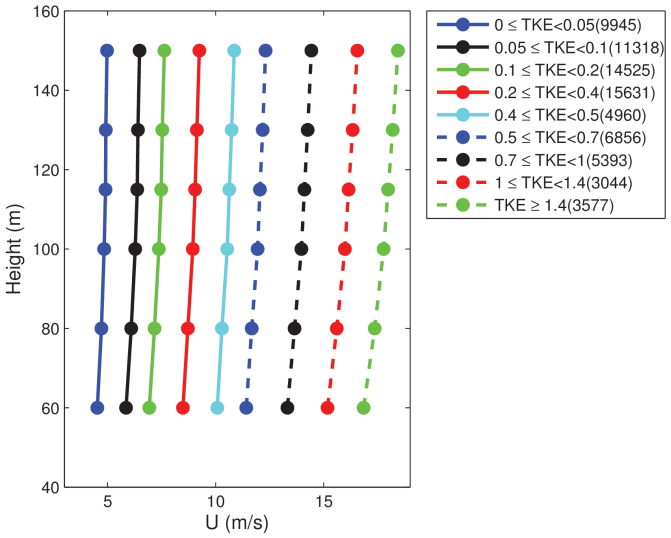


FIGURE 5.5: Average wind profiles for different classes of $TKE$ at 100 m asl. The number of profiles for each class is given in parentheses.

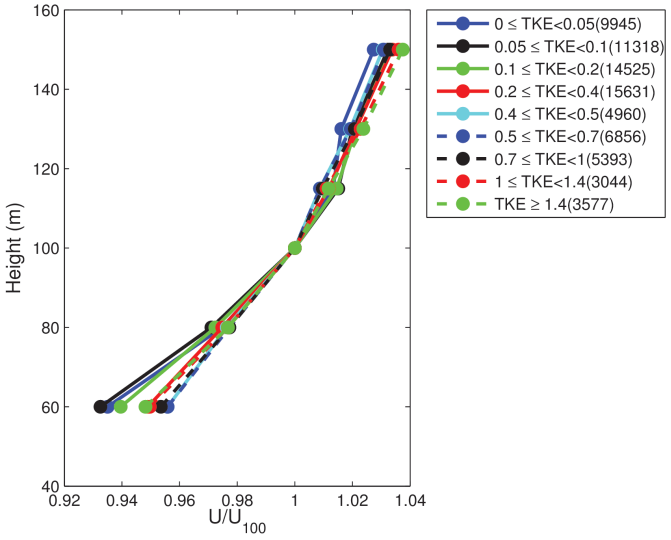


FIGURE 5.6: Normalized wind profiles for different classes of $TKE$ at 100 m asl. The number of profiles for each class is given in parentheses.

### 5.1.4 3D Turbulence Intensity ($I_{3D}$)

As described in 2.3.6, the 3D turbulence intensity ($I_{3D}$) is a function of TKE and MKE of the flow. This parameter present the turbulence intensity of the 3D velocity vector as shown in Eq. 2.14. Its behavior is quite similar to that of the horizontal and vertical turbulence intensity.

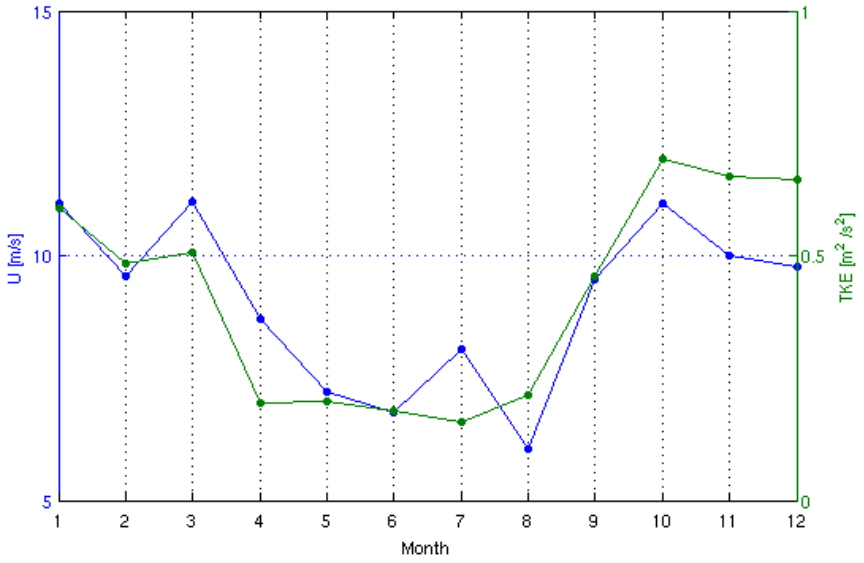


FIGURE 5.7: Monthly average values of $TKE$ and horizontal wind speed U at 100 m asl over the 4 years period (2008-2012)

Fig 5.8 shows the average wind profiles for different $I_{3D}$ classes. It shows a clear dependency between $I_{3D}$ and profiles. For $I_{3D}$ higher than 6% (73.88% of the data - 55595 wind profiles), an increase of horizontal wind speed is related to decrease of $I_{3D}$. For $I_{3D}$ below 9% (54.87% of the data - 41293 wind profiles) the wind profiles are grouped between 10 m/s and 12 m/s.

For a further investigation between wind shear and $I_{3D}$, the wind profiles have been normalized to 1 at 100 m asl in Fig. 5.9. The results shows a general increase in wind shear for decreasing $I_{3D}$. For $I_{3D}$ higher than 20% (11.05% of the data - 8313 profiles), which is related to low values of wind speed (i.e. 2-3 m/s), the normalized profile shows a distinctly enhanced wind shear at 130-150 m asl.

The results show that $I_{3D}$ can also be used to describe the turbulence intensity of wind field while it gives quite similar results with the traditional turbulence intensities of $I_U$ and $I_w$.

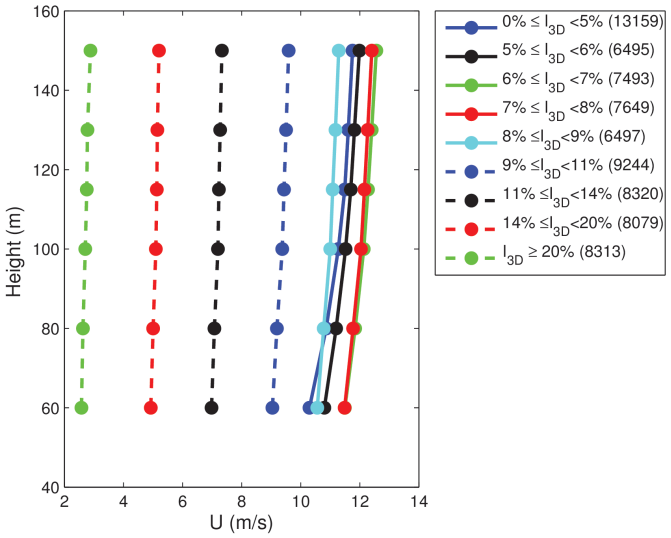


FIGURE 5.8: Average wind profiles for different classes of $I_{3D}$. The number of profiles for each class is given in parentheses.

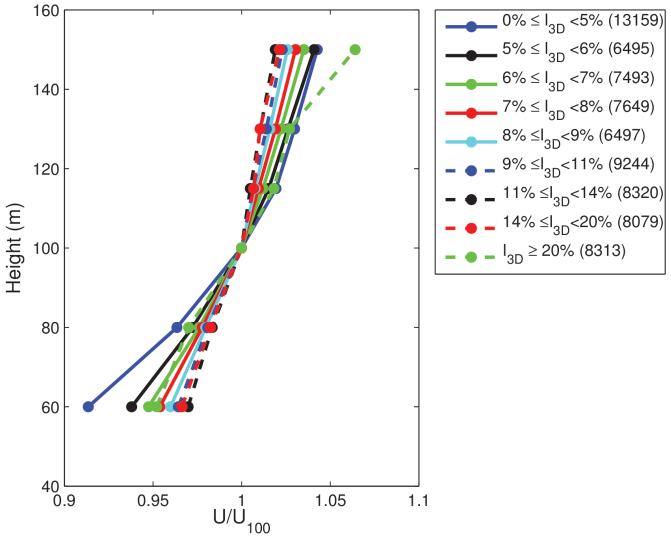


FIGURE 5.9: Normalized wind profiles for different classes of $I_{3D}$. The number of profiles for each class is given in parentheses.

## 5.2 Vertical Wind Speed

For the investigation of potential effects of flow distortion from the island of Storholmen on offshore wind profiles, the vertical wind speed is used to classify the wind profiles. Due to the low data availability of the lidar at high levels, only complete wind profiles (75249) between 60 m and 150 m asl have been used for this analysis.

Fig. 5.10 illustrates the average wind profiles for different classes of w at 100 m asl. It shows that the wind profiles are closely related to w. More specific, there is a clear separation of 4 different groups of offshore wind profiles with opposite direction of w. The first group (blue profiles) includes wind profiles for high positive w, greater than 0.4 m/s and high negative w, lower than -0.2 m/s and it represents horizontal wind speeds between 10-12 m/s. The second group (black profiles), includes wind profiles for positive w between 0.2 m/s and 0.4 m/s and negative w between -0.2 m/s and -0.1 m/s which are grouped for U $\sim 9m/s$. The third group (red profiles), includes wind profiles for positive w between 0.1 m/s and 0.2 m/s and negative w between -0.1 m/s and -0.05 m/s which are grouped for U $\sim 8m/s$. Finally, the fourth group (green profiles), includes wind profiles for w between -0.05 m/s and 0.05 m/s which are grouped for U $\sim 7 - 7.5m/s$.

The results indicate a possible effect of flow distortion from the island on the wind profiles. The wind profiles are closely grouped into nearly opposite classes of w. This result shows that the wind direction is connected to w. For a better understanding of the relation between wind direction and w, we used Fig. 5.11. It illustrates that for opposite wind directions over an island, the w changes direction (from positive to negative) as well.

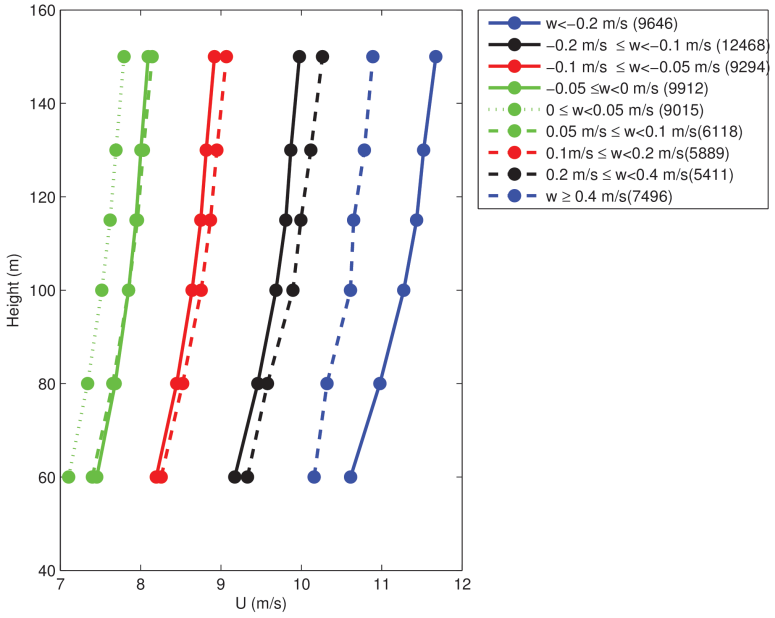


FIGURE 5.10: Average wind profiles for different classes of vertical wind speed (w). The number of profiles for each class is given in parentheses.

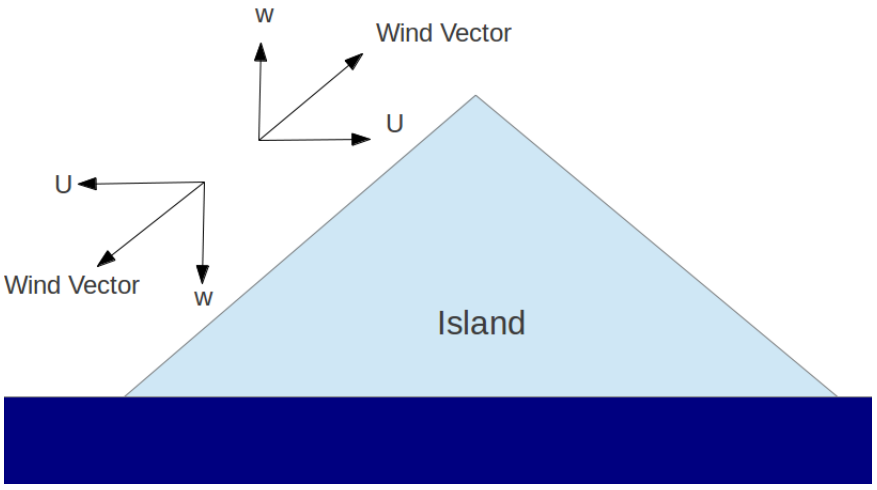


FIGURE 5.11: Horizontal and vertical components of wind vector over an island for opposite wind vectors.

## 5.3 Offshore Wind Profiles and Temperature

In this section, we investigate the effect of temperature (T) on offshore wind profiles. The temperature measurements at the nearly meteorological mast of Ona are used as another proxy for atmospheric stability. The average profiles have also been grouped with respect to this temperature assuming that the T at Ona and Storholmen is nearly the same. A number of 46752 complete lidar wind profiles from 60 m to 150 m asl with temperature measurements at 3 m agl have been used for this analysis.

Fig. 5.12 presents the average wind profiles for different classes of temperature. It shows that the wind profiles are closely related to temperature. For T higher than $16°C$ (3.52 % of the data - 1649 wind profiles), the horizontal wind speed is lowest around 5 m/s. For T below $0°C$ (2.8 % of the data - 1312 wind profiles), the wind speed is more less constant with altitude indicating unstable conditions and efficient mixing. For T between $7°C$ and $10°C$, the wind profile has the highest wind speed $\sim$ 9-10 m/s.

Times series of surface sea temperature (SST) during the year 2008 in Havsul region are presented in Fig. 5.14. It shows that the minimum and maximum of SST are approximately $5.5°C$ and $16°C$ respectively. For air T less than the SST, a thermal circulation is generated where moist air rises over the warm ocean and mixes the lowest part of MABL. On the other hand, for air T greater than the SST, the moist air descends over cool ocean generating stable conditions. This indicates that wind profiles with

air temperature less than $5°C$ can be considered to represent unstable conditions and mixing, and profiles with air T higher than $16°C$ are related to stable conditions.

The normalized wind profiles show the dependency between wind shear and T even clearer in Fig. 5.13. For negative values of T, the normalized profile is close to $U/U_{100} \sim 1$ for each height which represents no wind shear. For high T greater than $16°C$, a distinctly enhanced wind shear appears which represents low wind speeds during stable conditions.

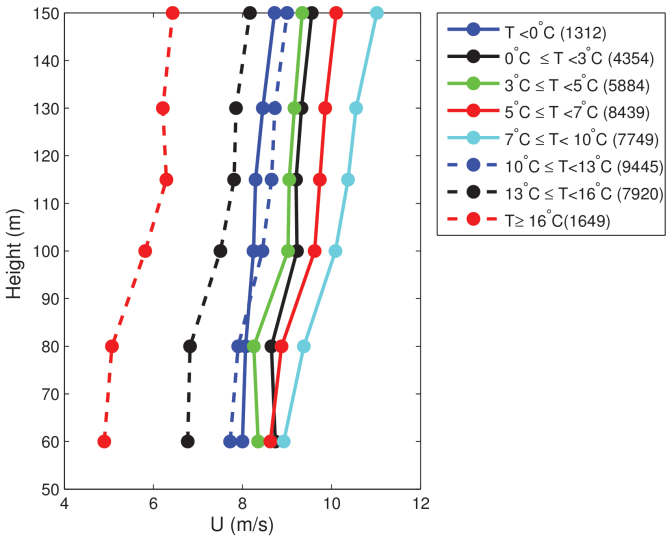


FIGURE 5.12: Average wind profiles for different classes of temperature. The number of profiles for each class is given in parentheses.

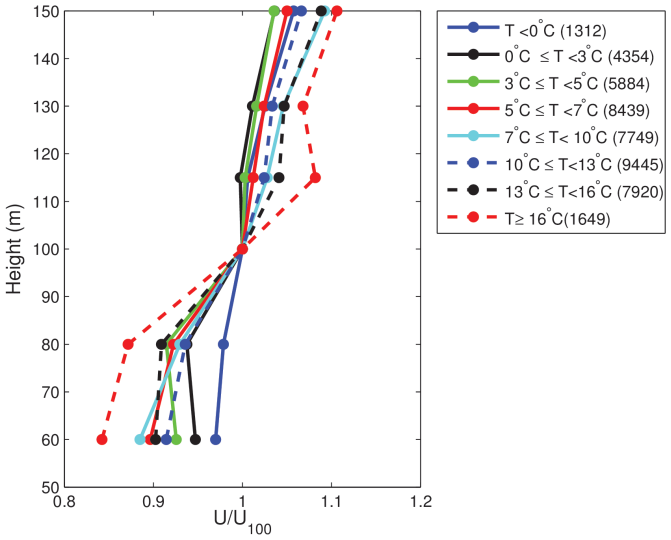


FIGURE 5.13: Normalized wind profiles for different classes of temperature. The number of profiles for each class is given in parentheses.

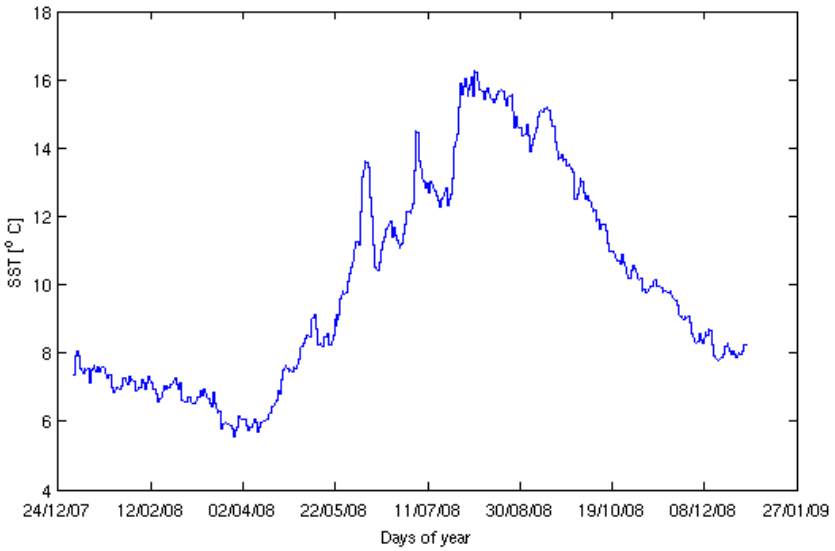


FIGURE 5.14: 6-hour sea surface temperature (SST) measurements in Havsul region for the year 2008. The data is provided by Mostafa Bakhoday Paskyabi.

## 5.4 Standard Deviation of the Horizontal Wind Direction

In this section, the standard deviation of the horizontal wind direction, $\sigma$ is applied as another proxy of atmospheric stability. The offshore wind profiles are separated into different Pasquill stability classes [40] based on $\sigma$. This classification was described in section 2.4.5. The main idea of this method is that for stable conditions the wind is steady with a low perturbation in wind direction (low $\sigma$): For unstable conditions the wind becomes unsteadier with higher perturbation in wind direction (high $\sigma$).

Fig. 5.15 presents the average wind profiles for different classes of $\sigma$. For $\sigma$ below 7.5 (stable conditions) the average wind profiles are closely grouped between 7 m/s and 9 m/s. For $\sigma$ greater than 7.5 (neutral and unstable conditions) the average wind profiles are grouped between 4.5 m/s and 5.5 m/s. The results show that during stable conditions the wind speed is higher compare to the neutral - unstable conditions.

For a further investigation between wind shear and $\sigma$, the wind profiles have been normalized to 1 at 100 m asl in Fig. 5.16. The results show no clear relation between wind shear and $\sigma$. For $\sigma$ higher than 22.5 (very unstable conditions), the normalized profile shows an extreme wind shear. This classification gives a very high percentage of stable conditions around 85 % and a very low percentage of unstable and neutral conditions of ca. 5 % and 10 %, respectively. The overestimation of stable conditions maybe occurs

because this method is based on onshore data. For this reason, the thresholds should be adjusted for offshore conditions e.g. by a future measurement campaing.

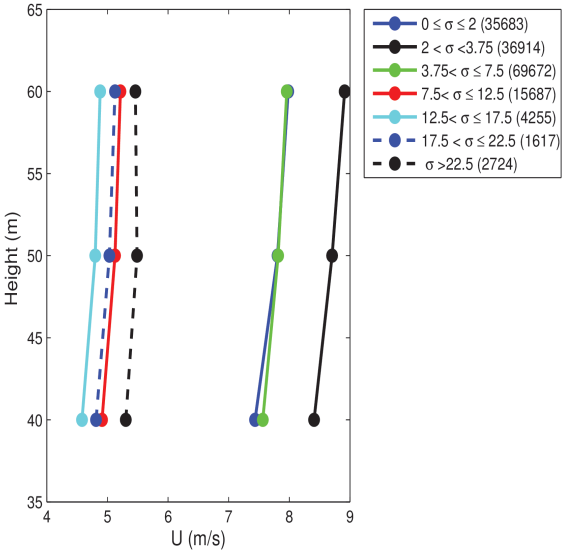


FIGURE 5.15: Average wind profiles for different classes of $\sigma$. The number of profiles for each class is given in parentheses.

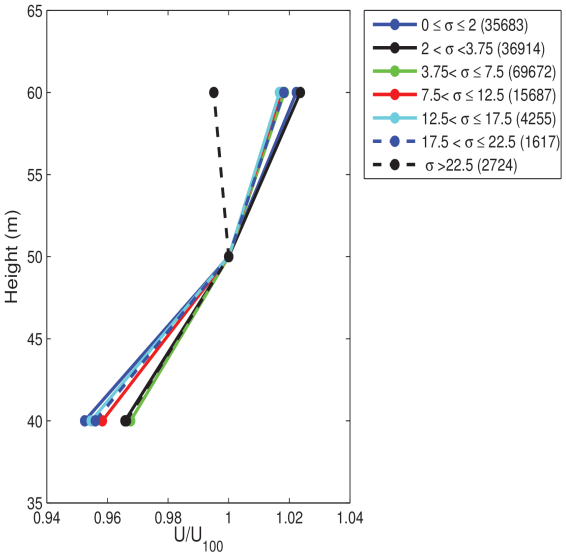


FIGURE 5.16: Normalized wind profiles for different classes of $\sigma$. The number of profiles for each class is given in parentheses.

# Chapter 6

# The Potential of Combination Lidar Wind Profiles with Satellite Data

In this chapter, case studies of different meteorological phenomena such as gravity waves, coastal jets and atmospheric fronts are presented and investigated using SAR, lidar and met mast data. The investigation of these mesoscale phenomena could be relevant for wind energy applications since they are connected to high turbulence and wind shear which have a negative impact on wind turbines.

## 6.1 Lee Waves

In atmospheric sciences, lee waves are quasi stationary atmospheric internal gravity waves. The lee waves are generated when the air flow blows over a mountain range with a stable air underlying over an unstable layer [41]. They usually are visible through different cloud formations such as lenticular clouds at high altitudes and rotor clouds at low levels (Fig. 6.1). In addition, lee waves with large amplitude can produce very strong downslope winds [42]. They have an important role in aviation since they can produce high turbulence (rotors) and strong wind shears, effects that also will have negative impacts on wind turbines when occuring close to the ground.

In this section, we will investigate an event of lee waves in the Havsul region with a combination of SAR and lidar wind profiler data. The wind profile measurements are essential for this investigation since the SAR can provide only information about the surface wind speed.

The SAR image in Fig. 6.8 shows the $\sigma$ parameter in dB which is proportional to the surface roughness. The dark (low $\sigma$) and bright (high $\sigma$) patterns along the coast represent trapped lee waves which are triggered by the mountain ranges at the west coast of Norway close to the Havsul region. For a better illustration of this atmospheric phenomenon, the SAR image ( Fig. 6.8) was analyzed to extract the surface wind speed using the CMOD algorithm and the wind direction from the HIRLAM (High Resolution Local Area Modelling) model in Fig. 6.3. The south/southwest wind direction and the clear separation of high (12-14 m/s) and low (6-8 m/s) wind speed patterns in the lee of the mountains, are the evidences of lee waves in the surface wind field off the coast.

For a further analysis of lee waves in the Havsul region, the wind transect between A and B location across the wave pattern is plotted in Fig. 6.4. This analysis shows again the variation of wind speed along the coast due to lee waves. The wavelength of lee waves is

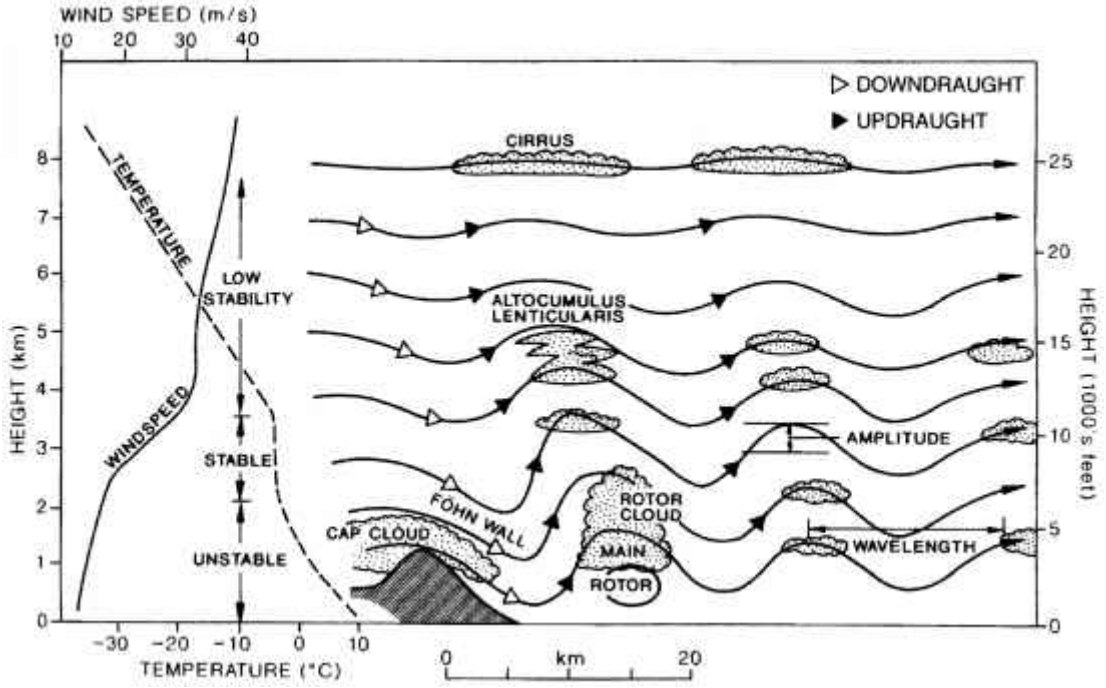


FIGURE 6.1: Lee waves and rotors are triggered by flow across a mountain. After Ernst [43].

ca. 20 km and the corresponding amplitude of surface wind speed is typically ± 2 m/s around the mean. The island of Storholmen is located approximately 40 km northwest from location A, at the 4th minimum of wind speed in the wind transect analysis (Fig. 6.4(bottom)).

The lidar wind profile data are used to validate the wind transect analysis and to investigate the wind speed and wind shear at Storholmen during this event. A problem for this analysis was the unavailability of lidar data, when the SAR image was taken at 21:08 UTC (24 April 2009). For this reason, only available lidar profiles are plotted between 23:10 UTC (24 April 2009) and 01:20 UTC (25 April 2009) in Fig. 6.5 and Fig. 6.6. Due to the persistency (ca. 6-12 hours) of lee wave episodes, these lidar wind profiles can be assumed representative to describe this atmospheric phenomenon.

Fig. 6.5 presents the available offshore wind profiles at Storholmen during the event. It shows a periodic back and forth movement of the U profiles which is related to the spatial and time variation of lee waves. Furthermore, there is a strong wind shear for U profiles between 23:10 and 00:40. Close to the sea surface (60 m asl), low wind speeds (7-8 m/s) are observed by the lidar which can validate the estimation of SAR wind speed at 6 m/s at the sea surface (Fig. 6.4). On the other hand, for high levels (200 m asl)

the wind speed reaches 10 to 12 m/s, generating a wind shear of 3-4 m/s over 140 m asl. These results are typical for situations with lee or shear waves [33].

Fig. 6.6 shows the corresponding available offshore w profiles. There is a high negative w (downward) with a range of -0.9 to -0.5 m/s which decreases with height at -0.4 to -0.2 m/s at 200 m asl. The result indicates the presence of downslope winds in the descending part of lee waves (Fig. 6.1). The high values of w close to the ground could be explained as a potential effect of flow distortion since the downslope wind increases approaching the island. In addition, a possible violation of the horizontal homogeneity assumption (section 3.1.7.2) of the lidar cone angle close to ground due to high turbulence (i.e.rotors) during this event, can effect the accuracy of the lidar measurements.

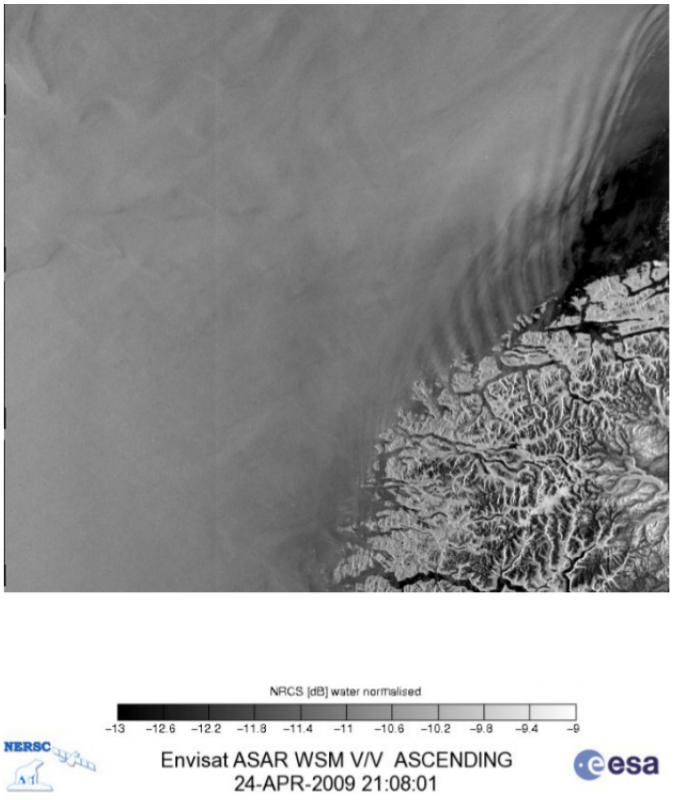


FIGURE 6.2: SAR (ENVISAT ASAR Wideswath) image of the west coast of Norway obtained on 24 April 2009.

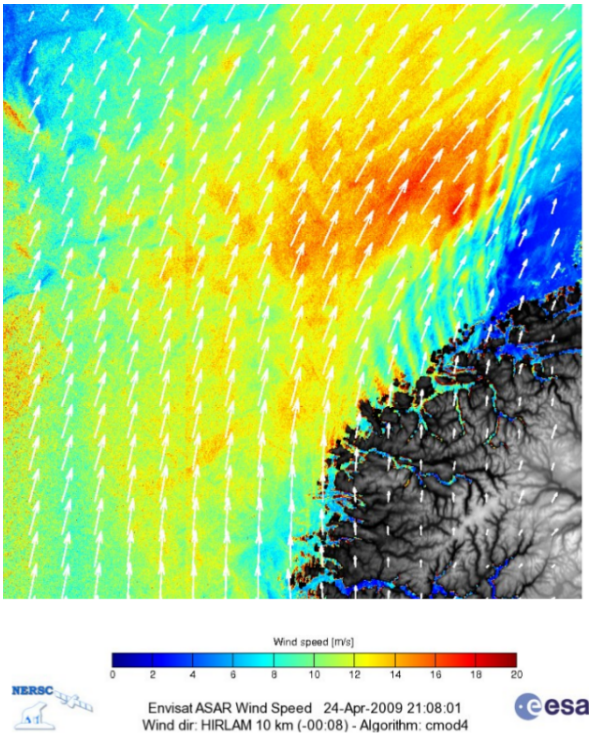


FIGURE 6.3: Analysis of SAR (ENVISAT ASAR Wideswath) image of the west coast of Norway obtained on 24 April 2009. Wind speed was estimated by CMOD algorithm and wind direction by HIRLAM model.

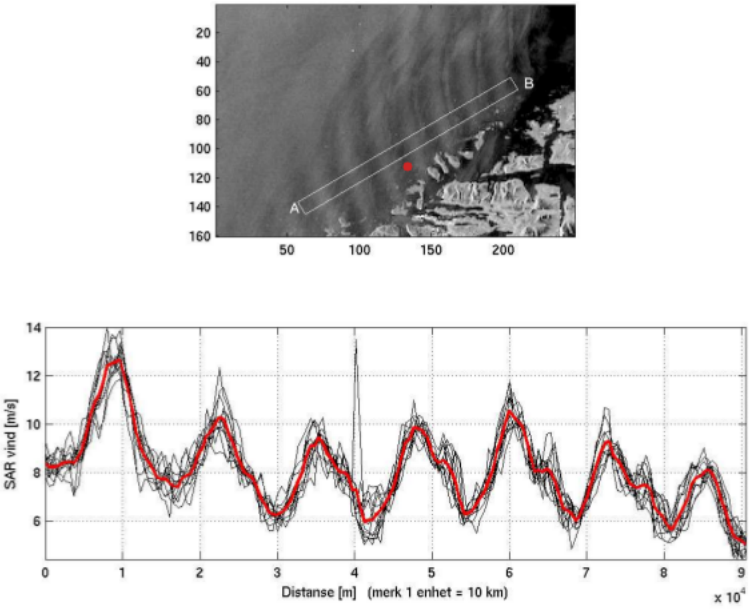


FIGURE 6.4: Wind Transect between A and B location. Adapted by[33]. Location of Storholmen is illustrated with a red dot.

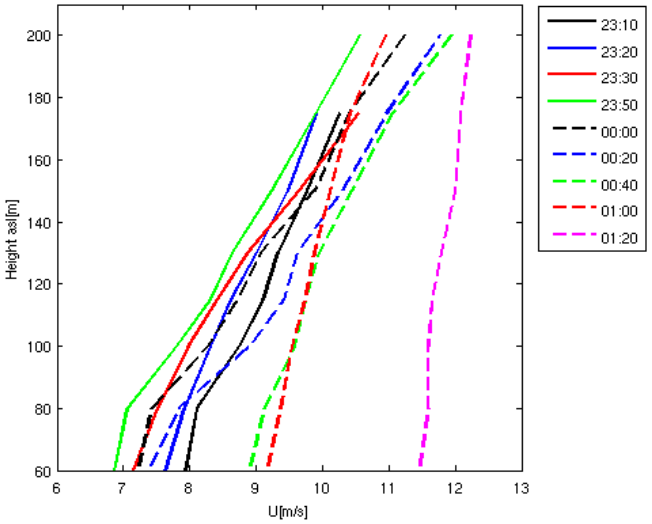


FIGURE 6.5: Available offshore wind profiles, 24-25 April 2009.

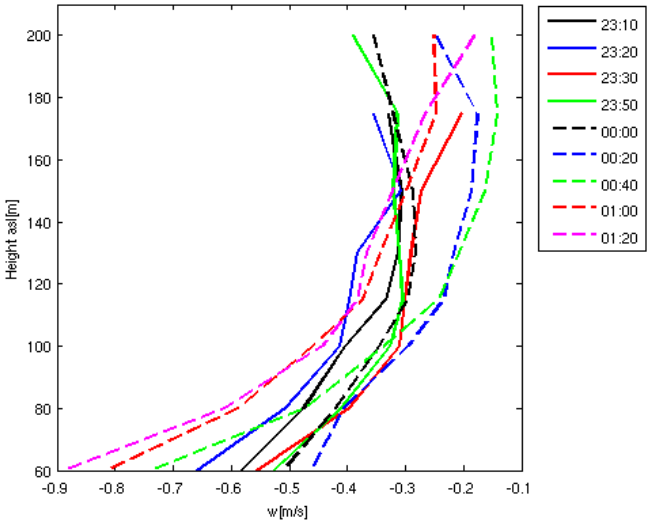


FIGURE 6.6: Available offshore w profiles, 24-25 April 2009.

## 6.2 Low level coastal jets

In this section, the blocking of winds by terrain in the Havsul region is investigated. When an air flow is approaching an obstacle (i.e. a mountain range) it can either go over or around it. This depends on the height and width of the obstacle, and the speed of the air flow and the atmospheric stability [44].

Low-level coastal jets are induced by blocking of winds by the terrain. A well-mixed, cool and moist marine atmospheric boundary layer which is capped by an inversion is the essential atmospheric condition that can develop a low level coastal jet [45]. As it is illustrated in Fig. 6.7, the inversion slope exceeds downward to reach the coast where temperature and sea level pressure gradient reach the highest values. As a result of the maximum of sea level pressure gradient close to the coast, the low level wind speeds increase and lead to a low level coastal jet. The presence of coastal mountains can keep the air flow parallel to the coastline and decrease the effect of the potential sea breeze [45]. The width of the jet has a typical range between 20 to 40 km. The observed winds are often higher than 18 m/s or 35 knots [45]. These strong winds lead to a high wind shear and can induce high waves which can effect the offshore structures. Numerical simulations of these mesoscale phenomena over southern Norway have also been studied by Barstad and Gornas [46].

The SAR image 20.03.2011 (Fig. 6.7) the central west Norwegian coast was analyzed in Fig. 6.8 to estimate the surface wind speed (CMOD algorithm) and wind direction (HIRLAM). The analysis shows clearly the presence of the low level jet with high wind speeds from 14 to 20 m/s close to the coast and a width of about 30-40 km. Due to separation of the flow, there is a sharp boundary of few kilometers which separate the high (14-20 m/s) from the low (8-10 m/s) wind flow. This separation produces a high horizontal wind shear which can be dangerous for the potential offshore applications in this area.

Close to the coast, the results of high surface wind speed by SAR agree well with the wind measurements at Ona in Fig. 6.10 since the observed wind speed ranges between 14 m/s and 22 m/s at 60 m asl during this event. In addition, the vertical wind shear is relatively low with the maximum value of 1.5 m/s over 20 m. Fig. 6.11 shows the horizontal turbulence intensity during the event of low level coastal jet. The $I_U$ has a

range of $5\% - 12\%$, with a mean value around 7%. These results indicate that the air flow of the coastal jet is steady with high wind speeds, relatively low wind shear and small fluctuations of the wind field.

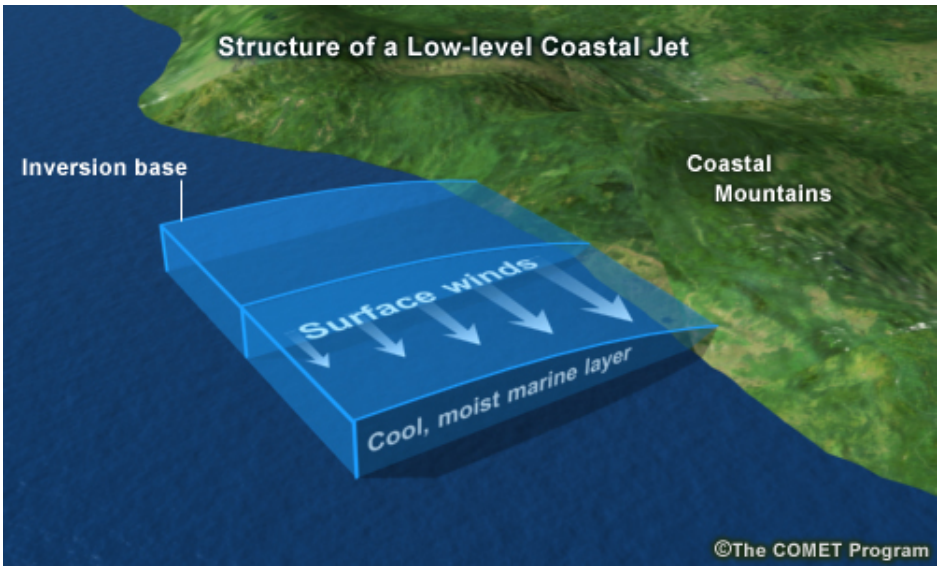


FIGURE 6.7: Structure of low level coastal jet in MABL [45].


FIGURE 6.8: SAR (ENVISAT ASAR Wideswath) image of the west coast of Norway obtained on 20 March 2011.

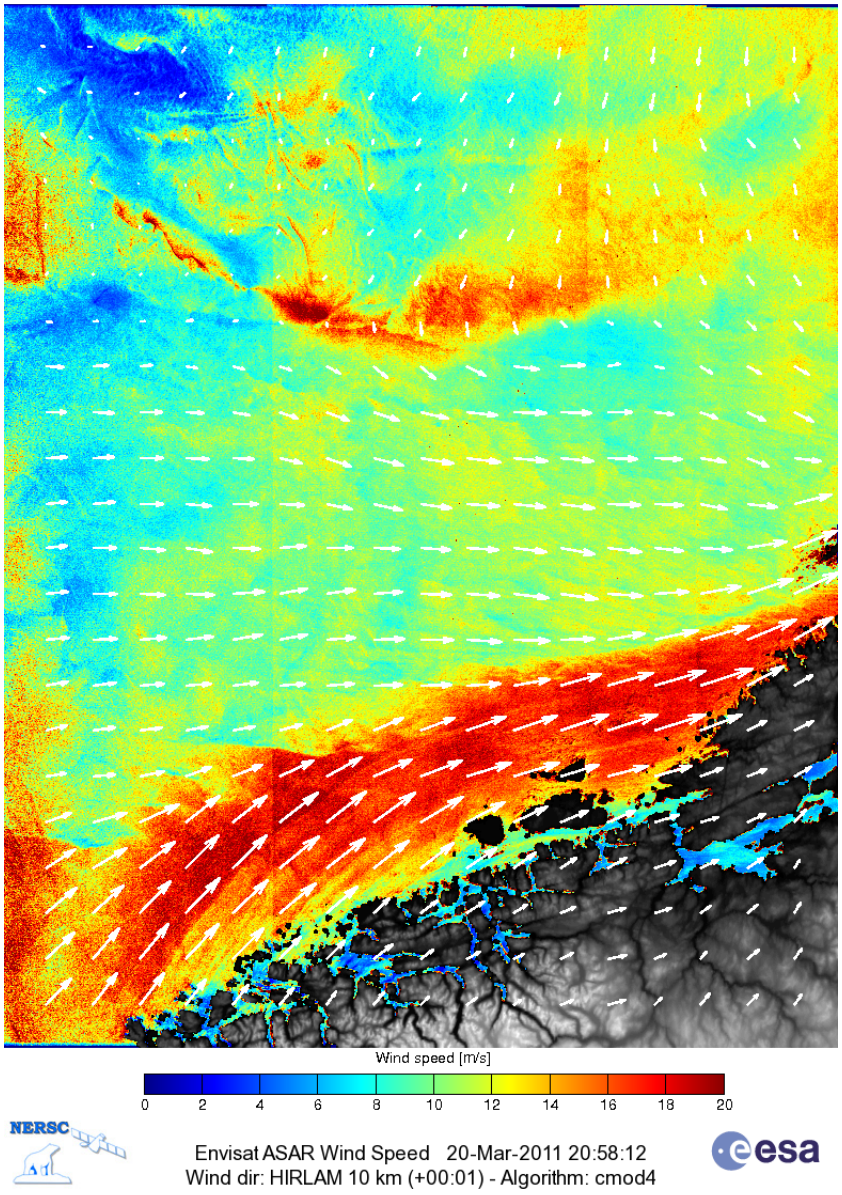


FIGURE 6.9: Analysis of SAR (ENVISAT ASAR Wideswath) image of the west coast of Norway obtained on 20 March 2011. Wind speed was estimated by CMOD algorithm and wind direction by HIRLAM model.

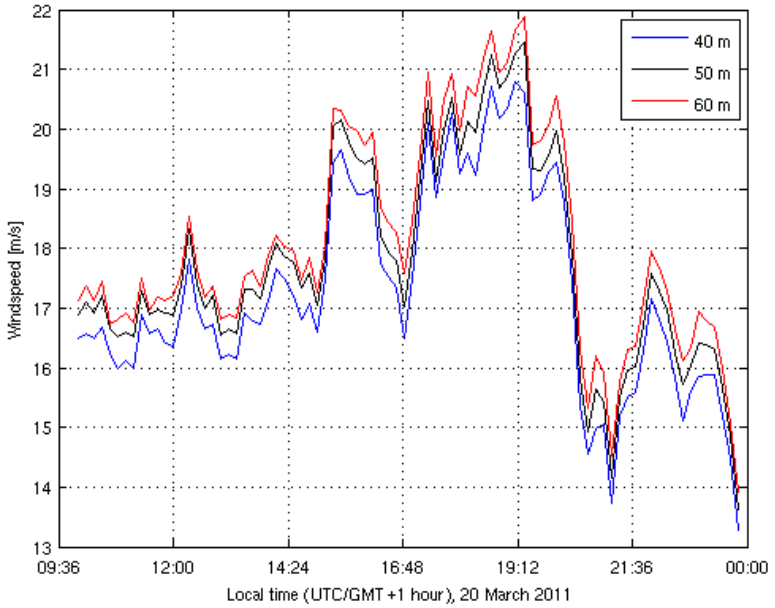


FIGURE 6.10: Time series of U at Ona, 20 March 2011.

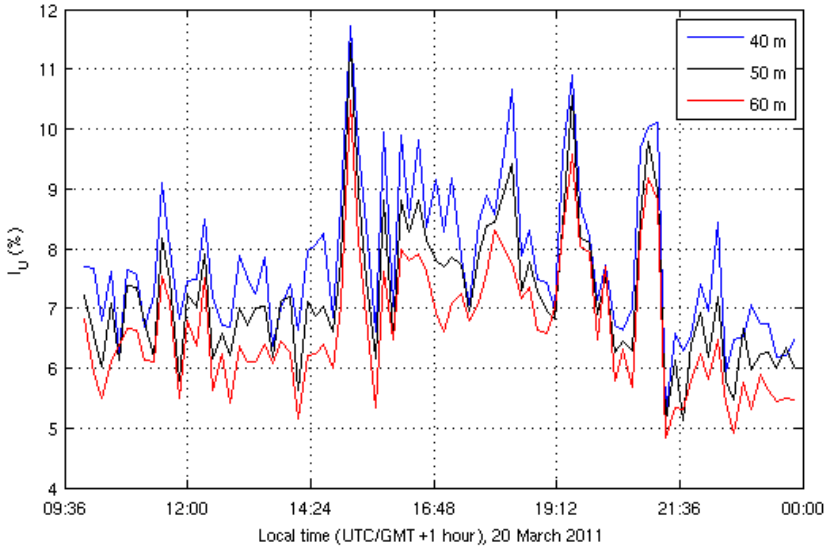


FIGURE 6.11: Time series of $I_U$ at Ona, 20 March 2011.

## 6.3 Atmospheric front

An atmospheric front is a boundary which separates two air masses of different densities, humidities and temperatures. There are two main types of front, the cold and warm front. The cold front is defined as the density discontinuity of a cooler air mass, replacing a warmer air mass. The Warm front is the boundary where a warm air mass is replacing a cold air mass. The passing of an atmospheric front over an area is indicated by changes in atmospheric pressure, temperature, wind speed and direction and often accompanied by precipitation.

The SAR image of Fig. 6.12 shows a developed atmospheric front which is passing over the central west coast of Norway on 22.05.2011. The SAR image was analyzed in Fig. 6.14 for the estimation of surface wind speed (CMOD algorithm) and wind direction (HIRLAM). In addition to SAR data, a hindcast of 10 m wind speed and mean sea level pressure at the south west Norway at 21 UTC 22 May 2011 is plotted using Diana (meteorological visualization program from the Norwegian Meteorological Institute) in Fig. 6.16. It shows the presence of a low pressure system (988 hPa) north of Lerwick island. For this analysis, the front is marked as a narrow area of few kilometers with high wind speeds (ca 16-20 m/s). After the passing of the front, the surface wind direction changes sharply from west to southeast.

For a better investigation of this phenomenon, the wind direction and temperature at Ona are plotted in Fig. 6.15. It shows a simultaneous sharp drop in temperature from $16°C$ to $10°C$ and an abrupt change in wind direction from southeast (100°) to west (270°) at around 17 local time. These indications proved the passing of cold front over the area. In addition, a short burst of high wind speed from 6 to 13 m/s is observed at the same time in Fig. 6.14. This strong gust of wind speed due to the passing of the cold front may have a negative effect on offshore wind turbines.

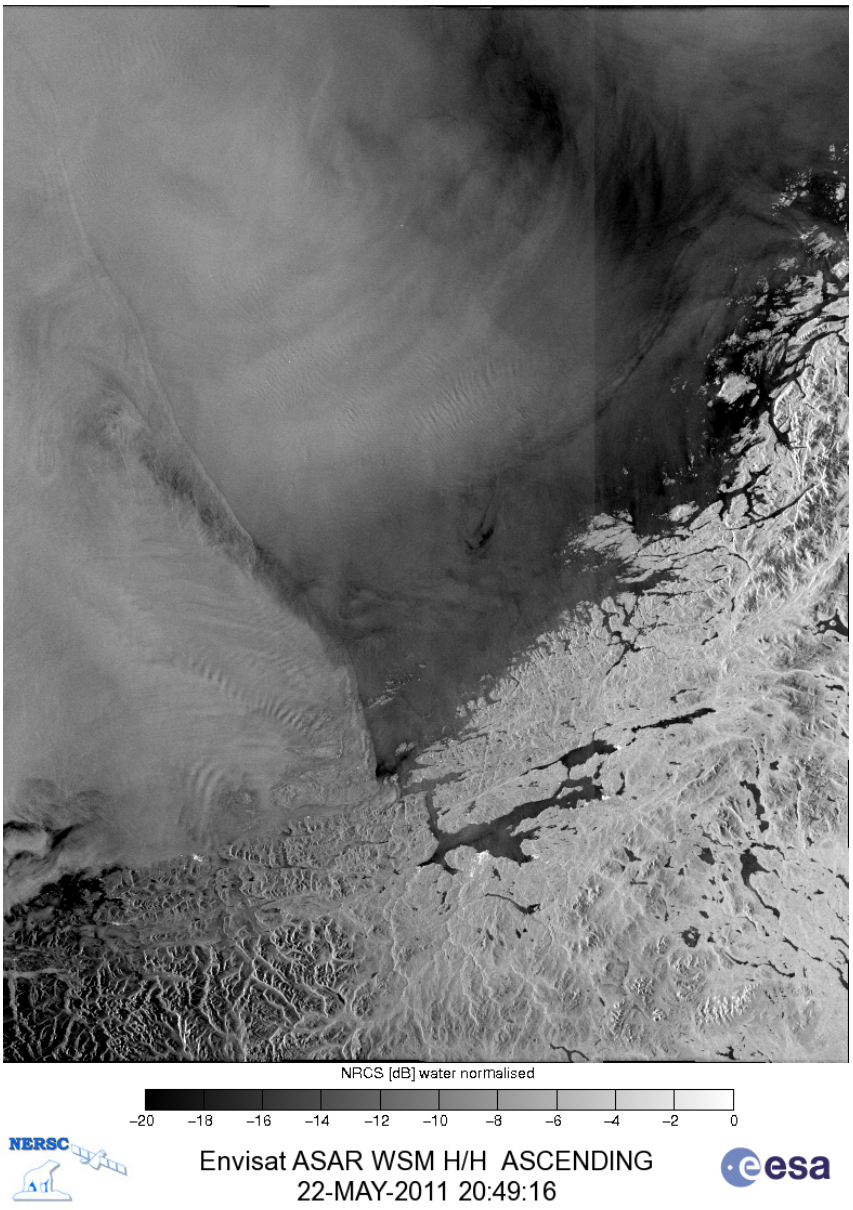


FIGURE 6.12: SAR (ENVISAT ASAR Wideswath) image of the west coast of Norway obtained on 22 May 2011

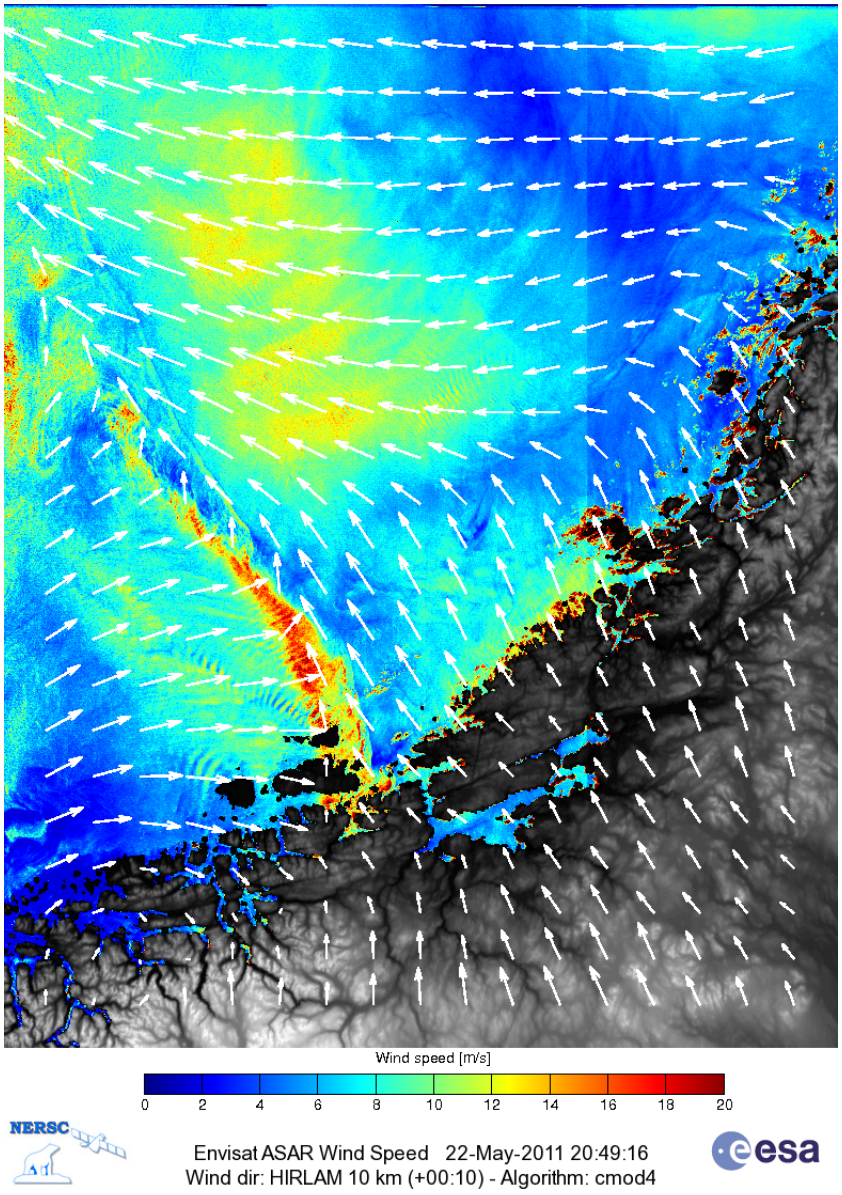


FIGURE 6.13: Analysis of SAR (ENVISAT ASAR Wideswath) image of the west coast of Norway obtained on 22 May 2011. Wind speed was estimated by CMOD algorithm and wind direction by HIRLAM model.

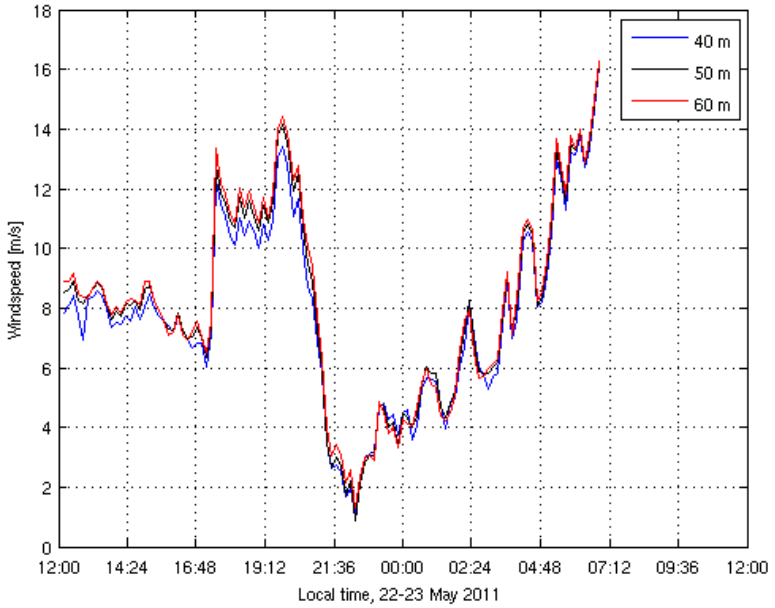


FIGURE 6.14: Time series of wind speed at 22-23 May 2011

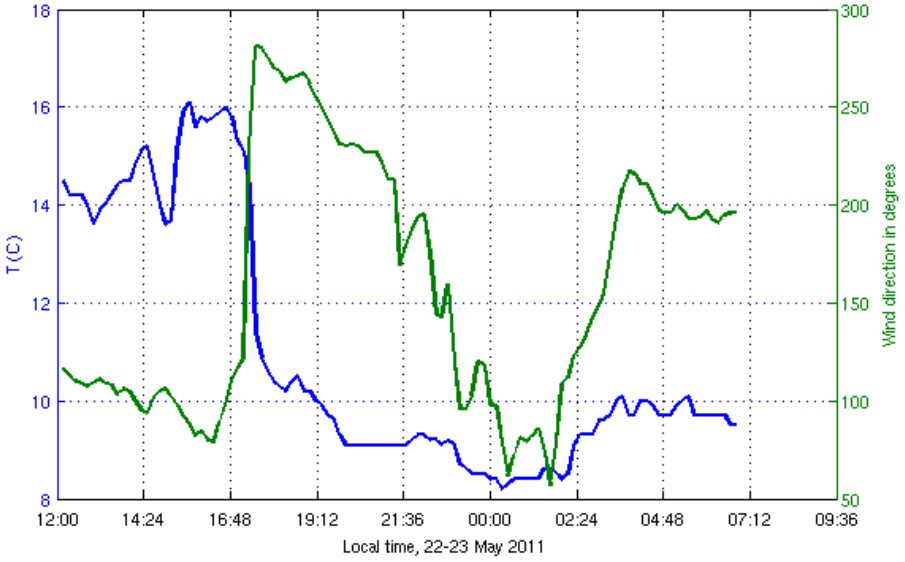


FIGURE 6.15: Time series of Temperature and wind direction at 22-23 May 2011.

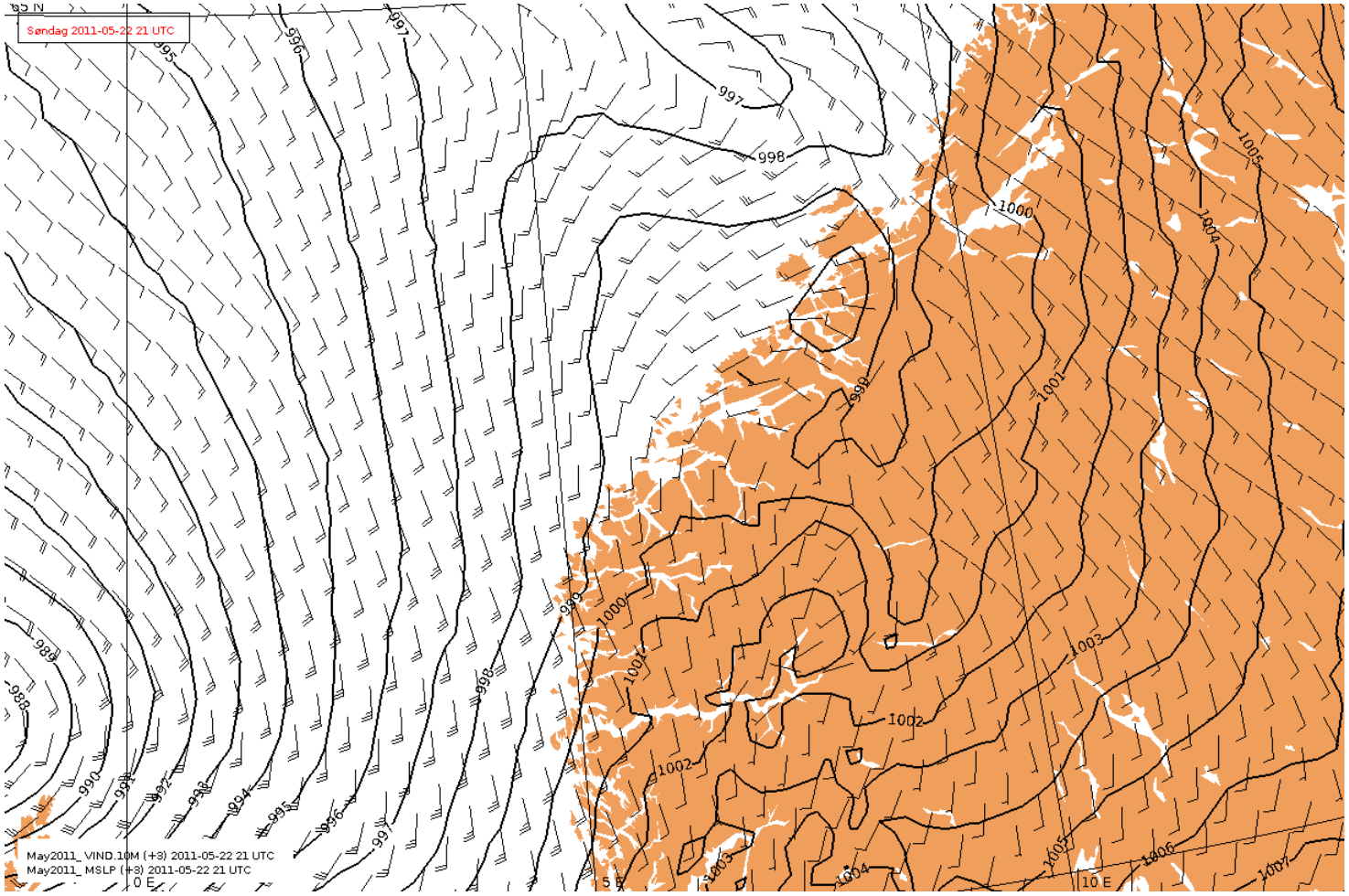


FIGURE 6.16: Hindcast of 10m wind speed and mean sea level pressure at the south west Norway, 22 May 2011, 21.00 UTC. Provided by Birgitte R. Furevik

# Chapter 7

# Conclusions and outlook

## 7.1 Summary

The study presented an analysis of lidar wind profile data for a better characterization of MABL with respect to wind energy applications. Lidar can provide a rich of source data for an improved understanding of offshore wind field and turbulence conditions.

Based on our statistical analysis, the prevailing wind blows from the southwest in the Havsul region. However, during summer months, the wind direction changes to north-east due to the see breeze combined with terrain driven circulations occurs along the Norwegian coast [47]. For the analysis of wind distributions, the Weibull and Nakagami distributions represent best description of the offshore horizontal wind speed. For the vertical wind speed, the t-locational scale gives the best results. The statistical analysis of $I_U$ shows a clear dependency of the turbulence intensity distribution on the wind speed. For increasing wind speed the center of the distribution moves to lower turbulence intensities and the probability density increases. The investigation of TKE gives the result that occurrence of high TKE is higher for offshore conditions. In addition, the results present that the TKE and $I_U$ are typically correlated. For increasing the wind speed, their relationship becomes more quadratic. On the other hand, TKE and $I_w$ are uncorrelated. Finally, a clear dependency between TKE and $\alpha$ for increasing wind speed is presented.

Our investigation of offshore wind profiles shows that the turbulence parameters, i.e. $I_U$, $I_w$, TKE, are strongly connected to the average offshore wind profiles and wind shear. The result indicates that the general idea of the classification of atmospheric stability without temperature measurement as described for SODAR onshore data by Wharton and Lundquist [6] should be possible to adapt for offshore lidar measurements. Due to a close relation between $I_U$ and wind shear on the normalized offshore profiles, $I_U$ seems more promising to classify the atmospheric stability for offshore conditions. The method of standard deviation of the horizontal wind direction was applied as another proxy of atmospheric stability. The results show that the thresholds of this method should be potentially adjusted on offshore conditions. Possible effects of flow distortion from the island were discussed using the w component of wind speed for the classification of wind profiles.

Finally, case studies of different meteorological phenomena are investigated using a combination of SAR, lidar and met mast data. The results show that this combination of instruments can be applied for a better understanding of these phenomena and their potential effects on offshore wind energy applications.

## 7.2 Future Research

**Lidar and MTP campaign**

The need for simultaneous measurements of temperature gradient and turbulence parameters is crucial of importance for the classification of atmospheric stability. In particular, the stability methods that have been described in sections 2.4.4 and 2.4.5 need calibration of thresholds for offshore conditions. For this reason, combination of lidar and temperature profilers such as the Microwave Temperature Profiler Attex MTP-5 could be an idea for future measurement offshore campaigns.

**Investigation of Wind and Turbulence with respect to Wind Direction**

For an improved understanding of the different effects of land and ocean on the wind field, an analysis of the turbulence parameters, the wind shear and the wind profiles could be performed separately for different wind direction sectors.

**Lidar and CFD simulations**

For a further investigation of the effect of flow distortion on the lidar measurements due to the island, CFD simulations could be an appropriate tool.

**Lidar and WRF model**

The relation between the offshore wind profiles and the turbulence parameters i.e. $I_U$, $I_w$ and $TKE$, which is described in Chapter 5, can be also studied by the WRF model.

**Lidar and SAR data**

The missing information of wind profiles and wind shear from SAR data can be provided by lidar or met mast measurements. This combination of different measurement techniques could be potentially applied for the further investigation of different atmospheric phenomena and of their impact on offshore wind turbines.

# Appendix A

# Poster

# Characterization of marine atmospheric boundary layer using LIDAR data

Konstantinos Christakos, Geophysical Institute (GFI), University of Bergen (UiB), *Konstantinos.Christakos@student.uib.no*
Master thesis at GFI: Supervisor: Joachim Reuder (GFI, UiB). Co-supervisor: Birgitte R. Furevik (GFI, UiB & met.no)

norcowe Norwegian Centre for Offshore Wind Energy

## Introduction

The main task of this study is the processing and interpretation of the 10 minute average wind speeds from the LIDAR measurements on the small island of Storholmen (Fig.2). The LIDAR data includes measurements at 60 m, 80 m, 100 m, 115 m, 130 m, 150 m, 175 m and 200 m above the sea level (asl) for the period 1.2008 - 1.2012.

**Figure 1**. The WindCube LIDAR (Light Detection And Ranging) device at Storholmen. The photo is provided by Vestavind Offshore.

**Figure 2**. Storholmen (square) is located northwest of the island of Vigra.

## Wind rose

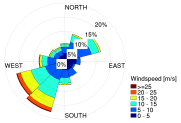


**Figure 3**. Wind rose, period 2008-12,height: 100m asl.

Winters[DJF] (2008-12)

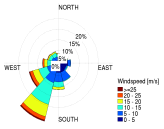

Springs[MAM] (2008-11)

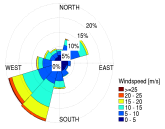

Summers[JJA] (2008-11)

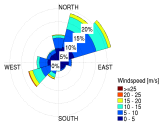

Autumns[SON] (2008-11)

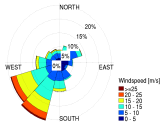

**Figure 4**. Seasonal Wind roses at Storholmen, height: 100m asl.

## Weibull distribution

The Weibull(2-Parameter) distribution is the most widely accepted distribution for wind speed. The Weibull probability density function is given by equation 1:

$$f(u) = \frac{k}{c}\left(\frac{u}{c}\right)^{k-1} \exp\left[-\left(\frac{u}{c}\right)^{k}\right] \quad \text{[Eq.1]}$$

where u is the wind speed, k is the shape parameter(dimensionless) and c is the scale parameter(m/s). The monthly probability density function and the monthly cumulative frequency function calculated from the measured wind speed at 100m asl at Storholmen for the period 2008-12 are shown in Fig. 5. In addition, the monthly variation of Weibull parameters and mean wind speed are illustrated in Fig.6 and Fig.7, respectively.

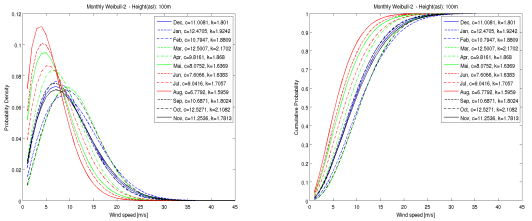

**Figure 5**. The monthly Weibull probability density function(left) and the monthly cumulative frequency function(right) at 100m asl at Storholmen, period 2008-12.

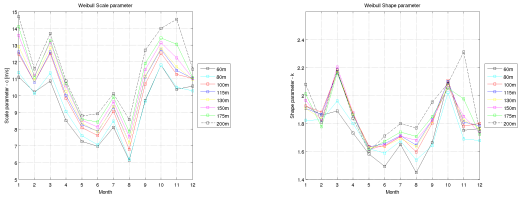

**Figure 6**. Monthly variation of Weibull Scale (left) and Weibull Shape (right) parameters at 100 m asl, Storholmen, period 2008-12.

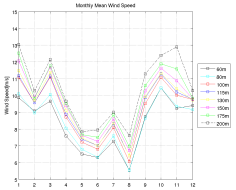

**Figure 7.** Monthly variation of mean wind speed at 100m asl, Storholmen, period 2008-12.

## Turbulence Intensity

Turbulence intensity ($I$,%) includes direct measurements of horizontal turbulence fluctuations. LIDAR estimates of turbulence intensity is calculated by equation 2:

$$I = \frac{\sigma}{u} \quad \text{[Eq.2]}$$

where u is the horizontal wind speed and σ represents the standard deviation of u.
The Log-normal distribution is applied to describe the turbulence intensity distribution for different levels of wind speed (Fig.8). For higher values of wind speed,the turbulence intensity distribution is narrower and its center closer to zero.

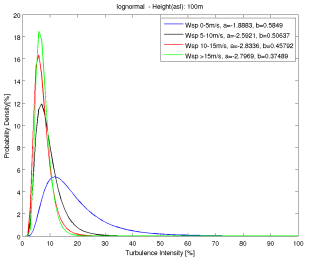

**Figure 8.** Log-normal distribution of turbulence intensity for different levels of wind speed

## Atmospheric stability

The atmospheric stability affects profiles of mean wind speed,direction, turbulence and impacts on power generation [1].
In this study, the atmospheric stability is calculated using the horizontal turbulence intensity due to lack of temperature (vertical gradient) measurements.
The stability classification scheme used for this study is based on Wharton and Lundquist [1] as follows:

- Strongly Stable: *I<8%*
- Stable: *8%<I<10%*
- Near-neutral: *10%<I<13%*
- Convective: *13%<I<20%*
- Strongly convective: *I>20%*

The monthly stability analysis of LIDAR data using this classification is shown in Fig. 9.
Since this classification is based on onshore measurements, the thresholds have potentially to be adapted to offshore conditions.

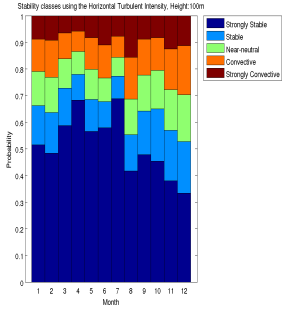

**Figure 9.** Monthly stability analysis of LIDAR data using the stability classification based on the horizontal turbulent intensity

## References

1. Wharton S and Lundquist J K (2012)Atmospheric stability affects wind turbine power collection,Environ. Res. Lett. 7

## Acknowledgements

The LIDAR data and the photo(Fig.1) have been provided by Vestavind Offshore.

Vestavind OFFSHORE

FIGURE A.1: Poster in NORCOWE days: "Offshore Wind Farms - Measurements and Control", 19 September 2012, Bergen, Norway.

# Appendix B

# Paper

Available online at www.sciencedirect.com

SciVerse ScienceDirect

Energy Procedia 00 (2013) 000–000

Energy Procedia

www.elsevier.com/locate/procedia

10th Deep Sea Offshore Wind R&D Conference, DeepWind'2013

# Experimental characterization of the marine atmospheric boundary layer in the Havsul area, Norway

Konstantinos Christakos[a,*], Joachim Reuder[a], Birgitte R. Furevik[a,b]

[a]*Geophysical Institute, University of Bergen, Allegaten 70, 5020 Bergen, Norway*
[b]*Norwegian Meteorological Institute, Allegaten 70, 5020 Bergen, Norway*

**Abstract**

Offshore wind energy applications depend strongly on an improved knowledge of the physical processes taking place in marine atmospheric boundary layer (MABL). In particular the better understanding of the complex interactions between wind shear, atmospheric stability and turbulence and the effects of wind-wave interactions on offshore vertical wind profiles are essential for the development of offshore wind projects. This paper presents an analysis of the relation between turbulence parameters, such as horizontal and vertical turbulence intensity, and turbulence kinetic energy and average vertical wind profiles and wind shear. The investigations are based on 4 years of wind lidar measurements on the small island of Storholmen in the Havsul area about 8 km off the coast of the Norwegian mainland. The results show systematic dependencies between the investigated turbulence parameters, both with respect to average wind speeds and average wind shear. The results indicate that in particular the horizontal turbulence intensity has the potential to act as a proxy for atmospheric stability in cases where corresponding temperature profiles are not available.



*Keywords:* Marine Atmospheric Boundary Layer; Turbulence Intensity; Turbulence Kinetic Energy; Wind Speed;

## 1. Introduction

The offshore wind power production has grown rapidly over the last two decades. In 1991, the first offshore wind farm was inaugurated for a total capacity of 4.95 MW, 2.5 km off the Danish coast at Vindeby [1]. By the end of 2011, 1662 turbines installed and grid connected 4.995 MW in 55 wind farms spread across Europe [2]. A better understanding of the physical processes in the marine atmospheric boundary layer (MABL) becomes critical important for the development of offshore wind farms. Measurements of the offshore wind field are of essential relevance for the characterization of the MABL. However the main problem is the lack of observational data in the relevant altitude range. For this reason meteorological remote sensing instruments are used in this field, such as LIDAR (LIght Detection And Ranging) and

*corresponding author: Konstantinos Christakos
*E-mail address:* Konstantinos.Christakos@student.uib.no.

SODAR (SOnic Detection And Ranging). The lidar is an active remote sensing instrument which relies on the the measurement of Doppler shift of laser radiations backscattered by particles in the air [3].

Lidar systems can take simultaneous measurements of the wind velocity up to several hundred meters, a region hardly accessible by meteorological masts. In addition they are more flexible with respect to positioning and handling. This remote sensing technique has progressed significantly during the last years and is on its way of being widely accepted as essential part of wind resource analysis and related scientific investigations of the MABL.

On the other hand atmospheric conditions can limit the data availability of lidar systems. The availability is in general dependent on the carrier to noise ratio (CNR) of the reflected lidar signal, mainly influenced by the distance from the light source and the amount of aerosol particles in the scattering volume. Reliable wind profile measurements require a minimum value of the CNR, measurements below this threshold are omitted from the data set. Other atmospheric parameters, as atmospheric turbulence and relative humidity also can affect the CNR [4]. In case of precipitation, the vertical velocity measured by the lidar is in addition biased by the fall velocity of the rain droplets [4].

During the last years, many studies are focused on the effect of atmospheric stability characteristics on the wind power generation. Rareshide et al. (2009) [5] studied the sensitivity of power curves to wind shear in the regions of the US Great Plains/Midwest region. They found that high positive wind shear is related to higher wind power than when wind shear was low. On the other hand, Wagner et al. (2009) [6], found that high wind shear decreased power output in comparison with no wind shear, based on wind turbines on flat terrain at Høvsøre in the northwest of Denmark. Kaiser et al. (2003) [7] suggested that measured wind power curves are influenced by the turbulence intensity. Unfortunately wind lidars, can not provide the required temperature structure of the atmosphere for direct stability analysis. However, Wharton and Lundquist (2012) [8], [9] recently presented a method to determine atmospheric stability from various turbulence related parameters, as horizontal and vertical turbulence intensity, turbulence kinetic energy, and wind shear, derived by a SODAR system. These measurements took place at a wind farm at the North American West Coast. The study presented here aims to transfer and investigate the applicability of the method based on SODAR measurements for an onshore boundary layer to offshore conditions, probed by a lidar system. It examines the relationship between the corresponding turbulence parameters, including horizontal turbulence intensity ($I_U$), vertical turbulence intensity ($I_w$) and turbulence kinetic energy (TKE) on average wind speed and average wind shear.

## 2. Data and Methods

### 2.1. Data Overview

Wind profile data were collected from January 2008 to January 2012 at the small island of Storholmen in the Havsul area (Fig. 1), located about 8 km northwest of the island of Vigra on the West coast of Norway. The measurements were taken with a lidar wind profiler (WindCube v.1 by Leosphere) deployed at 20 m above sea level (asl). Wind speed and wind direction was measured at eight height levels between 60 m and 200 m asl. The basic sampling rate of the instrument was set to 1 Hz, providing independent wind profiles every 4 seconds. The investigations are based on 10 minute average wind profiles and wind speed variances over this time period. Due to the processes discussed above in the introduction, the data availability of the lidar system decreases with the height in the atmosphere. While the lowest level of 60 m asl reaches an average data availability of 76.82%, this value is reduced to 75.87% at 100 m asl and 42.54% at 200 m asl. For the further analysis, only data sets of complete profiles between 60 m and 150 m asl have been used, leaving a total of 75249 profiles for this investigation.

### 2.2. Theory

The horizontal turbulence intensity ($I_U$, %) is a dimensionless parameter which measures the turbulence fluctuations in the wind field. Mathematically it is defined as the standard deviation of horizontal

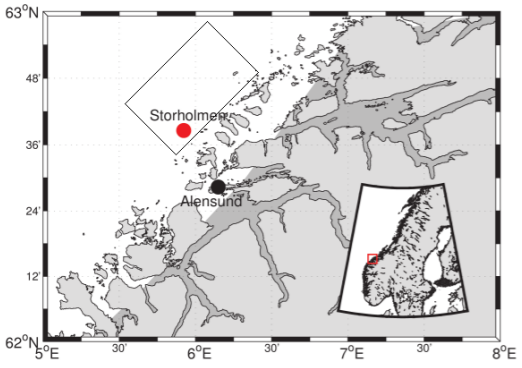


Fig. 1: Location of Storholmen island (red dot) in Havsul (selected area) off the coast of Alesund, Western Norway.

velocity fluctuation divided by the mean horizontal wind speed (U in m/s), in this study taken at a reference height of 100 m asl:

$$I_U = \frac{\sqrt{\sigma_u^2 + \sigma_v^2}}{U} \tag{1}$$

The horizontal wind speed U is calculated form latitudinal and longitudinal velocity components measured by the LIDAR as $U = \sqrt{u^2 + v^2}$. The vertical turbulence intensity ($I_w$, %) can be calculated correspondingly based on the standard deviation in the vertical velocity:

$$I_w = \frac{\sigma_w}{U} \tag{2}$$

Finally, the turbulence kinetic energy (TKE, $m^2/s^2$) is an important variable in boundary layer meteorology because it is a direct measure of the three dimensional turbulence. TKE is defined as the sum of the velocity variances in latitudinal (u), longitudinal (v) and vertical (w) direction divided by 2.

$$TKE = \frac{1}{2}(\sigma_u^2 + \sigma_v^2 + \sigma_w^2) \tag{3}$$

## 3. Results

### 3.1. Horizontal Turbulence Intensity

According to previous studies of offshore wind, e.g. [10] , a log-normal distribution has been applied to describe the turbulence intensity distribution. Fig. 2 presents the resulting distributions of turbulence intensity for different classes of wind speed at 100 m asl. The height of 100 m asl is selected as typical level for the nacelle heights of state of art wind turbines. The distribution parameters were computed using the maximum likelihood estimates (MLEs).

The results show a distinct dependency of the probability density distributions on the wind speed. For increasing wind speed the distribution narrows while its center moves towards lower turbulence

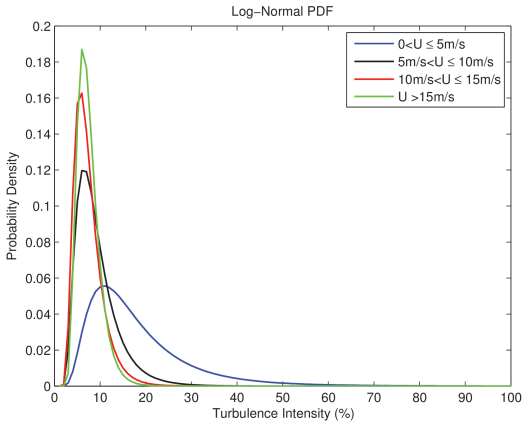


Fig. 2: Log-normal distribution of the horizontal turbulence intensity $I_U$ for different classes of wind speed at 100 m asl.

intensities. Simultaneously the peak value increases. In general there is a decrease of turbulence intensity for an increase in wind speed. However, for wind speeds greater than 10 m/s, the turbulence intensity remains nearly constant. Average vertical wind profiles for different horizontal turbulence intensity classes are presented in Fig.3 (left). For classification of the turbulence intensity the level 100 m asl has been selected. There is a clear dependency between turbulence intensity and average wind profiles. For turbulence intensities greater than 6% (51396 vertical wind profiles, corresponding to 68 % of the data), an increase of U is related to decrease of turbulence intensity. For turbulence intensities below 9% (46663 vertical wind profiles, 62% of the data) the average profiles are closely grouped between 10 m/s and 12 m/s. For an easier comparison of the dependency of wind shear on horizontal turbulence intensity, the profiles have been normalized to 1 at 100 m asl. The results (Fig. 3, right) show a general increase in wind shear for decreasing turbulence intensities. For $I_U \geq 20\%$ (6603 vertical wind profiles, corresponding to 8.77 % of the data) which is related to low wind speeds (ca. 2m/s), the profile shows a distinctly enhanced wind shear in particular at the highest levels. However this wind speed region is hardly of interest for offshore wind energy applications.

### *3.2. Vertical Turbulence Intensity*

The vertical turbulence intensity can also be used for the classification of atmospheric stability [8], [9]. Average vertical wind profiles for different vertical turbulence intensity classes at 100 m asl are presented in the left panel of Fig. 4. For a vertical turbulence intensity greater than 4 % (31333 vertical wind profiles, corresponding to 41.63 % of the data), the higher $I_w$ , the lower the wind speed. For turbulence intensities below 4 % (43916 vertical wind profiles corresponding to 58 % of the data) the average profiles are grouped again between 10 m/s and 12 m/s. In the right panel of Fig. 4 the vertical wind profiles are again normalized to 1 at 100 m asl. The results show that for levels below 100 m asl a decrease of the wind shear is related to an increase of $I_w$. For levels above 100 m asl there is a weaker dependency between wind shear and $I_w$ than closer to the ground.

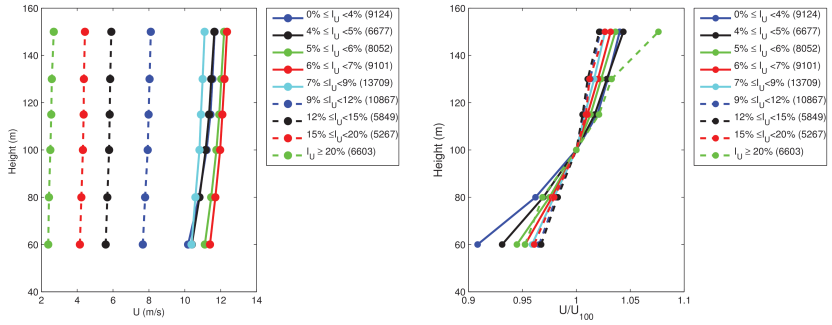


Fig. 3: Average vertical wind profiles for different classes of $I_U$ at 100 m asl (left) and the corresponding normalized profiles right). The number of profiles for each class is given in parenthesis.

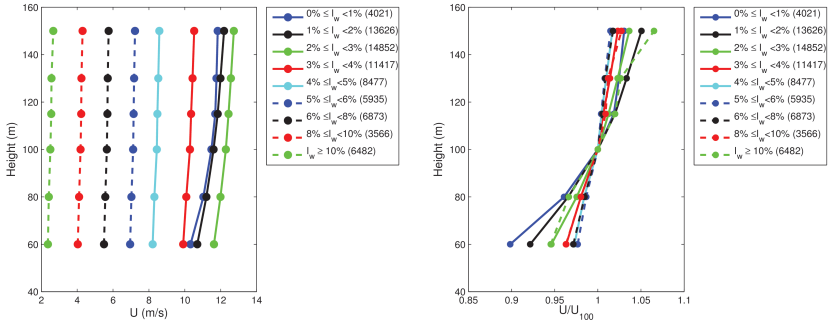


Fig. 4: Average wind profiles for different classes of $I_w$ at 100 m asl (left) and the corresponding normalized profiles (right). The number of profiles for each class is given in parenthesis.

### *3.3. Turbulence Kinetic Energy*

TKE is a measure for the energy content related to the 3-dimensional eddy motions in turbulent flow and is also indirectly related to the ability of transporting heat, moisture, and momentum through the boundary layer. TKE can be produced both by buoyancy and wind shear. Buoyancy production is related to thermally induced convection, while the shear production term of TKE represents the interaction of the turbulent momentum flux with the mean vertical wind shear that generates turbulence as described by e.g. Stull (1988) [11]. Fig.5 (left) presents average wind profiles for different TKE classes. For the classification the height of 100 m asl has been selected.
There is a clear relationship between the TKE and the wind profiles. The higher the TKE, the higher the wind speed. The highest TKE class i.e. TKE≥ $1.4 m^2/s^2$ (3577 vertical wind profiles, corresponding

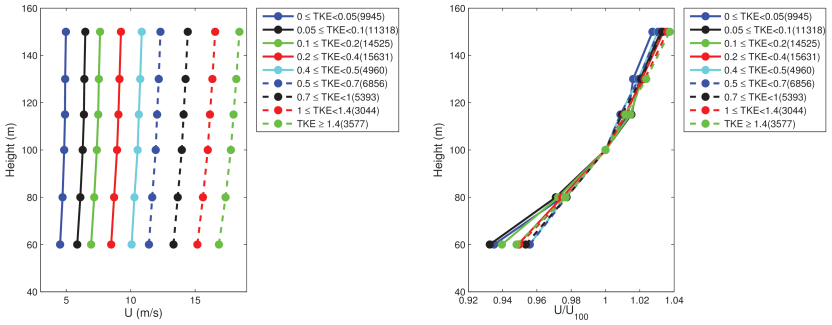


Fig. 5: Average wind profiles for different classes of TKE at 100 m asl (left) and the corresponding normalized profiles (right). The number of profiles for each class is given in parenthesis.

to 4.7 % of the data) corresponds to wind speeds greater than 16 m/s. On the other hand, for low TKE≥ $0.1m^2/s^2$ (21263 vertical wind profiles, corresponding to 28.25 % of the data), the wind speed is much lower (4-6 m/s). This behavior indicates that the TKE is predominantly generated by wind shear in the lowest 100 meters of the MABL. For an easier comparison between TKE and wind shear the vertical wind profiles are normalized to 1 at 100 m asl in the right panel of Fig. 5. For lower levels (60 m and 80 m asl), the wind shear is decreasing for increasing TKE. For levels above 100 m asl the wind shear becomes nearly independent of the TKE level.

## 4. Summary and Outlook

In the present study an analysis was performed to investigate the relationship between different turbulence parameters and offshore wind profiles based on 4 years of lidar measurements on the island of Storholmen off the Western coast of Norway. The results show that the investigated turbulence parameters, such as horizontal turbulence intensity, vertical turbulence intensity and turbulence kinetic energy, are strongly related to the average wind speed and the average shear of the profiles. The results indicate that it should be possible to adapt the general idea of determining stability classifications without temperature profile measurements, originally described for SODAR measurements onshore by Wharton and Lundquist (2012) [8], for offshore conditions and LIDAR measurements. Based on the presented study, the horizontal turbulence intensity seems to have the best potential for a corresponding stability classification for offshore conditions. However, the further development of this method, in particular the selection and validation of relevant threshold values of $I_U$, will require a tailored measurement campaign with parallel measurements of temperature and wind profiles offshore.

**Acknowledgements**

The presented research has been performed under WP1 (former WP5) of the the Norwegian Center for Offshore Wind Energy (NORCOWE) funded by the Norwegian Research Council (NFR project number: 193821). The authors are grateful to Dag T. Breistein and Andrea N. Eugster from Vestavind Offshore AS for sharing the wind lidar data. The lead author expresses his gratitude to NORCOWE and Statoil ASA for receiving the travel grant to participate and present this paper at the Deep Sea Offshore Wind R&D Conference in Trondheim on January 24 and 25, 2013.

References

[1] EWEA. Wind in our Sails - The coming of Europe's offshore wind energy industry. 2011;.
[2] EWEA. The European offshore wind industry - key trends and statistics 2012. 2013;.
[3] LEOSPHERE. Windcube User's Manual. March 2008;.
[4] Aitken ML, Rhodes ME, Lundquist JK. Performance of a Wind-Profiling Lidar in the Region of Wind Turbine Rotor Disks. J Atmos Oceanic Technol. March 2012;29:347–355.
[5] Rareshide E, Tindal A, Johnson C, Graves A, Simpson E, Bleeg J, et al. Effects of complex wind regimes on turbine performance. Proceedings American Wind Energy Association WINDPOWER Conference (Chicago, IL). 2009;.
[6] Wagner R, Antoniou I, Pedersen SM, Courtney MS, Jørgensen HE. The influence of the wind speed profile on wind turbine performance measurements. Wind Energy. 2009;12(4):348–362.
[7] Kaiser K, Hohlen H, Langreder W. Turbulence correction for power curves. Proceedings European Wind Energy Conference and Exhibition (Madrid). 2003;.
[8] Wharton S, Lundquist JK. Assessing atmospheric stability and its impacts on rotor-disk wind characteristics at an onshore windfarm. Wind Energy. 2012;15(4):525–546.
[9] Wharton S, Lundquist JK. Atmospheric stability affects wind turbine power collection. Environmental Research Letters. 2012;7(1):014005.
[10] Larsen GC. Offshore fatigue design turbulence. Wind Energy. 2001;4(3):107–120.
[11] Stull RB. An Introduction to Boundary Layer Meteorology. Atmospheric Sciences Library. Kluwer Academic Pub; 1988.

# Bibliography


[1] EWEA. *Wind in our Sails - The coming of Europe's offshore wind energy industry*, 2011.

[2] A. J. Eggers, Jr.R. Digumarthi, and K. Chaney. Wind shear and turbulence effects on rotor fatigue and loads control. *J. Sol. Energy Eng.*, 125(4):402–409, 2003.

[3] Elisabeth Rareshide, Andrew Tindal, Clint Johnson, AnneMarie Graves, Erin Simpson, James Bleeg, Tracey Harris, and Danny Schoborg. Effects of complex wind regimes on turbine performance. *Proceedings American Wind Energy Association WINDPOWER Conference (Chicago, IL)*, 2009.

[4] K Kaiser, H Hohlen, and W Langreder. Turbulence correction for power curves. *Proceedings European Wind Energy Conference and Exhibition (Madrid)*, 2003.

[5] Sonia Wharton and Julie K Lundquist. Atmospheric stability affects wind turbine power collection. *Environmental Research Letters*, 7(1):014005, 2012.

[6] Sonia Wharton and Julie K. Lundquist. Assessing atmospheric stability and its impacts on rotor-disk wind characteristics at an onshore windfarm. *Wind Energy*, 15(4):525–546, 2012. ISSN 1099-1824.

[7] J. F. Manwell, J. G. McGowan, and A. L. Rogers. Wind energy explained: Theory, design and application, 2nd ed. *Wiley*, 2010.

[8] A. Betz. Introduction to the theory of flow machines.(d. g. randall, trans.). *Oxford: Pergamon Press*, 1966.

[9] R.B. Stull. *An Introduction to Boundary Layer Meteorology*. Atmospheric Sciences Library. Kluwer Academic Pub, 1988. ISBN 9789027727695. URL http://books.google.no/books?id=eRRz9RNvNOkC.

[10] D. L. Elliott, C. Holliday, W. Barchet, H. Foote, and W. Sandusky. Wind energy resource atlas of united states. *DOE/CH 10093-4, Golden Colorado: Solar Energy Research Institute*, page 210, 1987.

[11] J.S. Touma. Dependence of the wind profile power law on stability for various locations. *Air Pollution Control Association*, 27:863–866, 1977.

[12] J. Counihan. Adiabatic atmospheric boundary layers: A review and analysis of data from the period 1880-1972. *Atmospheric Environment*, 79:871–905, 1975.

[13] S.A. Hsu, E.A. Meindl, and D.B. Gilhousen. Determining the power-law wind-profile exponent under near-neutral stability conditions at sea. *Appl. Meteor.*, 79: 757–765, 1994.

[14] H. Charnock. Wind stress on a water surface. *Quarterly Journal of the Royal Meteorological Society*, 81(350):639–640, 1955.

[15] Paul Gipe. Wind power: Renewable energy for home, farm, and business. April 2004.

[16] B. R. Bean and T. P. Repoff. A study of turbulent energy over complex terrain (state, 1978). *Boundary-Layer Meteorology*, 25:1, 1983.

[17] John L. Woodward. Estimating the flammable mass of a vapor cloud: A ccps concept book. *American Institute of Chemical Engineers*, pages 209–211, 1998.

[18] S.E. Gryning, E. Batchvarova, B. Brummer, H. Jrgensen, and S. Larsen. On the extension of the wind profile over homogeneous terrain beyond the surface boundary layer. *Boundary Layer Meteorology*, 124(2):251–268, 2007.

[19] K. A. Kloesel and B. A. Albrecht. Low-level inversions over the tropical Pacific-thermodynamic structure of the boundary layer and the above inversion moisture structure. *Mon. Wea. Rev.*, 117:87–101, 1989.

[20] Noaa - national oceanic and atmospheric administration - ocean. *Noaa.gov.*, Retrieved 8-11-2012.

[21] Peter Sullivan, James Edson, Tihomir Hristov, and James McWilliams. Large eddy simulations and observations of atmospheric marine boundary layers above non-equilibrium surface waves. 65(4):1225–1245, April 2008.

[22] Tindal A, Johnson C, LeBlanc M, Harman K, Rareshide E, and Graves A-M. Site-specific adjustments to wind turbinepower curves. *American Wind Energy Association WINDPOWER Conference, Houston, TX*, 2008.

[23] Rozenn Wagner. Accounting for the speed shear in wind turbine power performance measurement. *Ris-PhD-58(EN) - Short version*, April 2010.

[24] Christine Aussibal. Windcube users manual. *LEOSPHERE*, March 2008.

[25] LEOSPHERE. Windcube- lidar remote sensor. *www.lidarwindtechnologies.com.*

[26] T Fujii and T Fukuchi. Laser remote sensing. *Taylor and Francis Group*, page 912, 2005.

[27] Matthew L. Aitken, Michael E. Rhodes, and Julie K. Lundquist. Wind lidar performance in the region of turbine rotor disks. *Poster, University of Colorado at Boulder*, 2011.

[28] Matthew L. Aitken, Michael E. Rhodes, and Julie K. Lundquist. Performance of a wind-profiling lidar in the region of wind turbine rotor disks. *J. Atmos. Oceanic Technol.*, 29:347–355, March 2012. URL http://dx.doi.org/10.1175/JTECH-D-11-00033.1.

[29] Fernando Borbn Guilln, Paula Gmez, Javier Snz, Michael Courtney, and Alvaro Cuerva. Investigation of sources for lidar uncertainty in flat and complex terrain. *EWEA-2011 proceedings, Brussels (Belgium),*, March 2011.

[30] A. Albers and A.W. Janssen. Evaluation of windcub. *Deutsche WindGuard Consulting GmbH,Internal Project*, VC08007(Rep. PP 08007):30, 2008. URL http://www.leosphere.com/file/deusche_windguard_report_windcube_evaluation.pdf.

[31] G.B. Foote and P.S. du Toit. Terminal velocity of raindrops aloft. *J. Appl. Meteor.*, 8:249–253, 1969.

[32] V Wulfmeyer and G Feingold. On the relationship between relative humidity and particle backscattering coefficient in the marine boundary layer determined with differential absorption lidar. *J. Geophys. Res.*, D4(105):47294741, 2000.

[33] Bjorn Gjevik. Flow separation and lee-waves in the marine atmosphere. *Det norske Videnskabs-Akademi 16 Oct. 2009*, pages 1–41.

[34] Ola M. Johannessen and E. Korsbakken. Determination of wind energy from sar images for siting windmill locations. *Earth Observation Quarterly, European Space Agency*, (59):1–4, 1998.

[35] Johnny Johannessen. High resolution wind retrieval from satellites. *GEOF345 course, Geophysical Institute, UiB.*, pages 1–39, 2012.

[36] Gronas Sigbjorn and Sandvik D Anne. An analysis of sea and land breezes at high latitudes based on numerical simulations. in, condensation processes in a non-hydrostatic mesoscale model. *PhD thesis, Geophysical Institute, University of Bergen, Norway.*, pages 468–489, 1996.

[37] Morgan E, Lackner M, Vogel R M, and Baise L. Probability distributions for offshore wind speeds. *Energy Conversion and Management*, 52:15–26, 2011.

[38] Laurenson Dave. 'nakagami distribution', indoor radio channel propagation modelling by ray tracing techniques. retrieved 2007-08-04.

[39] Gunner C. Larsen. Offshore fatigue design turbulence. *Wind Energy*, 4(3):107–120, 2001. ISSN 1099-1824. doi: 10.1002/we.49.

[40] F. Pasquill. The estimation of the dispersion of windborne material. *The Meteorological Magazine*, 90(1063):33–49, 1961.

[41] Pagen Dennis. Understanding the sky. *City: Sport Aviation Pubns*, pages 169–175, 1992.

[42] Dale R. Durran. Lee waves and mountain waves. *The Encyclopedia of the Atmospheric Sciences*, pages 1161–1169, 2003.

[43] John A. Ernst. Sms1 nighttime infrared imagery of lowlevel mountain waves. *Monthly Weather Review*, 104:207–209, 1976.

[44] Paul Markowski and Yvette Richardson. Mesoscale meteorology in midlatitudes. *Wiley,Advancing Weather and Climate Science*, page 343, 2010.

[45] Low-level coastal jets (summary). *COMET Program,http://www.meted.ucar.edu/mesoprim/coastaljets/frameset.htm.*

[46] Idar Barstad and Sigbjorn Gronas. Southwesterly flows over southern norwaymesoscale sensitivity to large-scale wind direction and speed. *Tellus*, 57A:136–152, 2005.

[47] Gronas Sigbjorn and Sandvik D Anne. Numerical simulations of sea and land breezes at high latitudes. *Tellus*, 50A:468–489, 1998.